國立臺灣大學理學院大氣科學研究所

博士論文

Department of Atmospheric Sciences

College of Science

National Taiwan University

Doctoral Dissertation

赤道印度洋準雙日週期對流擾動：DYNAMO 實驗觀測

Quasi-2-day Convective Disturbances

in the Equatorial Indian Ocean: DYNAMO Observation

尤虹叡

Hungjui Yu

指導教授：郭鴻基 博士、Richard H. Johnson, Ph.D.

Advisors: Hung-Chi Kuo, Ph.D., Richard H. Johnson, Ph.D.

中華民國 107 年 7 月

July 2018

國立臺灣大學博士學位論文
口試委員會審定書

　　本論文係 尤虹叡 君（學號 F99229021）在國立臺灣大學大氣科學學系、所完成之博士學位論文，於民國 107 年 7 月 12 日承下列考試委員審查通過及口試及格，特此證明

口試委員： 　郭鴻基　 _Richard H. Johnson_ （簽名）

（指導教授）

	楊明仁
	黃彥婷
劉清煌	吳俊仁

系主任、所長 　林博雄　 （簽名）

ACKNOWLEDGMENT

誌謝

　　這項研究論文的完成，首要感謝指導教授 郭鴻基 教授自學生大學時代以降多年來不吝的鼓勵與指導，不論是在大學時期的獨立研究、當兵前、乃至隻身負笈前往科羅拉多、返臺繼續研習，教授激勵的話語總化為我繼續邁向前方的動力。

　　深深感謝博士學位考核委員：國立臺灣大學楊明仁教授、吳健銘教授、黃彥婷教授、國立臺灣師範大學王重傑教授、中國文化大學劉清煌教授，給予這項研究許多正面的建議與評價。另外，也非常感謝在求學期間曾指導、鼓勵我的師長：國立臺灣大學林博雄教授、陳泰然教授、隋中興教授、周仲島教授、李清勝教授、吳俊傑教授、林依依教授、科羅拉多州立大學 Dr. Wayne H. Schubert、以及中國文化大學蘇世顥教授。

　　感謝王美雲助理、以及動力模擬研究團隊的夥伴們，不論是學長姐們的指點、同學們、學弟妹們的激勵與討論，都化為彼此成長的養份。也謝謝這段時間同時為了不同目標而努力的兄弟們：俠哥、鄉長、小毛、亞洲甜心、郭眼科、黑哥、恩恩、蘇醫師、小 phy、Joe。人生得一知己足矣，我何嘗幸運在人生中有你們同行！

My deepest gratitude goes to my co-advisor at Colorado State University, Dr. Richard H. Johnson, who has been providing me with the most insightful and inspiring ideas, not only throughout my time at CSU but also afterward. Without his guidance, I could never have the chance to broaden my horizon.

And I must give the greatest thank to the mentor/friend of mine from CSU, Mr. Paul E. Ciesielski, for his constant motivation and support not only on my pursuit of better science (and of course, English writing) but also in life. I am immensely grateful for this friendship between generations.

I would also like to thank my friend/officemate from Johnson Research Group, Dr. James Ruppert, for the wonderful time of scientific discussion and life-sharing (and beer!).

I must also acknowledge the crews of DYNAMO field campaign from all around the world, especially those from the US, Japan, Maldives, and Taiwan, for their tremendous efforts toward the success of this field experiment.
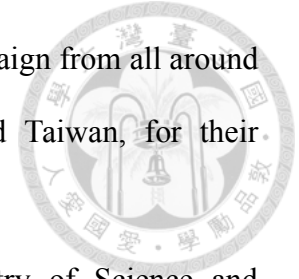
尤如嶽 Hung Tsu Tu   戊戌仲夏 July 2018

DEDICATION

This dissertation is dedicated to my family,

to my loving parents, Dennis and Grace,

and my sister and my brother in law, Mimi and Javier,

to my dearest wife Nina,

to my lovely son Christopher,

lastly, to my late grandmother

尤楊瓊枝 女士

who had made all these possible.

ABSTRACT

This study examines the westward-propagating convective disturbances with quasi-2-day intervals of occurrence identified over Gan Island in the central Indian Ocean from mid to late October 2011 during the Dynamics of the Madden-Julian Oscillation (DYNAMO) field campaign. Atmospheric sounding, satellite, and radar data are used to develop a composite of seven such disturbances.

Composites and spectral analyses reveal that: (1) the quasi-2-day convective events comprise westward-propagating diurnal convective disturbances with phase speeds of 10–12 m/s whose amplitudes are modulated on a quasi-2-day time scale on a zonal scale of ~1000 km near the longitudes of Gan; (2) the cloud life cycle of quasi-2-day convective disturbances shows a distinct pattern of tropical cloud population evolution—from shallow-to-deep-to-stratiform convection; (3) the time scales of mesoscale convective system development and boundary layer modulation play essential roles in determining the periodicity of the quasi-2-day convective events; and (4) in some of the quasi-2-day events there is evidence of counter-propagating (westward and eastward) cloud systems along the lines proposed by Yamada et al.

Based on these findings, an interpretation is proposed for the mechanisms for the quasi-2-day disturbances observed during DYNAMO that combines concepts from prior studies of this phenomenon over the western Pacific and the Indian Ocean.

Keywords: quasi-2-day convective disturbance, DYNAMO, Indian Ocean, diurnal, mesoscale convective system, stratiform, boundary layer

ABSTRACT (Chinese Version)

中文摘要

本研究分析 2011 年十月 Dynamics of the Madden-Julian Oscillation（DYNAMO）現地觀測實驗當中，在赤道中印度洋所觀測到發生週期約莫為兩天（準雙日）的西行對流擾動。本研究運用 DYNAMO 實驗期間的探空觀測、衛星與雷達資料，分析七組準雙日對流擾動個案。

合成分析與波譜分析結果顯示：1、準雙日對流擾動包含波速為 10–12 m/s 的西行單日週期對流擾動。該對流擾動的強度在中印度洋 Gan Island 附近、緯向空間尺度約為 1000 公里的範圍被調整為準雙日週期。2、準雙日對流擾動中的對流活動變化具有典型的中尺度對流生命期特徵，包含顯著的"淺對流－深對流－層狀雲"變化。3、準雙日對流擾動的發生週期，受中尺度對流系統發展的時間尺度與邊界層恢復時間決定，長時間的邊界層恢復將單日週期對流擾動調整為準雙日週期。4、觀測證據顯示在一些準雙日對流擾動個案當中，包含東西向相對移行的雲系，此結果類似 Yamada 等過去透過印度洋觀測資料所提出的概念模型。

結合以上分析結果、並根據過去在西太平洋與印度洋的觀測，本研究提出一項新的概念模型，從赤道印度洋 MJO 期間的風切環境及中尺度對流過程的角度，解釋 DYNAMO 實驗期間所觀測到的準雙日對流擾動發生機制及其特殊發生週期。

關鍵字：準雙日對流擾動、DYNAMO、印度洋、單日週期、中尺度對流系統、層狀雲、邊界層

CONTENTS

LIST OF TABLES

LIST OF FIGURES

dashed circles ~235–260 K). The smallest circle represents the early stage of the system (first afternoon cross-section in Figure 1.4), the largest circle represents the mature stage with the maximum areal extent of cold cloud tops (pre-dawn cross-section in Figure 1.4), and the dashed circles represent the warmer cloud deck (last cross-section in Figure 1.4). (b) The westward-propagating speed of 2-day equatorial inertial gravity waves is added to the westward displacement of the starting location of a new convective system. The pattern in (b) is the sum of the effects of the ISO, 2-day waves and the diurnal cycle of large convective systems. (Figure 19 in Chen and Houze 1997)

xi

xv

Chapter 1　Introduction

As quoted from Aaron B. Sorkin, "*The first step in solving any problem is recognizing there is one*". Among all challenges facing the community of atmospheric sciences, the first step should always be to obtain the necessary observations and information, that is, as the main theme of the 97th American Meteorological Society annual meeting goes, "*Observations lead the way*". Over the decades, many field campaigns aiming to advance our understanding of the atmosphere were conducted in this philosophy, especially for the understanding of the tropics.
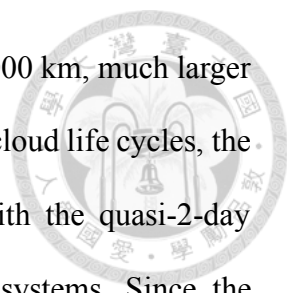
From time to time, the tropical atmosphere feels the pulses of extraordinary deep convection in multiple temporal and spatial scales. It is the broad spectrum of scales and the possible interactions between these scales that make the understanding of tropical convection difficult (Clayson et al. 2002). For example, Nakazawa (1988) noted that the convective envelopes in association with the active intraseasonal oscillations (ISOs) were often composed of several smaller-scale individual cloud clusters that tend to propagate westward, while the larger-scale ISO convective envelope propagates eastward. Specifically, convectively active, westward-propagating disturbances with a quasi-2-day periodicity are frequently associated with ISOs over the tropical western Pacific (WPAC; Nakazawa 1988, 1995; Hendon and Liebmann 1994; Takayabu 1994a,b; Takayabu et al. 1996; Chen et al. 1996).

In particular, these convective disturbances received considerable attention in studies based on observations taken during the Tropical Ocean Global Atmosphere Coupled Ocean-Atmosphere Response Experiment (TOGA COARE) intensive observation period (IOP; experimental domain illustrated in Figure 1.1) in 1992–1993 over the equatorial WPAC (Nakazawa 1988, 1995; Lau et al. 1991; Takayabu 1994a,b;

1

Takayabu et al. 1996; Chen et al. 1996; Haertel and Johnson 1998; Haertel and Kiladis 2004). During the TOGA COARE IOPs, two eastward-propagating Madden-Julian Oscillations (MJOs) convective systems were observed over the outer sounding array (OSA) and the Intensive Flux Array (IFA) in December 1992 and early 1993, respectively (Takayabu et al. 1996, Figure 2, as shown in Figure 1.2). Embedded in these systems were smaller-scale, mostly westward-propagating convective disturbances which possessed the quasi-2-day variation as found in the time series of satellite infrared blackbody temperature over IFA in December 1992 (Figure 1.2 bottom).

Based on TOGA COARE observations, previous studies regarded these 2-day convective events as convectively coupled equatorial waves, referred to as "2-day waves", characterized by zonal wavelengths of 2000–4000 km, westward propagation of 10–15 m/s (Hendon and Liebmann 1994; Takayabu 1994b; Takayabu et al. 1996; Chen et al. 1996; Haertel and Johnson 1998; Wheeler et al. 2000) and associated with the n=1 inertio-gravity wave (IGW) with equivalent depths of 12–50 m (Takayabu 1994a; Wheeler and Kiladis 1999). Observations from TOGA COARE also revealed that the quasi-2-day waves were comprised of westward-propagating organized cloud clusters (Chen et al 1996; Chen and Houze 1997), and further indicated that the quasi-2-day convective disturbances possessed a life cycle similar to that of organized mesoscale convective systems (MCSs) or long-lived squall lines (Hendon and Liebmann 1994; Takayabu et al. 1996). As proposed in the quasi-2-day variation schematics by Takayabu et al. (1996, Figure 19, as shown in Figure 1.3), four stages of cloud life cycle were identified from predominantly shallow-to-deep-to-stratiform convection (the shallow convection stage, the initial tower stage, the mature stage and the decaying stage), which repeated at quasi-2-day intervals from local observations.

According to Takayabu et al. (1996), the spatial scales of trailing anvil associated

2

with the quasi-2-day convective systems were observed to be 800–1000 km, much larger than those of the squall-line systems. In addition, despite the similar cloud life cycles, the recovery time of moisture in the lower troposphere associated with the quasi-2-day disturbances, near 24 h, was longer than that of the squall-line systems. Since the development of the next vigorous convective stage follows the moisture recovery in the lower troposphere, it is speculated in Takayabu et al. (1996) that the required time for the recovery of the lower-tropospheric moisture filed sets the timing of the quasi-2-day disturbances.

To explain the quasi-2-day intervals of occurrence, Chen and Houze (1997) suggested that the near 2-day periodicity results from an interaction between the "2-day waves" and convection. A conceptual mesoscale process involving the nonlinear interaction between clouds, radiation, and surface processes was proposed, to explain the near 2-day periodicity. As shown in the schematic in Chen and Houze (1997, Figure 18, as shown in Figure 1.4), a large convective system which forms in the afternoon, usually takes about 6–12 hours to grow and maximize in its areal extent of high cloud-tops (cloud-top temperature <208 K). As the large systems age, the cloud tops continue to expand and become warmer due to the absorption of solar radiation. During the expansion of the upper-level clouds, the short-wave absorption by the long-lasting cloud deck stabilizes the troposphere (Randall et al. 1991), and low moist-static-energy downdrafts associated with the cloud systems radically change the character of the lower-troposphere and the boundary layer (Zipser 1977). In their scenario despite diurnal radiative forcing, boundary layer (BL) recovery extends to a second day likely due to the expanded stratiform clouds of large MCSs, which impacts the timing of the next round of convection, i.e., the new intense convective event does not readily initiate at the same location on the next day due to the stabilization of the BL and the atmosphere. According to TOGA COARE

observations, the BL recovery for a future convective event over a given region is delayed for up to 12–18 hours by the previous convective systems.
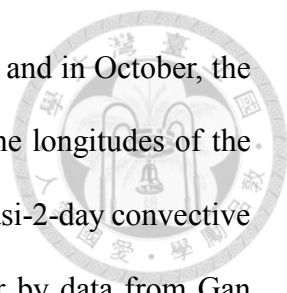
This so-called "diurnal dancing" process of convective systems is more prominent during the active phase of the ISO since the large convective systems occur more frequently. The process can be interpreted in the time-longitude diagram as shown in Figure 1.5a (Chen and Houze 1997, Figure 19a) which suggests that the convective systems on day 2 are most likely to form in a relatively clear region adjacent to the dissipating system form the previous day (day 1). By the time when the atmosphere and BL are recovered near the region of convection on day 1, a new convective system can be triggered again on day 3, forming a "checkerboard-like" pattern of convection (Figure 1.5a). In the existence of the "2-day waves" within the ISO envelope, this process may phase-lock with the westward-propagating IGWs, helping select the "2-day waves" as the dominant mode (Figure 1.5b). As stated in Chen and Houze (1997), this combination of 2-day IGWs and the diurnal variation is very similar to the observed variation of cold cloudiness in TOGA COARE IOP (Chen et al. 1996, Figure 11, as shown in Figure 1.6).

Similar to TOGA COARE over the WPAC warm pool, quasi-2-day convective disturbances were observed in the boreal fall of 2006 during the Mirai Indian Ocean (IO) cruise for the Study of the Madden-Julian oscillation convective Onset (MISMO) experiment (Yoneyama et al. 2008). Leveraging both satellite IR and microwave data along with ground-based radar observations, Yamada et al. (2010) detected a complicated relationship between eastward-propagating precipitating systems and westward-moving upper-level cloud shields, which yields a 2–4 day periodicity in rainfall at a given longitude (Figure 1.7). As summarized in their schematic diagram (Yamada et al. 2010, Figure 15, as shown in Figure 1.8), the convective cells propagate eastward while trailing stratiform clouds in the upper troposphere move westward, due to the background flows

with a westerly in the lower troposphere and easterly aloft. The eastward-propagating systems, generally less than 10 km in depth, deepened when they encountered the moisture-rich environment of the westward-moving upper-level stratiform clouds. These stratiform cloud shields advected by upper-level easterlies were trailing clouds remnants from previous eastward-propagating convective systems. The coexistence of eastward and westward convective components can cause a 2–4 day cycle of cloud tops and rainfall at each longitude (Figure 1.8).

In addition to these quasi-2-day features observed in previous field campaigns, westward-propagating mesoscale convective events with a similar periodicity were also prominent over the equatorial IO within the convective envelope of the October MJO event during the Dynamics of the Madden-Julian Oscillation (DYNAMO)/Atmospheric Radiation Measurement MJO Investigation Experiment (AMIE)/Cooperative Indian Ocean experiment on intraseasonal variability in the Year 2011 (CINDY) field campaign (Johnson and Ciesielski 2013; Yoneyama et al. 2013; Zuluaga and Houze 2013; Johnson et al. 2015). The field campaigns (hereafter DYNAMO) were designed to observe and understand the initiation of the MJO over the IO (experimental domain illustrated in Figure 1.9). Its observational network consisted of a large suite of measurements of the atmosphere and ocean, but for this study, high-resolution upper-air radiosonde data and remote sensor retrievals from radars and satellites are utilized.

During DYNAMO, three MJO convectively active events with cold cloud-tops and significant rainfall were observed over the IO (Figure 1.10 and Figure 1.11), the events in October and November were more prominent than the event in December (Yoneyama et al. 2013; Johnson and Ciesielski 2013), and the period between the first two MJO events was about 30 days, shorter than that observed in TOGA COARE. As shown in Figure 1.10 and Figure 1.11, a diurnal cycle of westward-moving precipitation

5

features is observed over the longitudes of Sumatra (~95°E –100°E), and in October, the diurnal cycle transitioned to a quasi-2-day cycle farther west near the longitudes of the DYNAMO sounding arrays (Johnson and Ciesielski 2013). Seven quasi-2-day convective events with significant rainfall identified in the last half of October by data from Gan Island in the central IO are examined in this study and used to form a composite view of the wind, thermodynamic, and diabatic structure of the disturbances.

The observational datasets used in the study are described in Chapter 2. The analysis procedures and the methodology for identifying the quasi-2-day convective events are explained in Chapter 3. Large-scale convective features of these events including their propagation and the spatial scale are shown in Chapter 4. In Chapter 5, differences between the quasi-2-day and diurnal convection are discussed. The composite atmospheric structures and life cycle of the quasi-2-day convective disturbances are analyzed in Chapter 6. In Chapter 7, an interpretation for the quasi-2-day convective disturbances is proposed. Finally, Chapter 8 summarizes the observational results. A major portion of this study had been published in Yu et al. (2018).

Chapter 2 Data
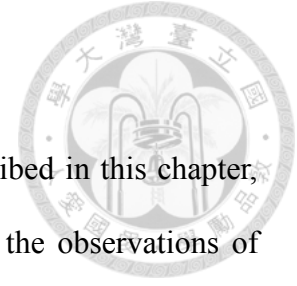
The observational datasets employed in this study are described in this chapter, including the gridded data over the IO and the datasets based on the observations of various instruments at Gan Island. These datasets are mostly available online from the EOL DYNAMO data archive (http://data.eol.ucar.edu/master_list/?project=DYNAMO).

2.1 Gridded data over the Indian Ocean

2.1.1 Gridded satellite data of infrared brightness temperature and rain rate

The 5-km resolution, 3-hourly interpolated Meteosat-7 infrared (channel 8) brightness temperature (IRBT) data and the 0.25° resolution, 3-hourly rain rate estimates from Tropical Rainfall Measuring Mission (TRMM) 3B42V7 dataset are both employed in this study. The major purpose of these datasets is to identify the occurrences of the quasi-2-day convective events as well as their broad-scale convective features.

2.1.2 CSU-DYNAMO upper-air and surface gridded analyses

The gridded analyzed fields including the upper-air horizontal winds were obtained from the CSU-DYNAMO upper-air and surface gridded analyses provided by CSU Mesoscale Dynamics Group at the Department of Atmospheric Science, Colorado State University. This 3-hourly dataset was majorly based on DYNAMO observations and was produced on 1° horizontal grids, 25-hPa vertical resolution (1000 to 50 hPa) using the multiquadric interpolation scheme of Nuss and Titley (1994). In this study, the version 3B dataset, in which the observations were supplemented with ECMWF Operational Analyses (OA) in data sparse regions, is specifically used for large-scale wind field analysis during DYNAMO. More details about this dataset can be found online (http://johnson.atmos.colostate.edu/dynamo/products/gridded/index.html)   and   in Johnson and Ciesielski (2013) and Johnson et al. (2015).

7

2.1.3 NOAA OI Sea Surface Temperature (SST) V2 high resolution dataset

The 0.25° resolution, daily SST data during October–December from 1998 to 2012 are used in this study for climatology analysis (section 5.4). This dataset is provided by the National Oceanic & Atmospheric Administration, Oceanic and Atmospheric Research, Earth System Research Laboratory, Physical Sciences Division (NOAA/OAR/ESRL PSD), Boulder, Colorado, USA (from their Web site at https://www.esrl.noaa.gov/psd/).

2.2 Gan Island observations

2.2.1 Upper-air radiosonde observations

The DYNAMO enhanced sounding array (ESA) was comprised of six sites forming two quadrilateral arrays (northern/southern sounding array) in the central equatorial IO during the special observing period (SOP) from 1 October to 30 November (Figure 1.9). The purpose of these sounding sites was to observe the evolution of atmospheric vertical structures using 3- to 6-hourly, high-vertical resolution radiosondes and to compute the large-scale forcing fields as well as heat and moisture budgets (Johnson and Ciesielski 2013; Yoneyama et al. 2013; Johnson et al. 2015). This study uses primarily the 3-hourly sounding data from Gan during the DYNAMO SOP. The high-resolution sounding data were interpolated to 5 hPa for use in this study. More information on the sounding systems, observing characteristics, and quality-control procedures for DYNAMO soundings are contained in APPENDIX A, further details can be found in Ciesielski et al. (2012; 2014) and Yu et al. (2015).

2.2.2 AMIE-Gan large-scale objective analysis

Large-scale fields, including apparent heating Q_1, apparent drying Q_2, and vertical motion, were obtained from AMIE-Gan objective analyses patterned after the procedure

of Xie et al. (2004). These analyses, covering a nearly circular region with 150 km radius centered on Gan (as illustrated in Figure 2.1), were available from 2 October to 31 December 2011 at 3-hour temporal resolution. The dataset was constructed by using the variational analysis method described in Zhang and Lin (1997) and Zhang et al. (2001) and constrained by C-band Shared Mobile Atmospheric Research and Teaching Radar (SMART-R) rainfall estimates ($P_{SMART-R}$) adjusted with TRMM rainfall (P_{TRMM}) using the following procedure as described in Ciesielski et al (2017),

$$P_{SMART-R\,(adjusted)} = P_{SMART-R} * P_{TRMM\,(150\,km\,region)} \Big/ P_{TRMM\,(SMART-R\,domain)}$$

This adjustment retains the variability of the TRMM 3B42 rainfall but with the magnitude set by the SMART-R. Use of the surface rainfall constraint in the analyses ensures that the vertically integrated large-scale heat and moisture budgets are consistent with the observed precipitation over the region.

2.2.3 Combined Remote Sensor retrieval (CombRet) dataset

Vertical profiles of the shortwave/longwave radiative fluxes and heating rates were obtained from the Pacific Northwest National Laboratory (PNNL) Combined Retrieval (CombRet) dataset (Feng et al. 2014). The CombRet radar product includes high-resolution data from the SMART-R, NCAR's S-band dual-polarization Doppler radar (S-Pol), and the Ka-band ARM zenith radar (KAZR) deployed on Gan. The radiative product was retrieved by using a delta-four-stream correlated k-distribution radiative transfer model (Mather et al. 2007, Fu and Liou 1992). CombRet is available at 1-hour, 25-hPa resolution (from 1000–50 hPa) for the period from 10 October 2011 to 08 February 2012, and was averaged into 3-hour bins to match the temporal resolution of the

9

satellite, rainfall, and sounding data. The version of CombRet data used in this study was produced by replacing the observed 2-m temperature with the SST in the near vicinity of Gan, which makes the radiative fields more representative of open-ocean conditions. Radiative fields are available for both all-sky and clear-sky conditions allowing us to estimate cloud radiative forcing effects.
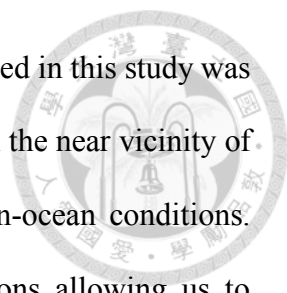
Chapter 3 Analysis Procedures

3.1 Computation of vertical flux of moist static energy
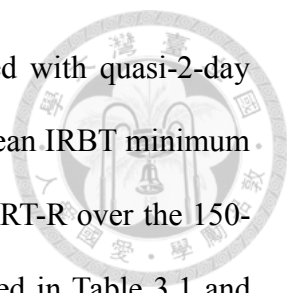
The vertical eddy flux of moist static energy (MSE), referred to as F_{MSE}, has been widely used to measure the activity of cumulus convection (Yanai et al. 1973; Gallus and Johnson 1991; Johnson et al. 2015). In this study, the composite F_{MSE} is estimated following Yanai et al. (1973),

$$F_{MSE} = \frac{1}{g}\int_{P_{100hPa}}^{P}(Q_1 - Q_2 - Q_R)dp \cong -\frac{1}{g}\overline{h'\omega'},$$

in which Q_1 and Q_2 were obtained from AMIE-Gan analysis while Q_R (total longwave and shortwave radiative forcings) is the net radiative heating rate retrieved from CombRet data. $(Q_1 - Q_2 - Q_R)$ was then integrated downward from 100 hPa (a reasonable cloud top pressure where F_{MSE} equals zero) to each pressure level to estimate the F_{MSE} profiles as $-\frac{1}{g}\overline{h'\omega'}$.

3.2 Identification of the quasi-2-day convective events

This study focuses on the convective activities over the central IO, especially the area around Gan (as illustrated in Figure 2.1). During the convectively active period of the October MJO over this region (15–31 October 2011), convective activity and precipitation tended to occur at quasi-2-day intervals (Zuluaga and Houze 2013) as shown in the time series of average and areal percentage of IRBT, averaged TRMM rain rate and adjusted SMART-R surface rain rate (Figure 3.1a). The IRBT areal percentage in Figure 3.1a was calculated by dividing the number of IRBT grid points in 5-K intervals by the total number of grid points over the 150-km circular region around Gan.

11
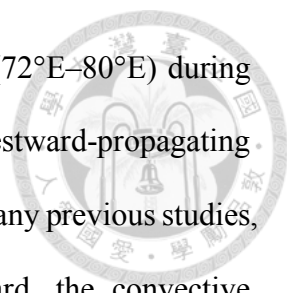
From the time series, seven convective events are identified with quasi-2-day periodicity and convective activity characterized by clouds with a mean IRBT minimum below 240 K and rain rates higher than 1 mm/hr in TRMM or SMART-R over the 150-km region near Gan. The criteria and times of these events are listed in Table 3.1 and indicated in Figure 3.1a. These times of IRBT minimal peaks were used as the 0-hour for the 48-hour window composite analyses. The convective event on 30 October showed an averaged IRBT lower than 240 K; however, it was excluded from the composite analyses due to the fact that the mean rainfall near Gan was considerably less than the other events and the radar reflectivity indicated mostly stratiform clouds over Gan throughout the time of event (Figure 3.2). By way of comparison, the first six of the seven convective events identified by the IRBT and rain rate signatures in our study were included in the 11-case composite of Zuluaga and Houze (2013) based on hourly S-Pol rain accumulation (Table 3.2). However, their composite analysis also includes events on a 4–6 day time scale associated with synoptic-scale waves from the November and December MJOs. Although the sample size in our study is small, there appears to be no preferred time of day for the 0 h occurrence of these events.

12

Chapter 4　Large-scale Convective Features of the Quasi-2-day Convective Events

One of the conspicuous large-scale convective features during DYNAMO SOP was the eastward-moving MJO convective envelope passing over Gan and the DYNAMO ESA from 15 to 31 October 2011 (Figure 1.10 and Figure 1.11). During this convectively active period over the central IO, hereafter referred to as MJO1, seven quasi-2-day convective events occurred at Gan. According to the IRBT areal percentage in Figure 3.1a, during MJO1 the frequency of shallow cloud-tops reached a maximum before the rainfall peaks. The clouds then evolved into a deeper structure and reached maturity when the lowest IRBT peaks occurred. Following the mature stage, deep convective cores gradually dissipated while the frequency of warmer cloud-tops (250–270 K), some of which may be stratiform in nature, maximized (Zuluaga and Houze 2013, Zhang and Yoneyama 2017). These convective transitions repeated at quasi-2-day intervals during MJO1. A second major MJO event occurred over the IO in November with a convectively active phase at Gan from 15 to 30 November 2011 (Figure 1.10 and Figure 1.11), however, the quasi-2-day convective signal was not statistically significant over the central IO region during this period and therefore is not considered in this study (see APPENDIX B). The reasons for this difference between the two periods may be related to the different MJO propagation features over the DYNAMO ESA, but further examination is needed for the full explanation.

Figure 4.1, similar to Figure 1.10 and Figure 1.11, is a time-longitude diagram of IRBT and TRMM rain rate averaged over a 1.5° latitude strip north and south of Gan showing the large-scale zonal features of these quasi-2-day convective events. During DYNAMO, the convective envelope of the October MJO initiated over 60°E–70°E on 14

October, slowly propagated eastward through the DYNAMO ESA (72°E–80°E) during 15–31 October, which then encountered the diurnally excited, westward-propagating convective signal from Sumatra in early November. As observed in many previous studies, although the MJO convective signal over IO propagated eastward, the convective envelope was comprised of a number of westward-propagating features at shorter time scales (Nakazawa 1988, 1995; Hendon and Liebmann 1994; Takayabu 1994a,b; Takayabu et al. 1996; Chen et al. 1996). The diurnally pulsing, westward-moving convection near the west coast of Sumatra Island (90°E–100°E) may have had some linkages to the convection over the central IO (Kubota et al. 2015); however, such a linkage is not entirely obvious from Figure 4.1.

Focusing on the quasi-2-day convective events over Gan, Figure 4.2 depicts the time-longitude IRBT, TRMM rain rate and 850-hPa total wind composites of the seven events over the DYNAMO ESA. The reference time 0 h, corresponding to the times listed in Table 3.1, is characterized by the lowest averaged IRBT over Gan. In Figure 4.2, the region of convective activity propagated westward from the eastern portion of the ESA, peaking over the area surrounding Gan with dominant cold clouds and heavy rainfall near 0 h. The 850-hPa total wind field shows in general westerlies to the west of Gan and slight easterlies to the eastern ESA. Noted that the zonal wind component shows a low-level convergence prior to the onset of deep convection over Gan, and the westerlies extend toward the east of Gan as the convective disturbance passes through. The ~500–1000 km zonal scale of the area of lower IRBT (< 240 K) suggests the presence of anvil shields and is consistent in size with observations made in TOGA COARE (800–1000 km; Takayabu et al. 1996). As depicted in the horizontal time evolution of seven-event composite (Figure 4.3), after time 0 h, the convective signal continued to move westward while the peak IRBT gradually warmed at Gan, suggesting (and confirmed later) that

14

broad areas of stratiform clouds dominated during this period.

The westward propagation speed of the convective signals can also be estimated from Figure 4.2. Considering time-longitude IRBT composites lower than 240 K, the convective signal propagated 7°–8° in longitude in 20 hours, while the rainfall signal showed a similar speed but extended over a greater zonal distance. The propagation speed of the quasi-2-day convective signal is thus approximated to be 10–12 m/s, the same order as that observed over different areas in previous studies, i.e., 10–19 m/s over WPAC during TOGA COARE IOP in 1992–1993 (Haertel and Johnson 1998 as shown in Figure 4.4; Takayabu 1994b) and 15 m/s in Hendon and Liebmann (1994).

While the quasi-2-day convective events over the equatorial IO possess similar propagation speeds as those over the WPAC, the zonal scales are different. From Figure 4.1 to Figure 4.3, the zonal scale of propagation for the 2-day disturbances is ~1000–1500 km, shorter than the ~2000–4000 km scale observed for the WPAC during the TOGA COARE IOP (Chen et al. 1996; Chen and Houze 1997; Clayson et al. 2002). The difference could well be related to differences in the environments between the two ocean basins, but a full explanation is beyond the scope of this study.
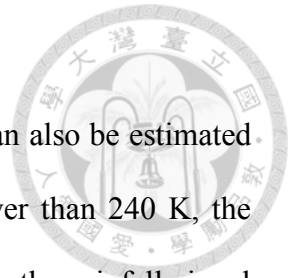
Chapter 5　Propagating　Convective　Waves　and Stationary Convective Disturbances

5.1　Fourier power spectral analysis

During MJO1, the passage of the westward-propagating quasi-2-day convective events regulated the cloudiness over Gan. To investigate the cloud variability, Fourier spectral analysis is employed to quantify the frequency and intensity of cloud activity associated with the quasi-2-day disturbances during MJO1.
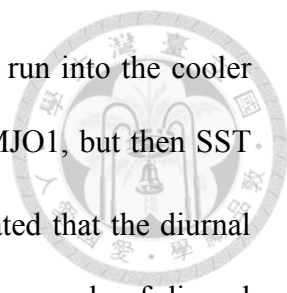
Identical with the procedure in Haertel and Johnson (1998), Figure 5.1 shows the Fourier power spectrum of the averaged IRBT over 150-km region around Gan from October to December 2011 and during MJO1. Here the spectral components are weighted by frequency so that within a certain frequency band, the variance of IRBT time series is proportional to the area under the peak. From October to December, significant spectral peaks are seen at 30-day, 13-day, 5-day, and close to 2-day (dotted curve in Figure 5.1). These results are similar to the findings in TOGA COARE over WPAC (Haertel and Johnson 1998) as shown in Figure 5.2 except for the peak near the shorter 30-day period in DYNAMO (Figure 1.10, Figure 1.11) compared to the 60-day peak in TOGA COARE, which was due to the MJO events passing over Gan in late 2011 with a time interval of about 30 days (Johnson and Ciesielski 2013; Yoneyama et al. 2013). The peaks in both the diurnal (0.9–1.2 day) and quasi-2-day (1.6–3 day) frequency bands are statistically significant but the diurnal oscillation was weaker than quasi-2-day oscillation over this region (more details on the significance tests in APPENDIX B). The quasi-2-day (diurnal) cloud oscillation contributed approximately 54.7% (12.3%) of the variance during MJO1 over Gan and about 15.7% (3.2%) from October to December 2011. And the quasi-2-day

16

oscillation contributed about 17% of the variance over the IFA in TOGA COARE from November 1992 to February 1993 (Haertel and Johnson 1998).

5.2   Separation of diurnal and quasi-2-day oscillations

By applying a Lanczos bandpass filter (Duchon 1979; Thomson and Emery 2014), the diurnal and quasi-2-day oscillations in IRBT during MJO1 can be separated as shown in Figure 3.1b and Figure 3.1c. The response functions associated with the bandpass filter are shown in Figure 5.3. Note that the time difference between minima in the diurnal signal ranged from 24–27 hours in Figure 3.1b due to the width of the diurnal filter allowing frequencies between 0.9 and 1.2 days to be retained. Having about half the amplitude of the quasi-2-day signal, the diurnal signal tends to grow then wane as the MJO convective envelope passes.

By applying this filter along each longitude during MJO1, Figure 5.4 shows time-longitude diagrams of averaged IRBT and TRMM rain rate within 1.5° latitude north and south of Gan for the diurnal (Figure 5.4a, c) and quasi-2-day (Figure 5.4b, d) signals. The equatorial diurnal convective signals were stronger near Sumatra than over the open ocean, indicating the dominant strong diurnal forcing of convection by topography (Yanase et al. 2017). The cloud signals accompanied by a precipitation signal originated daily from the terrain of Sumatra in the late afternoon (16–18LT) and propagated westward over IO owing to the dominant background easterlies near Sumatra (Yanase et al. 2017). As the diurnal convective signal propagated westward away from the terrain, it gradually weakened over the IO. Another group of relatively strong diurnal signals appeared across the DYNAMO ESA as part of the MJO1 convective envelope, though not apparently linked to the diurnal signal coming off of Sumatra. One possible explanation for the separated diurnal signals lies in the SST distribution during the period

17

of study. Figure 5.5 shows that diurnal signals coming off Sumatra run into the cooler water to the east of the DYNAMO ESA near $90°E - 95°E$ during MJO1, but then SST starts to increase between $80°E–85°E$ and farther west. It is speculated that the diurnal signals coming off Sumatra die off due to cooler SST, but then a new cycle of diurnal convection initiates farther west associated with warmer SST. While the source of this separate regime of diurnal convection is difficult to ascertain, radiative effects were undoubtedly playing a prominent role (Gray and Jacobson 1977; Randall et al. 1991; Chen and Houze 1997). The gradual advance in the timing of the peaks in the diurnal signal at Gan (Figure 3.1b) is generally consistent with the slow eastward drift in the origins of the diurnal signals across the ESA (Figure 5.4a). Correspondingly, the peaks in the quasi-2-day signals advance slowly with time as well (Figure 3.1c).

The IRBT and TRMM rain rate signals associated with quasi-2day periodicity (Figure 5.4b, d) exhibited starkly different behavior patterns from the diurnal signal. First, the convectively active quasi-2-day signal was prominent over the IO in addition to near Sumatra terrain at $100°E$. Second, and more importantly, the quasi-2-day signal did not always propagate as the diurnal signal. In fact, the quasi-2-day convective signals over the central IO occasionally exhibited no propagation and at times even eastward propagation during MJO1 in contrast to its diurnal counterpart, which almost always propagated from east to west. In addition to these features, the active quasi-2-day signal displayed a larger amplitude over a relatively large zonal scale (up to 1000 km), and at times during MJO1 appeared as a "checkerboard-like pattern" (similar to that in Figure 1.5a) with alternating areas and periods of enhanced and suppressed convection and clouds (e.g. in Figure 5.4b from 15–20 October between $60°E–75°E$, and from 22–25 October between $70°E–100°E$). Interestingly, the 2-day signals over Gan appeared in most instances to extend only to the eastern boundary of the DYNAMO ESA ($80°E$) and

18

were mostly disconnected with 2-day variability farther east, even as the active phase of MJO1 progressed through the region. This behavior is generally consistent with earlier findings in the IO during MISMO (Yamada et al. 2010) but is in contrast with the behavior of 2-day disturbances in the WPAC, which tend to progressively migrate eastward with the overall MJO convective envelope (Nakazawa 1988).
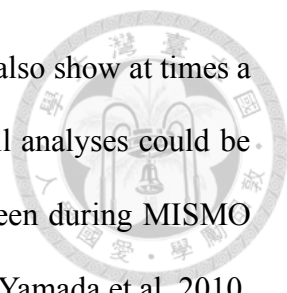
Worth noting in Figure 5.4c and Figure 5.4d is that the heavy rainfall (>1 mm/hr) of the seven quasi-2-day convective events over the DYNAMO ESA only occurred when both the diurnal and quasi-2-day signals were convectively active, hence the quasi-2-day intervals of occurrence as shown in Figure 4.1. On the other hand, the rainfall near Sumatra (90°E–100°E) corresponds well to the diurnal signal, but not necessarily to the quasi-2-day signal (Figure 5.4d), suggesting that the precipitation over the eastern IO was dominated by the terrain-induced diurnal convective activity (Yanase et al. 2017), while other factors controlled the rainfall patterns over the central IO.

These differences between quasi-2-day and diurnal signals are further demonstrated in time-longitude composite diagrams (Figure 5.6) for the seven convective events during MJO1. As evident from Figure 5.6, the quasi-2-day convective events associated with significant precipitation over Gan occurred only when the diurnal and quasi-2-day signals were both convectively active. The active diurnal signal propagated westward through the DYNAMO arrays (Figure 5.6a, c) with an estimated propagation speed of ~10–12 m/s, which largely explains the propagation speed of the convective events shown in Figure 4.2. In contrast, the quasi-2-day active signals appeared almost stationary, and the convective signals possessed a zonal scale up to about 1000 km (Figure 5.6b, d), a likely result of broadening stratiform clouds. In addition to the considerable amount of spatial range of the active clouds and significant precipitation, the quasi-2-day composite signal contributed 54.7% of the variance in cloud activity (43.5% in

19

precipitation) over Gan during MJO1.

As inferred from the above analyses, the quasi-2-day convective events observed over Gan during MJO1 were actually comprised of at least two modes of convective activity. One was the westward-propagating diurnal convective waves very likely corresponding to the westward-propagating IGWs with phase speed of 10–12 m/s (Takayabu 1994a,b; Takayabu et al 1996; Haertel and Kiladis 2004; Wheeler and Kiladis 1999). The other was the near-stationary quasi-2-day convective disturbances with zonal scale up to ~1000 km, which contributed approximately half of the convective variance over Gan during MJO1. Overall, the combination of both modes contributed substantially 67% to the variance of cloud activity over Gan during MJO1 (and about 65% in TRMM rain rate variance). As a result, the propagation of cloud clusters in the seven quasi-2-day convective events was regulated by diurnally-excited convective waves while the intensity and spatial range varied in quasi-2-day intervals.

To estimate the equivalent depth of the westward-propagating diurnal convective waves, we follow a similar approach to that taken in Takayabu (1994b). From Figure 5.6a we estimate the zonal scale of the diurnal disturbance to be ~1.05×10^6 m (or zonal wavenumber 38) as illustrated in Figure 5.7. The intrinsic frequency ($\omega_{int} = \omega_{abs} - kU$) is computed using $\omega_{abs} = 2\pi/1$day, k = $–2\pi/(1.05\times10^6$ m), and the zonal wind U = 3.25 m/s (taken as the 850-mean hPa at Gan for the period of interest) which results in $\omega_{int} =$ $9.22\times10^{-5}\,s^{-1}$ (or 1.27 cycles/day). These wave characteristics coincide with the dispersion curve for a westward-propagating n=1 IGW with an equivalent depth of ~20 m (Figure 5.8). Also, shown here is the result from Takayabu 1994b for the 2-day disturbance they analyzed using TOGA COARE observations. Despite the differences between the zonal and temporal scales of the disturbances in these studies, both waves have a similar equivalent depth of ~20 m.

The quasi-2-day-filtered signals in Figure 5.4 and Figure 5.6 also show at times a checkerboard-like pattern. This feature seen in the cloud and rainfall analyses could be interpreted in terms of the counter-propagating convective signals seen during MISMO which interacted to enhance rainfall locally on a 2–4 day time scale (Yamada et al. 2010, Figure 15, as shown in Figure 1.8). In few of the 2-day events depicted in Figure 4.1, it appears that an eastward propagating convective signal to the west of Gan encountered a westward propagating signal enhancing rainfall in the vicinity of Gan. The environmental wind structure (i.e., low-level westerlies underlying upper-level easterlies seen in Figure 6.6a) during MJO1 would support Yamada's mechanism of counter-propagating convective signals.

In addition to Yamada's mechanism, Chen and Houze (1997, Figure 19a, b, as shown in Figure 1.5) using TOGA COARE observations showed that the conceptual "diurnal dancing" process accounts for a checkerboard pattern of convective systems and a 2-day cycle of cloud activity at a given longitude. More precisely, Chen and Houze (1997) explain the observed cloud variability in terms of "a combination of 2-day IGWs and the diurnal dancing" (Figure 1.5b). In contrast to their findings, our analyses suggest that the quasi-2-day convective events during MJO1 were composed of westward-propagating diurnal convective disturbances and a quasi-2-day modulation of that convective signal as shown in the composites (Figure 5.6). That is, the 2-day IGWs were not necessarily a component for the propagating feature in these seven events, at least within the longitudes of the DYNAMO ESA. Instead, the diurnal convective waves controlled the propagation while those diurnal signals were modulated on a quasi-2-day time scale in the vicinity of Gan. Later analyses will show that the quasi-2-day periodicity is likely more related to the life cycle of the convective systems and associated boundary layer modification and recovery.

5.3   Spatial distribution of convective signals
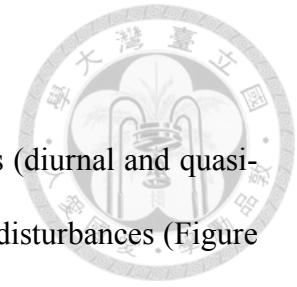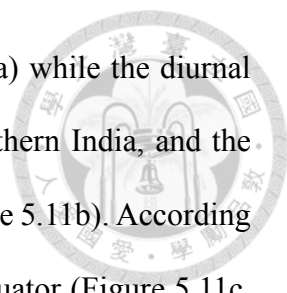
Maps in Figure 5.9 show where these two convective modes (diurnal and quasi-2-day) were most active during MJO1. The quasi-2-day convective disturbances (Figure 5.9a) preferentially occurred over open ocean and were mostly confined to near the equator between 10°N and 10°S, similar to that observed over the WPAC during TOGA COARE (Haertel and Johnson 1998, Figure 7, as shown in Figure 5.10), and the disturbances were present throughout the DYNAMO ESA maximizing near Gan during MJO1. On the other hand, the stronger diurnal disturbances (Figure 5.9b) were closely tied to the terrain of Sumatra Island, Southern India, and the coast of Sri Lanka, being about half the amplitude of the quasi-2-day disturbances over the central IO (Figure 3.1b and Figure 3.1c).

In general, compared to the diurnal variances, the quasi-2-day variances in IRBT (Figure 5.9c) and in TRMM rain rate (Figure 5.9d) were larger over the central equatorial IO and smaller near the coast of Sumatra. And the differences between the quasi-2-day and diurnal variances in TRMM rain rate were smaller than that in IRBT. It is not well understood at this point why the amplitude of the quasi-2-day variance was so large in proximity to Gan during DYNAMO, but it may be related to the MJO1 initiation and sea surface temperature (SST) distribution over the central IO as discussed in the next section.

5.4   Climatological characteristics of convective signals over the Indian Ocean

To determine how the DYNAMO results compare to other years, a climatology of quasi-2-day and diurnal variability using IRBT dataset from NOAA (0.07° resolution) is investigated for the October to December periods from 1998 to 2012 (15 years). Similar patterns of the variances are found for this longer period (Figure 5.11), in which the quasi-

2-day disturbances preferentially occurred over the IO (Figure 5.11a) while the diurnal disturbances were closely tied to the terrain of Sumatra Island, southern India, and the coast of Sri Lanka, showing smaller amplitudes over the ocean (Figure 5.11b). According to the averaged variances of IRBT and TRMM rain rate near the equator (Figure 5.11c, d), the variance of diurnal signals maximizes near 100°E while quasi-2-day convective signals become more apparent to the west of 95°E. On average, both signals show an overall decreasing trend in variance from the eastern IO toward the west.

The spatial patterns for each year from 1998 to 2012 are shown in Figure 5.12 (quasi-2-day) and Figure 5.13 (diurnal). Interestingly, the stronger quasi-2-day signals in the central IO as during DYNAMO period are also observed in certain years, e.g. 1999, 2000, 2006, 2007, 2009 and 2012. During other years, the stronger quasi-2-day signals are observed closer to the eastern IO as seen in the averaged pattern (Figure 5.11a). This difference in distributions of quasi-2-day convective disturbances is found to be generally correlated with the spatial distribution of SST over the eastern and western IO, i.e., the Indian Ocean Dipole (IOD; Saji et al. 1999). According to Saji et al. (1999), the index describing IOD, also known as the Dipole Mode Index (DMI), is defined by the difference in the SST anomaly between the tropical western IO (50°E–70°E, 10°S–10°N) and the tropical south-eastern IO (90°E–110°E, 10°S–Equator). As shown in Figure 5.14, during MJO1 the occurrence of quasi-2-day signals over the DYNAMO ESA is overall coincident with the warmer SST over the central IO and the positive IOD (DMI ~0.34). And during the positive phase of IOD such as October–December in 2006 (DMI ~0.63), relative warm SSTs occur in the central to western IO (60°E–80°E) as shown in Figure 5.15a, also during which the stronger quasi-2-day signals occur over the central IO (Figure 5.15b). On the other hand, during the periods when IOD is negative (e.g., late 1998 and late 2010, DMIs are –0.93 and –0.77, respectively), the quasi-2-day signals are

23

more prominent toward the eastern IO near 80°E–100°E (Figure 5.16 and Figure 5.17).
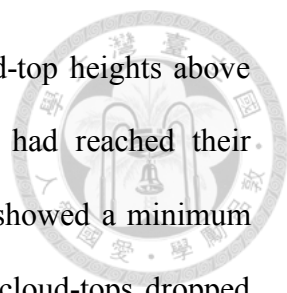
To explain the connection between the SST and quasi-2-day disturbances over the IO, it would certainly be a valuable exercise to investigate the climatology of these disturbances and perhaps compare them among different MJO and/or IOD phases. However, the DYNAMO period on which this study is focused represents the only time period where reliable computations of the heating, moistening, and other detailed aspects of the disturbances were available to accompany the satellite analyses. Given the large variance in the 2-day signals near Gan during DYNAMO, observations from that island should provide insight into the structure of the quasi-2-day convective disturbances. With the aid of the AMIE-Gan large-scale analyses and datasets from other observational platforms deployed at Gan (e.g., radiosondes, SPOL radar, CombRet radiative measurements), the vertical structures of the quasi-2-day convective disturbances are examined in Chapter 6.

Chapter 6 Composite Features of the Quasi-2-day Convective Disturbances

6.1 Cloud-top population from brightness temperature

Figure 6.1 shows 48-hour window composites of cloud-top population and rain rate over Gan. The composites are centered at 0 h as this time represents a minimum in IRBT, which from Figure 3.1 can be seen to be distributed throughout the diurnal cycle. The atmospheric cloudiness shows a clear oscillation with a period of 2-day in which different stages of cloud activity can be identified. During the first stage of the oscillation from −1 d to −9 h, the cloud-tops were generally low and mostly confined to below 700-hPa, indicating the convectively suppressed stage of the disturbances. Starting from −9 h, the composite cloud tops rose and the mean rainfall increased, indicating intensifying convection. Heavier rainfall commenced near −6 h and the composite rain rate peak occurred before 0 h. It is reasonable that heavier rain occurred when deep convective clouds were dominant in the convective events prior to their mature stage. Although the satellites are incapable of detecting shallow clouds beneath thick higher clouds, the broadening cloud-top population suggests the coexistence of different cloud tops besides the dominant deep convective clouds during this stage. This convective intensifying stage was similar to that observed and identified as the "initial convective tower stage" in Takayabu et al. (1996) with TOGA COARE observations (Figure 1.3). In Figure 6.1b the rainfall retrieved from SMART-R was lighter and the peak occurred earlier than that from TRMM. This is consistent with findings of Xu and Rutledge (2014) based on radar data from the R/V *Revelle*, where they found that TRMM 3B42 product overestimates rainfall during convectively active periods likely due to the abundance of high cloudiness.

25

At 0 h, most cloud clusters were well developed with cloud-top heights above 200-hPa (~220 K), and the quasi-2-day convective disturbances had reached their convectively mature stage while at the same time the mean IRBT showed a minimum peak. After 0 h the average rain rate decreased and the dominant cloud-tops dropped slightly to near 200-hPa (220–240 K) from +3 h to +6 h likely a result of trailing stratiform anvils (Takayabu et al. 1996; Chen and Houze 1997; Haertel and Johnson 1998; Zuluaga and Houze 2013). From +6 h to +18 h, the convective components of the quasi-2-day disturbances had mostly decayed around Gan with light rain and dominant cloud-tops between 250 K and 270 K for nearly 12 hours.

Four stages in the life cycle of the quasi-2-day convective disturbances over Gan during MJO1 can thus be identified in terms of cloud activity: suppressed, convective intensifying, mature, and stratiform. This is similar to the observations of TOGA COARE (Takayabu et al. 1996; Haertel and Johnson 1998) and is consistent with the "building-block" life cycle of MCSs proposed by Mapes et al. (2006).
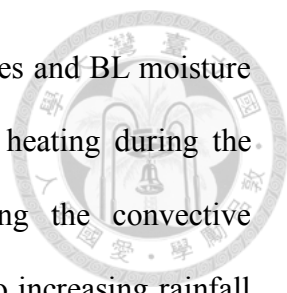
6.2   Basic fields from Gan radiosonde

Gan radiosonde moisture and thermodynamics fields of the quasi-2-day life cycle in convective disturbances are shown in Figure 6.2 and Figure 6.3. In the suppressed stage, the atmosphere was relatively dry with moisture accumulating near and within the BL (maximum near −12 h, as shown in Figure 6.2). Moisture then deepened and became abundant throughout the troposphere as the convection developed. Figure 6.3 shows warm anomalies at low levels in temperature field and mid-level positive pressure perturbations (represented in geopotential height anomalies) beginning near −1 d then ascending after −18 h. During the intensifying stage, the ascending warm anomalies and negative pressure perturbations are presumably associated with the cloud development

26

from shallow cumulus to deep convective clouds in intensifying stage (supported by Q_1 and Q_2 profiles, shown later in Figure 6.9). Meanwhile, the BL was relatively warm prior to the onset of heavier rainfall near –9 h, and relatively cool during the heavy rain period after –9 h for ~18 hours.

At 0 h, the atmosphere was moistest throughout the troposphere as the quasi-2-day convective disturbances reached their mature stage (Figure 6.2). From 0 h to +6 h, in addition to the warm cores in the convective towers (400–200 hPa) and the associated positive pressure perturbations (near 200 hPa), a cool anomaly appeared near and above the 200-hPa level (Figure 6.3). This feature is coincident with cloud-top radiative cooling shown later in Figure 6.7. A second cool anomaly is evident below 500 hPa, with a peak directly below the 0°C level, due to the melting and evaporative cooling. While moisture was abundant above the 0°C level, the lower troposphere began to dry and was dominated by the positive pressure perturbations after +3 h. Also, after the mature stage, the lower troposphere became relatively warm from +6 h to +18 h in the 900–700 hPa layer. These are likely signatures of mesoscale downdrafts which also caused "onion-type" profiles in the soundings during the stratiform stage (Zipser 1977) as shown in Figure 6.4 below 600–650 hPa. However, cool anomalies still existed in the BL around +12 h due to spreading cold pools from the evaporating precipitation. During the stratiform stage, a thin moist layer slightly below 0°C level related to the melting process under stratiform anvils (Johnson et al. 1996) can also be seen from +6 to +18 h (Figure 6.2).

The temperature variation in the BL showed a clear quasi-2-day oscillation within the 48-hour window (Figure 6.3), as well as the moisture variation in the BL (Figure 6.2). A phase diagram for moisture and temperature anomalies within and near the BL (≤900 hPa) was generated to represent the BL quasi-2-day cycle (Figure 6.5). As shown in the phase diagram, during early suppressed stage (–1 d to -15 h) both moisture and

27

temperature increase (the 1st quadrant) until the convection intensifies and BL moisture reaches the maximum near –12 h, indicating the moistening and heating during the suppressed stage when shallow convection is dominant. During the convective intensifying stage both the moisture and the temperature drop due to increasing rainfall (the 2nd quadrant). And as the convection reaches its mature stage, the moisture in the BL keeps decreasing while the temperature increases (the 3rd quadrant) as stratiform clouds become prominent. The BL moisture anomaly reaches a minimum and the temperature anomaly slightly increases during the stratiform stage as a result of the warming and drying from mesoscale downdrafts (the 3rd and 4th quadrants). Overall, the composite BL cool anomaly lasted for almost a day (from –9 h to +12 h) during the convective intensifying and mature stages, and the early stratiform stage (the 2nd and 3rd quadrant). This long BL recovery of quasi-2-day disturbances over Gan during DYNAMO supports the idea that the convective processes and the BL recovery can be key factors for the quasi-2-day periodicity observed in the disturbances, similar to the processes in MCSs observed during TOGA COARE in WPAC (Takayabu et al. 1996; Chen and Houze 1997).

The zonal wind field (Figure 6.6a) shows strong westerlies in the lower troposphere below 700 hPa with easterlies above during this active period of the quasi-2-day disturbances (Zhang and Yoneyama 2017). Prior to the mature stage, a westerly anomaly occurred in the lower troposphere (1000–800 hPa) near –6 h (Figure 6.6b). This westerly anomaly then shifted upward as the quasi-2-day convection developed with a peak in the upper troposphere (200–300 hPa) near +9 h. This result suggests an upward transport of westerly momentum associated with the quasi-2-day convective disturbances over Gan during MJO1. These zonal wind anomalies are consistent with low-level convergence prior to 0 h (Figure 4.2) and upper-level divergence centered around 0 h to support deep convection during this period (Figure 6.8, later). There is also evidence from

28

Figure 6.6b and Figure 6.8 of a downward transport of easterly momentum within stratiform precipitation regions of the disturbances (from +6 h to +18 h), consistent with the TOGA COARE Doppler radar analyses of Houze et al. (2000), which show the existence of such transport in what they call the "westerly onset region" of the MJO Kelvin-Rossby circulation. Liu and Wang (2012) have argued that easterly momentum transport by 2-day waves serves to slow down and convectively enhance moist Kelvin waves or the MJO, so such transports may play an important role in the life cycle of the MJO itself.

6.3   Composite feature of radiative forcings

The radiative impacts of clouds and moisture to the quasi-2-day convective disturbances are considered in Figure 6.7 with composites of the total (Q_R), longwave (LW) and shortwave (SW) cloud radiative forcings (CRF) obtained from the CombRet dataset. The total cloud radiative cooling (Figure 6.7a) maximized at upper levels above 200 hPa at 0 h as a result of the strong cloud-top longwave cooling, with peak rates approaching 5 K/day (Figure 6.7b). The CRF SW heating profiles (Figure 6.7c) show large peaks directly beneath the cloud tops near 200-hPa (Webster and Stephens 1980) in the −6 h to 0 h timeframe. Presumably, these large heating rates are related to the events with 0 h occurring during the daylight hours when SW effects would be present (see Figure 3.1 for local times of 0 h occurrences). For these cases, this upper-level SW heating peak would promote a stabilization of the lapse rate and a weakening of the deep convection (Randall et al. 1991) that would also enhance midlevel convergence and upper-level divergence (Gray and Jacobson 1977), thereby assisting the transition to stratiform precipitation. During the mature stage, the CRF composites show a slight downward-sloping pattern in the upper troposphere as a result of the trailing stratiform

clouds, similar to the squall line structure found in Johnson et al. (1990). From the intensifying stage to the stratiform stage, CRF LW heating in the lower troposphere was dominant from –9 h to +18 h.

Although the cloud radiative forcings are prominent as the quasi-2-day convection intensifies and reaches its mature stage, fewer impacts are observed during the stratiform stage after +6 h. To better understand the structure and variation of the quasi-2-day convective disturbances, we make use of AMIE-Gan large-scale objective analysis data to investigate the convective features during MJO1. Although the dataset is representative of the region with only a 150-km radius around Gan, considering the propagation speed (10–12 m/s) and the zonal scale (~1000km) of the quasi-2-day events, it is capable of sampling variability within the quasi-2-day convective disturbances.

6.4　Derived fields based on Gan radiosonde and AMIE-Gan large-scale objective analysis

Figure 6.8 and Figure 6.9 include the 48-hour window composites for horizontal wind divergence and large-scale vertical motion, apparent heating (Q_1), and apparent drying (Q_2) from AMIE-Gan objective analysis. During the convective intensifying stage (from –9 h to 0 h) upward motion, associated with low-level convergence and upper-level divergence, dominated the troposphere with a maximum around 600 hPa (Figure 6.8). As the convection matured, the updrafts shifted upward, and low-level downdrafts due to stratiform precipitation dominated over the updrafts. Low-level divergence maximized in the BL during the mature stage (after +3 h), similar to the findings of Zuluaga and Houze (2013). In the mature stage and later in the stratiform stage, a separate peak in updrafts was present above 0°C level while mesoscale downdrafts dominated the lower troposphere as generally observed in other stratiform regions (Cifelli and Rutledge 1994;

30

Uyeda et al. 1995).

Starting from −9 h, positive Q_1 was observed throughout the troposphere with a maximum between 600 and 500 hPa around −6 h and −3 h, which then transitioned to near 400 hPa at 0 h (Figure 6.9a). The principal Q_2 peak was found below the 600-hPa level with maximum at −3 h (Figure 6.9b) when the highest rain rate occurred (Figure 6.1b). The results are consistent with Yanai et al. (1973) that the vertical separation of the Q_1 and Q_2 peaks is indicative of strong convective eddies fluxes which prevailed during the convective intensifying stage from −9 h to 0 h (Figure 6.9c).
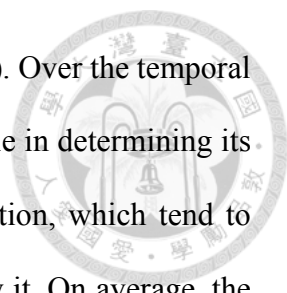
After 0 h, the principal Q_1 peak shifted upward above the 0°C level between 500 and 300-hPa levels while negative Q_1 was prevalent below the 0°C level from +3 h to +15 h (Figure 6.9a). In Q_2 positive peaks occurred above 400-hPa level around +9 h with negative values found mostly below the 700-hPa level from +6 h to +18 h (Figure 6.9b). These results reflect the typical top-heavy signatures of stratiform precipitation in which stronger heating and drying occur in the upper troposphere while cooling and moistening due to melting and evaporation occur in the lower troposphere (Johnson 1984; Houze 1989, 1997). There is an upward shift in the MSF flux during the developing stages of the quasi-2-day disturbances (Figure 6.9c), with another peak in the stratiform stage at +6 h. This latter feature likely reflects the remnant convective components which occurred after 0 h in some of the events as seen in NCAR S-Pol radar data (examples as shown in Figure 6.10).

The disturbance composite equivalent potential temperature (θ_e) anomaly field is shown in Figure 6.11a. From −18 h to −6 h, the atmosphere was unstable with higher θ_e in the BL as deep convection starts to develop. At −6 h, θ_e in the BL transitioned from relatively high to relatively low as the rain became heavier. Afterward, the lower troposphere (900–700 hPa) gradually became more stable with low θ_e during the mature

31

stage due to a transport of low θ_e by downdrafts (e.g., Zipser 1977). The low BL θ_e lasted for almost 18 hours (from −6 h to +12 h) in the life cycle of the disturbances. The prevalent, long-lasting stable BL over Gan, a result of the convective process, impacted the recovery of lower troposphere and the occurrence of the next round of convection over that region especially during the stratiform stage, similar to the convective processes during TOGA COARE in WPAC (Takayabu et al. 1996; Chen and Houze 1997).

The atmospheric stable layers based on Gan radiosonde data also show variation over the life cycle of the quasi-2-day convective disturbances (Figure 6.11b). Tropical convection often shows a trimodal structure in the vertical profiles of cloud population, divergence, and cloud detrainment as depicted in the conceptual model of Johnson et al. (1999, Figure 13, as shown in Figure 6.12). This structure suggests the impact of three major stable layers of the tropical atmosphere from top to bottom, the tropopause inversion layer, the melting stable layer near 0°C level, and the trade-wind stable layer in the lower troposphere (Schubert et al. 1995; Johnson et al. 1996, 1999; Kikuchi and Takayabu 2004). During MJO1 the trimodal structure is clearly identified according to the temperature lapse rate profiles (Figure 6.11b). The tropopause inversion layer occurred mostly above 125 hPa except during the mature stage when gravity wave features excited by the MJO convective envelope lead to its lowering (Johnson and Ciesielski 2013). The melting stable layer generally occurred near and slightly above 0°C level and was strongest during the mature and stratiform stages when the melting process was most prevalent over large areas.

A trade-wind-like stable layer is observed between 700 and 900 hPa with a more complex variation than the other two layers. Previous modeling studies have suggested that the overall height of the trade-wind stable layer is controlled by both local thermodynamic processes (Albrecht et al. 1979; Sarachik 1985) and large-scale

32

dynamical adjustment across different latitudes (Schubert et al. 1995). Over the temporal scale of ~2-day, it appears that local processes played a dominant role in determining its height. These processes include radiative effects and moist convection, which tend to deepen the trade layer, while large-scale subsidence tends to shallow it. On average, the height of the trade stable layer was near 800 hPa throughout MJO1, but during the suppressed stage of the quasi-2-day disturbances (from -1 d to -9 h), it moved progressively upward to near 700 hPa. This period was marked by overall upward motion in the lower troposphere (Figure 6.8), weak cloud-top radiative cooling near 600 hPa (Figure 6.7) and unstable conditions at low levels (Figure 6.11a) all of which would promote a deepening trade layer. After -6 h, but particularly after 0 h, low-level subsidence, mid-level radiative warming and BL cooling predominated resulting in a reduction in the trade layer depth. In the mature stage (from 0 h to $+6$ h), the trade layer height showed the largest variance as a result of more downdraft-induced complex temperature profiles in the lower troposphere. The trade layer heights were generally low (~900 hPa) in the early stratiform stage (from $+6$ to $+12$ h) as cooler BL θ_e air and subsidence dominated.

The composites of convective available potential energy (CAPE) and convective inhibition (CIN) derived from Gan sounding data are shown in Figure 6.11c. Although these stability indices exhibit considerable variability among the seven cases, their composite structure is quite reasonable with larger CAPE prior to the mature stage and a minimum at 0 h, as also shown for the composite MJO life cycle by Xu and Rutledge (2014). In contrast, the composite CIN was relatively small before the mature stage and became larger after 0 h during the mature and stratiform stages due to enhanced stability in the lower troposphere.

The composite quasi-2-day disturbance vertical heating structures, kinematic and

33

thermodynamic fields, radiative profiles, and modification of the boundary layer suggest that these phenomena have properties resembling those of individual tropical MCSs, evolving from shallow cumulus to congestus to deep convection to stratiform precipitation (e.g., Houze 1997; Zipser 1977), as well as 2-day disturbances observed in the western Pacific (Takayabu et al. 1996; Chen and Houze 1997). Such structures and life cycle behavior are observed not only on the time and space scales of individual MCSs and quasi-2-day disturbances but also are characteristic of phenomena all the way up to the scales of convectively coupled Kelvin waves and the MJO itself (Mapes et al. 2006; Kiladis et al. 2009).

Chapter 7   Interpretation of Quasi-2-day Convective Disturbances

Previous studies of 2-day disturbances in the WPAC (e.g., Takayabu et al. 1996; Chen and Houze 1997; Haertel and Johnson 1998) and the IO (Yamada et al. 2010) have shed considerable light on these phenomena. Drawing upon these studies as well as the current findings reported in this study, we offer a new interpretation of mechanisms for the quasi-2-day disturbances observed during the October MJO in DYNAMO.

As a first consideration, we relate our results to the Chen and Houze (1997) "diurnal dancing" paradigm (Figure 1.4 and Figure 1.5). The very slow eastward drift of the origin of the diurnal signal affecting Gan (~1 m/s; Figure 5.4a) differs significantly from the 10–15 m/s eastward movement illustrated in Chen and Houze (1997, Figure 19b, as shown in Figure 1.5b). According to their study, that paradigm was based on a series of convective systems occurring during the period 11–16 December 1992 (Figure 1.6). Moreover, there was mostly easterly flow with little vertical shear throughout the troposphere during that period (Chen et al. 1996, Figure 2, as shown in Figure 7.1), in contrast with DYNAMO where during the October MJO there were westerlies below 700 hPa and easterlies above (Figure 6.6a). This much slower eastward movement of the diurnal signal in DYNAMO yields an ~1-day signal downstream to the west rather than a quasi-2-day signal, so the "diurnal dancing" argument (Figure 1.5b) that may have been relevant to the TOGA COARE period they studied does not fit the DYNAMO conditions. It is more likely that for some reason yet to be fully understood, a diurnal signal initiates
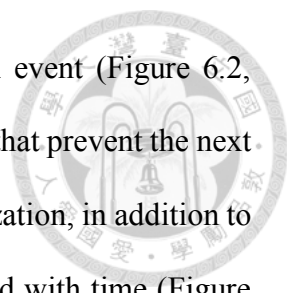
between 80°E and 85°E that is separate from that coming off Sumatra[1], moves westward at 10–15 m/s and crosses the longitudes of Gan where it encounters an environment that contributes to a quasi-2-day time periodicity.
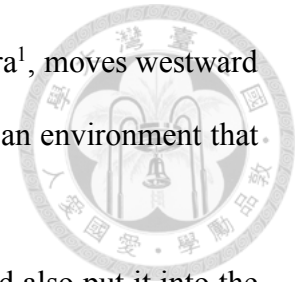
In an attempt to understand the quasi-2-day signal at Gan and also put it into the perspective of convective phenomena with similar periodicity observed during MISMO as reported by Yamada et al. (2010), S-Pol radar images for the seven individual events have been examined. Several of these DYNAMO cases exhibited eastward movement of convective cells with westward movement of stratiform anvils, similar to Yamada et al.'s findings. Examples include the eastward moving convective cells to the north of Gan along with slightly westward expanding stratiform region observed by NCAR S-Pol on 24 October (Figure 7.2), and the eastward moving convective system to the east of Gan on 28 October (Figure 7.3), which also shows a slight southward propagation. In both cases, the convective cells possessed a propagation speed of approximately 13–14 m/s. However, other cases exhibited convective cells moving in different directions (e.g., northeastward shifting convection observed on 22 October as shown in Figure 7.4). Regardless of the motion of the convective cells, however, on average the stratiform anvils in each case moved from east to west due to easterly flow aloft (Figure 6.6a).

Thus, a different scenario for the quasi-2-day variability is proposed (Figure 7.5). Diurnally driven convective events initiate between 80°E and 85°E and move westward at 10–15 m/s, arriving at the longitude of Gan approximately one day later. Generally, only every other diurnal signal is amplified, leading to a quasi-2-day signal at Gan. The

---

[1] Preliminary analyses of possible causes suggest that the variable SST over the IO during this period may be a potential explanation for the initiation of the diurnal signal between 80°E and 85°E, although thorough investigation of this possibility is beyond the scope of current study.

stabilization of the BL and lengthy recovery from the first diurnal event (Figure 6.2, Figure 6.3, Figure 6.5, Figure 6.8, and Figure 6.11) are likely factors that prevent the next diurnal event from amplifying. Contributing to this prolonged stabilization, in addition to convective-scale downdrafts, are stratiform anvils that drift westward with time (Figure 6.6). These anvils, which produce light precipitation and cloud shading, cross the longitudes of Gan and modify the BL there. However, even after they pass to the west, the low-level westerlies advect the modified low-levels air eastward, helping to contribute to the slow BL recovery observed at Gan. Thus, the idea advanced by Chen and Houze (1997) that BL modification is a factor in the quasi-2-day periodicity is supported by our findings, though the different vertical shears and eastward speed of movement of the origin of the diurnal signals for the two periods of study in the two ocean basins argues for a different interpretation of the quasi-2-day periodicity.

Chapter 8   Summary and Concluding Remarks
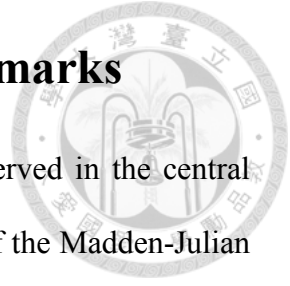
Convective events with a quasi-2-day periodicity were observed in the central equatorial Indian Ocean (IO) during the convectively active phase of the Madden-Julian Oscillation (MJO) from 15 to 31 October 2011 (MJO1) in the DYNAMO/AMIE/CINDY 2011 (DYNAMO) field campaign. Seven quasi-2-day convective events with significant convective activity were identified over Gan Island, which were analyzed with the aid of various observational platforms including radiosondes, radar, satellite, and surface observations. Properties of the convective features and the atmospheric structures of these events are summarized as follows.

(1) Seven convective events were identified over Gan as westward-propagating convective episodes which moved through the central IO repeatedly in a quasi-2-day interval during MJO1. The propagation speed of these convective signals was estimated by satellite infrared brightness temperatures (IRBT) to be 10–12 m/s, which is similar to that observed over the equatorial WPAC during TOGA COARE (10–19 m/s; Haertel and Johnson 1998; Takayabu 1994b). However, the zonal scale of propagation was approximately 1000–1500 km, less than that found during TOGA COARE (2000–4000 km; Chen et al. 1996; Chen and Houze 1997; Clayson et al. 2002).

(2) By isolating the quasi-2-day (1.6–3 day) and the diurnal (0.9–1.2 day) frequencies, spectral analyses reveal that the seven quasi-2-day convective events were comprised of two primary modes of convection, (i) a westward-propagating diurnal convective signal with phase speed of 10–12 m/s, very likely corresponding to an n=1 westward-propagating IGWs with an equivalent depth of 20 m (Takayabu 1994a,b; Takayabu et al 1996; Wheeler and Kiladis 1999; Haertel and Kiladis 2004), and (ii) a quasi-2-day convective signal having an ~1000 km zonal scale that modulated the diurnal

signals in the vicinity of Gan. The latter mode strongly influenced the magnitude and the spatial distribution of the precipitation and contributed to over half of the cloud variance (54.7%) over Gan during MJO1.

(3) The horizontal distributions of the two convective modes, as determined by IRBT variance, were different over the IO during MJO1. The quasi-2-day convective disturbances were prominent over the open ocean and near Sumatra but were confined to near the equator between 10°N and 10°S, similar to that in the TOGA COARE observations (Haertel and Johnson 1998). The convective variance on the diurnal time scale was closely tied to the terrain of Sumatra Island, Southern India, and Sri Lanka, and possessed a much smaller amplitude and spatial scale than that of the quasi-2-day disturbances over the central IO.
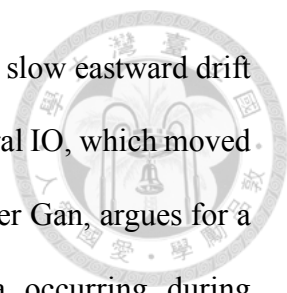
(4) In the 48-hour window composites (–24 h to +24 h) of moisture and cloud activity centered at the times of the lowest averaged IRBT (0 h) in the 150-km region over Gan, four stages of convection were identified in the life cycle of the quasi-2-day convective disturbances, (i) a convective suppressed stage (from –1 d to –9 h) with moisture confined in the lower troposphere, (ii) a convective intensifying stage (from –9 h to 0 h) in which convection transitioned to dominant deep convective clouds, (iii) a mature stage (from 0 h to +6 h) when convective systems were well-developed and transitioned from convective to stratiform precipitation, and (iv) a stratiform stage (from +6 h to +18 h) when most of the convective elements decayed into stratiform systems dominating much of the 150-km region over Gan. This life cycle represents a similar pattern not only to mesoscale convective systems (MCSs) life cycle but also to that observed on longer time scales all the way up to that of the MJO (Kiladis et al. 2009).

(5) Radiative forcings and apparent heat sources and moisture sinks for the composite quasi-2-day disturbances have been determined. Top-heavy cloud radiative

heating may play a role in promoting the longevity of the stratiform region after the disturbance mature stage. Diagnosed heat sources and moisture sinks are consistent with the shallow-to-deep-to-stratiform transition within the composite disturbances. The long duration of low BL θ_e air during the stratiform stage supports the notion that the life cycle of the MCSs may be an important factor contributing to the quasi-2-day periodicity of the disturbances over Gan along the lines proposed by Chen and Houze (1997).

The schematics of convective activity in the quasi-2-day convective disturbances during DYNAMO (Figure 7.5) is similar to that depicted in the schematic diagram presented in Takayabu et al. (1996, Figure 19, as shown in Figure 1.3) using TOGA COARE observations. Both campaigns showed the convection to have many common features with long-lived convective systems including a rather long convective life cycle and duration of the stratiform stage. Some of the seven events indeed were also characterized by the passage of squall-line systems as observed from the NCAR S-Pol radar data at Gan (Figure 7.2 to Figure 7.4).

The interpretation of the quasi-2-day disturbances within the convective envelope of MJO1, much like those originally identified by Nakazawa (1988), is that they are manifestations of westward-propagating, diurnal disturbances (very likely IGWs) whose convective signal becomes modulated over the central IO on a quasi-2-day time scale, a combination of the propagating diurnal IGWs and the quasi-2-day convective activity. There is evidence, in at least some of the cases, that counter-propagating cloud systems with height were present that owed their existence in part to strong vertical shear (westerlies at low levels, easterlies aloft), as hypothesized by Yamada et al. (2010). Composites of the quasi-2-day disturbances support the idea that the quasi-2-day intervals of occurrence may be a consequence of the longer time scale of mesoscale convective system development and BL modification, a concept invoked by Chen and Houze (1997)

to account for what they called "diurnal dancing". However, the very slow eastward drift of the initiation locations of the diurnally driven signals over the central IO, which moved westward and contributed to quasi-2-day convective disturbances over Gan, argues for a different interpretation of the mechanisms for these phenomena occurring during DYNAMO (described in Chapter 7) that incorporates ideas from earlier TOGA COARE (Takayabu et al. 1996; Chen and Houze 1997) and MISMO (Yamada et al. 2010) studies.

Nevertheless, questions remain regarding a number of aspects of these phenomena. Why do quasi-2-day convective disturbances prevail during the convectively active phases of some MJOs but not others? For example, why were the disturbances so prominent over the DYNAMO array during the October MJO, but not the November MJO? What environmental conditions are needed to sustain these disturbances and what determines their horizontal scale? What roles do quasi-2-day convective disturbances play in the moistening of the atmosphere and momentum transport during the onset stage of the MJO? Further analyses with the radar data from Gan and cloud-resolving numerical simulations may help us characterize the convective structures of these disturbances and gain a better understanding of this intriguing phenomenon.
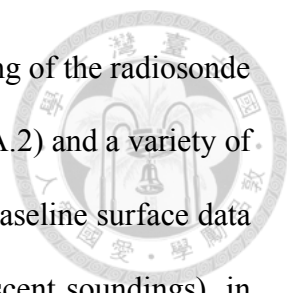
APPENDIX A   Upper-air Radiosonde Observations and Data Quality Control in DYNAMO

The upper-air sounding network for DYNAMO (as illustrated in Figure 1.9) has provided an unprecedented set of observations for studying the MJO along with its convective activities over the IO. The network covers the tropics from eastern Africa to the western Pacific with 72 rawinsonde sites and 13 aircraft missions. In total 25,938 soundings were collected from this network during the DYNAMO extended observing period (EOP) from October 2011 to March 2012, and slightly more than half of those (13,074) are at high vertical resolution (hi-res; Ciesielski et al. 2014).

The primary component of this sounding network is six core sounding sites in the central IO that formed two quadrilateral sounding arrays (Figure 2.1). These arrays were intact for the DYNAMO SOP from 1 October to 30 November with an overall success rate ~98% (defined as the ratio of successful sounding launches to those planned). Five of the six core sites used research-quality Vaisala RS92 radiosondes (Table A.1). And as the main focus of this study, Gan Island located on a vertex of both the northern and southern sounding arrays (73.15°E, 0.69°S), was a supersite where multiple radars were deployed (Yoneyama 2013, Figure 3, as shown in Figure A.1) and the reliable computations of the heating, moistening, and other detailed observations of the disturbances were made based on various instruments in addition to the soundings (Yoneyama 2013).

In order to meet the scientific goals of the experiment and to create the "best possible" set of radiosonde observations, particular attention is given to the quality

control of the radiosonde dataset. Rigorous post-field phase processing of the radiosonde data includes several levels of quality checks (Table A.2 and Figure A.2) and a variety of corrections that address a number of issues (e.g., daytime dry bias, baseline surface data errors, ship deck heating effects, and artificial dry spikes in slow-ascent soundings), in which a significant effort was directed toward improving the quality of the humidity observations.

The quality control (QC) procedure applied to the hi-res radiosonde data follows the schemes outlined in Loehrer et al. (1996) and Ciesielski et al. (2012). A flowchart is presented by Ciesielski et al. (2012, Figure 1, as shown in Figure A.2) outlining this procedure with four stages (or levels) of data processing. The first step was to convert the raw level 0 (L0 in Table A.2) sounding data from the various data formats created by the different data systems into a single, easily utilized format that we refer to as level 1 (L1) processing. All hi-res radiosonde data (L1 through L3) contain the basic fields (pressure, height, temperature, relative humidity, and winds) as well as ancillary fields (e.g., sonde ascent rate and geolocation information) as a function of time. Header lines in each sounding include the exact time of the radiosonde launch and the radiosonde serial number, which provide information on the manufacture date and can prove helpful in developing corrections.

These efforts were followed by level 2 (L2) processing in which the hi-res soundings were passed through a series of automated QC algorithms (Loehrer et al. 1996) and visual inspection to systematically detect suspicious data values. An example of such an automated tool, the Atmospheric Sounding Processing Environment (ASPEN) developed by the NCAR Earth Observing Laboratory (EOL) can remove egregious data points based on several QC checks, filter the winds, compute geopotential height, smooth pressure, and write out the processed hi-res data in one of many convenient formats. This

43

software and its complete documentation can be obtained online (see www.eol.ucar.edu/isf/facilities /software/aspen/aspen.html).

In level 3 (L3) processing, errors and biases in the data especially for humidity observations were identified and corrected, if possible. This level of processing resulted in the final high-resolution datasets to which corrections have been applied. To evaluate the humidity corrections, two different correction algorithms—the DigiCORA (proprietary correction algorithm built in the Vaisala ground station software) and Global Climate Observing System Reference Upper-Air Network (GRUAN; open-sourced correction algorithm containing uncertainty estimates; Immler et al. 2010; Immler and Sommer 2011; Dirksen et al. 2014)—are examined specifically for Vaisala RS92 radiosondes at Gan (and other sounding sites as described in Yu et al. 2015).

The analysis of mean RH profiles for Gan as shown in Figure A.3 suggests that both daytime and nighttime DigiCORA-corrected measurements lie within the uncertainty of the GRUAN measurements (left panels in Figure A.3), and the GRUAN- and DigiCORA-corrected RHs are statistically consistent at nearly all levels (right panels in Figure A.3) according to the consistency testing approach identical to that of Immler et al. 2010 (Yu et al. 2015).

To further evaluate the corrections, total-column precipitable water (TPW) retrieved from two radiosonde-independent data sources, i.e., ground-based global positioning system (GPS) estimates and microwave radiometer (MWR), are used. Figure A.4 shows a comparison over the diurnal cycle for Gan between the uncorrected and corrected radiosonde estimates of TPW along with the GPS and MWR estimates. This analysis considers only the times when all estimates are available with the number of comparison observations in each period shown along the bottom of the top panel. Also shown here is the uncertainty range of TPW based on the uncertainty of GRUAN RH

44

measurements. To calculate the uncertainty range of TPW, the mean vertical profiles of RH uncertainty range were converted to mixing ratio and then integrated through the entire column.

According to Figure A.4, excellent agreement was found at all sites between radiosonde and MWR values of TPW. Relative to the MWR estimates, all sounding corrections show a small (<2%) daytime dry bias and a similarly small nighttime moist bias. These differences are well within the uncertainties provided as part of the GRUAN data and suggest that the correction algorithms examined herein perform well at Gan (and over a wide range of tropical moisture conditions as shown in Yu et al. 2015). On the other hand, GPS TPW shows a systematic dry bias relative to the corrected radiosonde and MWR estimates of ~5% (or about 2 mm).

Finally, after the level 3 corrections, in level 4 (L4) processing a more "user-friendly" version of the sounding dataset was created with QC flags assigned to each variable, providing a measure of the data reliability. L4 processing was performed on sites with both GTS resolution and hi-res data, where L3 hi-res data were vertically interpolated to create values at uniform pressure intervals, specifically at 5-hPa. Suspicious data were identified through application of objective QC test as in Loehrer et al. (1996) and a subjective adjustment of QC flags by visual inspection (Ciesielski et al. 2012). While tedious, visual inspection was necessary to ensure a research-quality dataset, since subtle errors in radiosonde data (e.g., superadiabatic layers near cloud top due to wet bulbing effects, layers of suspicious wind shear, boundary layer abnormalities, etc.) are often difficult to identify with objective procedures. By flagging suspect data values, the reliable data are easily retrievable with the users deciding what level of quality is acceptable for their analyses.

In terms of performance, considering both quantity and quality of upper-air

radiosonde observations, operations in DYNAMO should be considered an extraordinary success, which is due to countless students, staff, and scientists from many agencies and universities in the United States, Japan, the Maldives, and Taiwan.
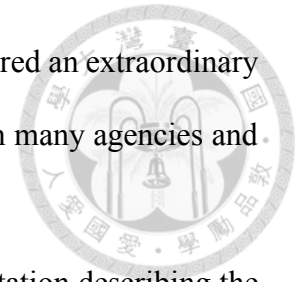
All radiosonde data described herein, including the documentation describing the processing performed at each site, are available from the EOL DYNAMO data archive online (http://data.eol.ucar.edu/master_list/?project=DYNAMO). This part of the study on DYNAMO upper-air radiosonde observations and data quality control has been published, more discussion and details can be found in Ciesielski et al. (2012; 2014) and Yu et al. (2015).

APPENDIX B Statistical Significance of the Quasi-2-day Convective Disturbances during DYNAMO
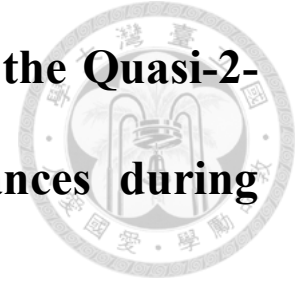
During DYNAMO SOP from October to November 2011, two MJO convective envelopes passing over Gan were observed and identified as MJO1 in October (15–31 October 2011) and MJO2 in November (15–30 November 2011) respectively. These two MJOs were certainly different as documented in Zhang et al. (2013) and Johnson et al. (2015). The main reason that the analysis during MJO2 was not included in this study is that the variances of both diurnal and quasi-2-day convective signals (IRBT) over Gan are not statistically at the 95% confidence level with p-values 6.38×10^{-12} and 6.85×10^{-8} for diurnal and quasi-2-day oscillation, respectively (Figure B.1). In fact, as seen in Figure B.2, the spectral power of the convective signal during MJO2 is less significant than the red noise spectrum at the 95% confidence level (Figure B.2, right panel); while during MJO1 (Figure B.2, left panel) both the diurnal and quasi-2-day signals are significant at the 95% level. Similar results are found in TRMM rain rate analysis (Figure B.3).

Even though both diurnal and quasi-2-day convective signals were robust during MJO1, as stated in Chapter 5, the variance of diurnal oscillation was statistically weaker than that of quasi-2-day oscillation over Gan at the 95% confidence level (p-value = 2.4×10^{-22}). Nevertheless, it is apparent that the quasi-2-day convective signal was robust during MJO1 and less significant during MJO2. As a result, despite the small sample size, the seven quasi-2-day convective disturbances observed at Gan during MJO1 in DYNAMO SOP are the focus of this study.

In order to answer the question of whether these seven selected convective events

represent common features of quasi-2-day disturbances, the standard deviations (stdev) of the composites were examined. Figure B.4 shows the composite of IRBT stdev among seven cases (shaded) and the area with IRBT composite <240 K (green hatched). The significance test (t-test) suggests that the stdev within the green hatched region (IRBT <240 K) is significantly less than the overall stdev at the 95% confidence level (p-value = 3.6×10^{-25}). This indicates that the selected seven convective events share statistically significant common zonal features of propagating quasi-2-day perturbations when the IRBT is lower due to higher cloud tops associated with deeper convection.

For the vertical structures from Gan radiosonde, the t-test for the stdev of RH from Gan radiosonde (Figure B.5) suggests that the stdev is significantly smaller when the RH is higher than 75%. Throughout the convective intensifying and mature stage, the stdev is smaller than the overall stdev at the 95% confidence level (p-value = 0.0004), indicating a strong commonality in the vertical moisture structures among the seven selected cases when the convection is active. It does show some larger deviations during the stratiform stage, but according to Figure B.5 the impacts occur at higher altitude, the seven cases are more consistent in the lower troposphere where the effects of stratiform clouds and the BL modulation occur.

Similar analyses were also applied to the composites of IRBT vertical structure. The t-test suggests that for the averaged vertical cloud top population >6 %, the seven individual cases as shown in Figure B.6 have common vertical structures to the composite (top left in Figure B.6), i.e. the stdev among the seven cases are significantly small at the 95% confidence level (p-value = 0.03).

Similar results come from analyses on ω, Q_1, and Q_2 (Figure B.7 and Figure B.8), which suggest that the seven convective events show a statistically similar pattern (smaller stdev at the 95% confidence level) when ω is smaller than –4 hPa/hr and larger

48

than +2 hPa/hr (p-value = 0.008 and 0.003, respectively), and Q_1 (Q_2) is larger than 4 K/day with p-value = 0.0028 (0.02).

In summary, the seven cases exhibit strong commonality with the composite being the best representative of individual events during periods when the convection is developing and more active. In addition, the seven quasi-2-day convective events display differences from a Eulerian view at Gan due to differences in smaller-scale convection along with the slow eastward propagation of the MJO1 convective envelope.

APPENDIX C   Chapter 7 Interpretation of Quasi-2-day Convective Disturbances (Chinese Version) 準雙日對流擾動之詮釋

　　承襲過去在西太平洋與印度洋上準雙日對流擾動的觀測（Takayabu et al. 1996；Chen and Houze 1997；Haertel and Johnson 1998；Yamada et al. 2010），本研究根據 DYNAMO/AMIE/CINDY 2011（DYNAMO）實驗在印度洋的觀測提出一項新的詮釋，解釋在 2011 年十月 Madden-Julian Oscillation（MJO）對流活躍期間（MJO1），在 Gan Island 所觀測到的準雙日對流擾動機制及其特殊發生週期。

　　過去根據 TOGA COARE 實驗，Chen and Houze （1997）曾利用 1992 年十二月 11 日至 16 日出現在赤道西太平洋的一系列對流活動，提出所謂 "diurnal dancing"（圖 1.4、1.5）機制解釋準雙日對流擾動。然而，在 TOGA COARE 期間十二月所發生的 MJO 對流系統其東行速度約為每秒 10–15 公尺（圖 1.5b、1.6），而 DYNAMO 期間十月下旬通過中印度洋的 MJO 對流系統，則以約為每秒 1 公尺（圖 5.4a）的速度向東傳遞。此外，在 TOGA COARE 準雙日對流擾動發生期間，赤道西太平洋主要是受盛行東風影響、環境垂直風切較小（圖 7.1）；相較於在 MJO1 期間，赤道中印度洋 700 百帕以下的低對流層盛行西風、以上則盛行東風，垂直風切較大（圖 6.6a）。在此環境底下，較小尺度的西行單日變化擾動受向東緩慢移行的 MJO 對流系統控制，在 Gan Island 附近呈現單日變化、向西傳遞的對流訊號。此結果與 Chen and Houze （1997）的解釋有所不同，顯示根據 TOGA COARE 觀測所提出的機制並不能完全解釋 DYNAMO 期間的準雙日對流擾動。事實上，DYNAMO 觀測顯示在 MJO1 期間，除了在東印度洋受蘇門答臘島地形所激發的單日變化擾動之外，在赤道中印度洋（東經 80 度至 85 度）洋面上受其他可能原因激發的單日變化對流訊號，以每秒 10–15 公尺的速度向西傳遞並通過 Gan Island 附近，在該區域受環境影響，對流的發生週期被調整為準雙日。

　　有鑒於赤道中印度洋與赤道西太平洋不同的風切環境，本研究也利用部署在 Gan Island 的 NCAR S-Pol 雷達，分析 MJO1 期間的七組準雙日對流擾動個案。S-Pol 雷達分析顯示，MJO1 期間的部分準雙日對流擾動個案當中出現對流胞向東

移行、高層層狀雲系向西傳遞的對流系統發生，類似 Yamada et al.（2010）所提出的準雙日對流擾動配置，例如：十月 24 日及 28 日的個案（圖 7.2、7.3），當中對流胞以約每秒 13–14 公尺的速度向東移動。然而，七組個案當中仍有部分個案顯示不同的對流胞移行方向，例如出現在十月 22 日個案中向北移動的對流胞（圖 7.4）。即便七組個案包含了不同的對流胞移動方向，所有個案當中的層狀雲及雲砧都受到高層東風的影響（圖 6.6a）由東向西傳遞。

　　因此，針對準雙日對流擾動的變化週期，本研究提出了不同於 Chen and Houze（1997）與 Yamada et al.（2010）的詮釋。首先，可能伴隨 2011 年十月 MJO 對流系統肇始，單日變化對流波動在赤道印度洋東經 80 度至 85 度區域出現，並以每秒 10–15 公尺的速度向西傳遞，約莫在一天以後通過 DYNAMO 實驗區域。分析結果指出，每天向西傳遞的對流波動在通過 Gan Island 區域時，每兩天僅會被激發一次、形成緯向空間尺度約為 500–1000 公里的組織性對流系統，因此在 Gan Island 出現準雙日的對流發生週期。而單日變化對流波動每兩天僅被激發一次的原因，很有可能是受到前一天組織性對流系統影響。由於前一天對流系統後期低對流層的中尺度沈降，區域內底層大氣及邊界層趨於穩定，使得邊界層恢復到能夠激發對流擾動的時間延長，影響了下一次單日變化對流波動的激發（圖 6.3、6.5、6.8、6.11）。除了中尺度的沉降會使邊界層穩定之外，向西移行的層狀雲系所造成的層狀降水及大範圍雲覆蓋（圖 6.6），也會調整 Gan Island 區域附近的低層大氣及邊界層，延長邊界層的恢復時間。即便層狀雲系持續受高層東風影響向西移行，MJO1 期間 Gan Island 區域附近的低對流層西風仍會將穩定的空氣向東平流至 Gan Island，有助於該區域內穩定邊界層的維持，直到單日變化對流波動再次被激發。

　　因此，根據 DYNAMO 觀測結果，本研究的詮釋仍承襲 Chen and Houze（1997）機制當中關於邊界層恢復時間延長的概念。然而，由於赤道中印度洋與赤道西太平洋不同的風切環境及不同的 MJO 傳遞速度，本研究部分沿用 Yamada et al.（2010）所提出的概念模型，提出不同於 Chen and Houze（1997）的詮釋，解釋發生在赤道中印度洋 MJO1 期間的準雙日週期對流擾動。

51

APPENDIX D Chapter 8 Summary and Concluding Remarks (Chinese Version)

重要結論與研究總結

　　本研究分析 2011 年十月 15 至 31 日、赤道中印度洋 Madden-Julian Oscillation（MJO）對流活躍期間，DYNAMO/AMIE/CINDY 2011（DYNAMO）實驗所觀測到之發生週期約莫為兩天的西行對流擾動（準雙日對流擾動）。

　　運用 DYNAMO 實驗期間的探空觀測、衛星、雷達資料及其衍生產品，本研究針對在中印度洋 Gan Island 測站所觀測到的七組準雙日對流擾動個案，進行包含合成分析與波譜分析等客觀分析。重要分析結果條列如下：

　　一、

　　衛星紅外線亮度溫度（IRBT）與 TRMM 衛星降雨資料顯示，Gan Island 測站定點觀測到的七組準雙日對流擾動個案，實際上為 2011 年十月 MJO 對流活躍期間（MJO1）西行通過中印度洋的對流系統造成。該對流系統以大約兩天的週期出現、並以每秒 10–12 公尺的速度向西傳遞。該傳遞速度與過去 1992–1993 年在赤道西太平洋 TOGA COARE 觀測實驗所發現到的準雙日對流擾動傳遞速度尺度一致（每秒 10–19 公尺；Haertel and Johnson 1998；Takayabu 1994b）；但 DYNAMO MJO1 期間擾動向西移行 1000－1500 公里的緯向空間尺度卻小於 TOGA COARE 實驗觀測到的 2000–4000 公里（Chen et al. 1996；Chen and Houze 1997；Clayson et al. 2002）。

　　二、

　　波譜分析中，我們利用 Lanczos 濾波方式分離單日週期（0.9–1.2 天）訊號與準雙日週期（1.6–3 天）訊號，結果顯示此七組準雙日對流擾動個案包含兩種主要的對流型態。第一種為以每秒 10–12 公尺速度向西傳遞的單日變化對流波動。分析結果顯示該波動極有可能與相當厚度為 20 公尺、n=1 的西行慣性重力波（inertial gravity waves; IGWs）有關（Takayabu 1994a,b；Takayabu et al 1996；Wheeler and Kiladis 1999；Haertel and Kiladis 2004）。第二種為緯向空間尺度約 1000 公里、在 Gan Island 附近區域發展的準雙日對流擾動。在 MJO1 期間，該擾動為控制中印度

洋、特別是 Gan Island 附近降水強度及對流發展空間尺度的主要因子，並解釋超過一半的亮度溫度訊號變異（54.7%）。顯示區域性的準雙日對流擾動，有效地將西行至 Gan Island 附近的單日變化對流波動調整為準雙日的發生週期。

三、

衛星資料分析顯示，MJO1 期間準雙日週期與單日週期的對流擾動在印度洋具有不同的分布特徵。準雙日對流擾動主要分布在北緯 10 度至南緯 10 度的赤道洋面，雷同於 TOGA COARE 的觀測（Haertel and Johnson 1998）。單日週期的對流擾動則與印度洋周遭的地形緊密關聯，主要分布在蘇門答臘島、印度南端、以及斯里蘭卡，顯示單日週期的對流擾動主要是受地形所激發。而在中印度洋開放洋面上，準雙日週期對流擾動的強度與空間尺度遠大於單日週期的對流擾動。

四、

合成分析當中，我們以 MJO1 期間 Gan Island 附近 150 公里區域內、平均亮度溫度出現相對低值的時間為基準（0 h），進行七組準雙日對流擾動個案的 48 小時合成，檢視對流擾動內的垂直大氣特徵。結果顯示準雙日對流擾動的生命期具有典型中尺度對流系統（MCSs）的變化特徵：即 "淺對流－深對流－層狀雲" 的變化。因此，準雙日對流擾動的生命期可區分為下述四個階段：

1、對流抑制期（convective suppressed stage；–1 d 至–9 h）：水氣主要集中在邊界層及低對流層。低對流層受淺積雲主導。

2、對流發展期（convective intensifying stage；–9 h 至 0 h）：當中較淺的對流雲逐漸發展為深對流雲，除了造成 Gan Island 附近區域內的降水強度增加，也主導區域內的大氣垂直結構。

3、對流成熟期（mature stage；0 h 至+6 h）：深對流雲發展旺盛、雲砧開始出現。成熟階段後期深對流雲逐漸轉化為層狀雲。

4、層狀雲期（stratiform stage；+6 h 至+18 h）：Gan Island 區域內大部分的對流雲都消散、轉化為層狀雲及層狀降水主導的大氣結構。

準雙日對流擾動的生命期除了與中尺度對流系統類似，也與較大尺度的對流活動、如季內震盪（ISOs）的生命期變化類似（Kiladis et al. 2009）。

五、

合成分析同時檢驗準雙日對流擾動當中的輻射效應、Q_1（apparent heat

sources）、Q_2（apparent moisture sinks）及其他大氣狀態變數的垂直結構：如相當位溫及溫度遞減率。結果顯示，對流發展過程中深對流雲內的輻射加熱，可能會驅使成熟階段後期對流雲轉化為層狀雲的過程。Q_1 及 Q_2 的垂直結構變化也與對流雲轉化為層狀雲的過程一致。在層狀雲階段，受中尺度對流過程影響而出現在邊界層內、長達十幾小時的低相當位溫分布，也顯示準雙日週期的出現，可能是受到中尺度對流過程的影響，其機制類似於 Chen and Houze （1997）根據 TOGA COARE 實驗所提出的觀點。

綜整以上分析結果、並根據過去在西太平洋與印度洋的觀測，本研究提出一項概念模型，詮釋 DYNAMO 實驗期間所觀測到的準雙日對流擾動（如圖 7.5 所示）。根據示意圖，準雙日對流擾動的生命期類似 Takayabu 等利用西太平洋 TOGA COARE 觀測的結果：具有 "淺對流－深對流－層狀雲" 的變化（Takayabu et al. 1996、圖 19；如圖 1.3 所示）。DYNAMO 及 TOGA COARE 兩項觀測實驗皆顯示，準雙日對流擾動的生命期當中具有較長的層狀雲階段，類似長生命期的中尺度對流系統或颮線系統。而在 DYNAMO 實驗期間的七組個案中，NCAR S-Pol 雷達資料也顯示部分個案存在長生命期的颮線（圖 7.2 至 7.4）。

根據衛星觀測以及過去 Nakazawa （1988）所提出的想法，發生在赤道中印度洋 MJO1 期間的準雙日週期對流擾動，最初是受到 MJO 對流活躍期間向西移行的單日變化對流波動（慣性重力波）主導；該對流波動在中印度洋、特別是 Gan Island 區域附近，受中尺度對流過程影響而被調整為準雙日週期的對流擾動。因此，準雙日對流擾動的出現可被視為向西傳遞的重力波與區域性準雙日週期對流活動的合成結果。此外，雷達分析也顯示在觀測到的七組個案當中，部分存在受風切環境影響而交互移行的對流雲系統：包含受底層西風影響而向東移行的對流雲、以及受高層東風影響而向西傳遞的層狀雲等高層雲系。該結果類似 2006 年印度洋 MISMO 實驗的發現，以及 Yamada et al. （2010）針對印度洋準雙日對流擾動提出的可能機制。

根據合成分析，調整西行單日變化對流波動的區域性準雙日對流擾動，乃肇因於較長時間的中尺度對流發展過程以及較長時間的邊界層恢復，類似 Chen and Houze （1997）提出的 "diurnal dancing" 機制。然而，與 Chen and Houze 的 TOGA COARE 觀測結果不同，在 DYNAMO 期間，向東移行的 MJO 對流訊號（MJO1）

54

在中印度洋的移行速度相對緩慢，使得向西移行的小尺度單日變化對流波動在中印度洋區域被有效地調整為準雙日週期。因此，不同於 Chen and Houze 的解釋，本研究在詮釋上（如第 7 章所述），將 MJO1 期間發生的準雙日對流擾動視為**向西傳遞的單日週期對流波動（重力波）、與區域性準雙日週期中尺度對流活動交互作用下的結果。**
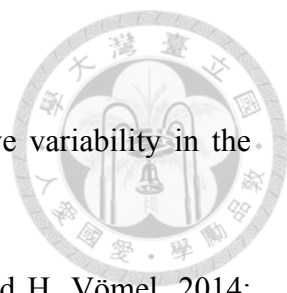
　　然而，在本研究的詮釋所涵蓋範圍之外，準雙日對流擾動仍有許多層面的問題仍待解決。為何準雙日對流擾動出現在某些 MJO 對流活躍時期，如 2011 年十月份的 MJO；而在某些 MJO 當中則未被發現（如 2011 年十一月及十二月）？此外，什麼樣的環境條件會維持準雙日對流擾動的出現？而什麼樣的條件決定其移行的水平空間尺度？再者，準雙日對流擾動在 MJO 肇始期間，對於濕化對流層與動量傳輸上又扮演什麼樣的角色？
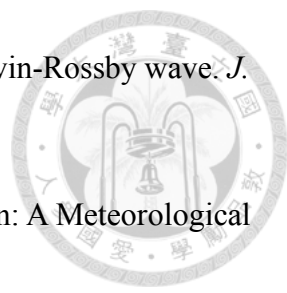
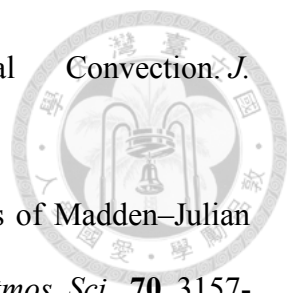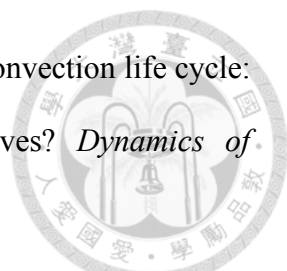　　後續針對 DYNAMO 雷達資料的詳盡分析以及雲解析數值模擬，或能回答以上問題，並進一步幫助我們瞭解赤道洋面上的準雙日對流擾動現象。

REFERENCE

Albrecht, B. A., A. K. Betts, W. H. Schubert, and S. K. Cox, 1979: A model for the thermodynamic structure of the trade-wind boundary layer. *J. Atmos. Sci.*, **36**, 73-89.

Chen, S. S., and R. A. Houze, 1997: Diurnal variation and life-cycle of deep convective systems over the tropical Pacific warm pool. *Quart. Journal of the Roy. Meteor. Society*, **123,** 357-388.

Chen, S.S., R.A. Houze, and B.E. Mapes, 1996: Multiscale Variability of Deep Convection in Relation to Large-Scale Circulation in TOGA COARE. *J. Atmos. Sci.,* **53**,1380–1409.

Ciesielski, P.E., P.T. Haertel, R.H. Johnson, J. Wang, and S.M. Loehrer, 2012: Developing High-Quality Field Program Sounding Datasets. *Bull. Amer. Meteor. Soc.,* **93**,325–336.

Ciesielski, P.E., H. Yu, R.H. Johnson, K. Yoneyama, M. Katsumata, C.N. Long, J. Wang, S.M. Loehrer, K. Young, S.F. Williams, W. Brown, J. Braun, and T. Van Hove, 2014: Quality-Controlled Upper-Air Sounding Dataset for DYNAMO/CINDY/AMIE: Development and Corrections. *J. Atmos. Oceanic Technol.,* **31**, 741–764.

Ciesielski, P., R. Johnson, X. Jiang, Y. Zhang, and S. Xie, 2017: Relationships between radiation, clouds, and convection during DYNAMO. *J. Geophys. Res.: Atmospheres*, **122**, 2529–2548.

Cifelli, R. and S.A. Rutledge, 1994: Vertical Motion Structure in Maritime continent mesoscale Convective Systems: Results from a 50-MHz Profiler. *J. Atmos.*

Sci., **51**,2631–2652.

Clayson, C.A., B. Strahl, and J. Schrage, 2002: 2–3-Day convective variability in the tropical western Pacific. *Mon. Wea. Rev.,* **130**, 529–548.

Dirksen, R. J., M. Sommer, F. J. Immler, D. F. Hurst, R. Kivi, and H. Vömel, 2014: Reference quality upper-air measurements: GRUAN data processing for the Vaisala RS92 radiosonde. *Atmos. Meas. Tech. Discuss.,* **7**, 3727–3800.

Duchon, C.E., 1979: Lanczos filtering in one and two dimensions. *J. Appl. Meteor.,* **18**, 1016–1022.

Feng, Z., S. A. McFarlane, C. Schumacher, S. Ellis, J. Comstock, and N. Bharadwaj, 2014: Constructing a merged cloud–precipitation radar dataset for tropical convective clouds during the DYNAMO/AMIE experiment at Addu Atoll. *J. Atmos. Oceanic Technol.*, **31,** 1021-1042.

Fu, Q. and K.N. Liou, 1992: On the correlated k-distribution method for radiative transfer in nonhomogeneous atmospheres. *J. Atmos. Sci.,* **49**, 2139–2156.

Gallus, W.A. and R.H. Johnson, 1991: Heat and moisture budgets of an intense midlatitude squall line. *J. Atmos. Sci.,* **48**, 122–146.

Gray, W.M. and R.W. Jacobson, 1977: Diurnal variation of deep cumulus convection. *Mon. Wea. Rev.,* **105**, 1171–1188.

Haertel, P. T., and R. H. Johnson, 1998: Two-day disturbances in the equatorial western Pacific. *Quart. Journal of the Roy. Meteor. Society*, **124,** 615-636.

Haertel, P.T., and G.N. Kiladis, 2004: Dynamics of 2-Day equatorial waves. *J. Atmos. Sci.,* **61**, 2707–2721.

Hendon, H. H., and B. Liebmann, 1994: Organization of convection within the Madden-Julian oscillation. *J. Geophys. Res.: Atmospheres*, **99,** 8073-8083.

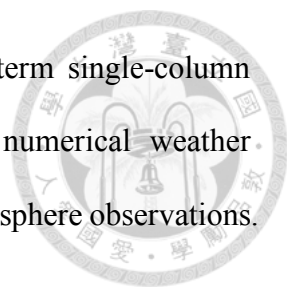Houze, R. A., S. S. Chen, D. E. Kingsmill, Y. Serra, and S. E. Yuter, 2000: Convection

over the Pacific warm pool in relation to the atmospheric Kelvin-Rossby wave. *J. Atmos. Sci.*, **57,** 3058-3089.

Houze, R.A., 1997: Stratiform Precipitation in Regions of Convection: A Meteorological Paradox? *Bull. Amer. Meteor. Soc.,* **78**, 2179–2196.

Houze, R. A., 1989: Observed structure of mesoscale convective systems and implications for large-scale heating. *Quart. Journal of the Roy. Meteor. Society,* **115,** 425-461.

Immler, F. J., J. Dykema, T. Gardiner, D. N. Whiteman, P. W. Thorne, and H. Vömel, 2010: A guide for upper-air reference measurements: Guidance for developing GRUAN data products. *Atmos. Meas. Tech.*, **3**, 1217–1231.

Immler, F. J., and M. Sommer, 2011: Brief description of the RS92 GRUAN data product (RS92-GDP). Revision 1.1, GRUAN Tech. Doc. GRUAN-TD-4, 17 pp. (Available online at http://www.dwd.de/bvbw/generator/DWDWWW/Content/Projekte/Gruan/Downloads/documents/gruan-td-4,templateId5raw,property5publicationFile.pdf/gruan-td-4.pdf).

Johnson, R.H., 1984: Partitioning Tropical Heat and Moisture Budgets into Cumulus and Mesoscale Components: Implications for Cumulus Parameterization. *Mon. Wea. Rev.,* **112**, 1590–1601.

Johnson, R.H., W.A. Gallus, and M.D. Vescio, 1990: Near-Tropopause Vertical Motion within the Trailing Stratiform Region of a Midlatitude Squall Line. *J. Atmos. Sci.,* **47**,2200–2210.

Johnson, R.H., P.E. Ciesielski, and K.A. Hart, 1996: Tropical Inversions near the 0°C Level. *J. Atmos. Sci.,* **53**, 1838–1855.

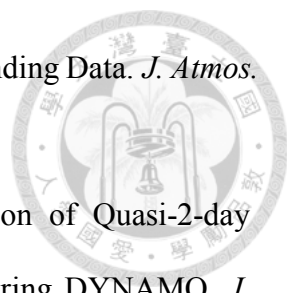Johnson, R.H., T.M. Rickenbach, S.A. Rutledge, P.E. Ciesielski, and W.H.

Schubert, 1999: Trimodal Characteristics of Tropical Convection. *J. Climate,* **12**, 2397–2418.

Johnson, R. H., and P. E. Ciesielski, 2013: Structure and Properties of Madden–Julian Oscillations Deduced from DYNAMO Sounding Arrays. *J. Atmos. Sci.*, **70,** 3157-3179.

Johnson, R. H., P. E. Ciesielski, J. H. Ruppert, and M. Katsumata, 2015: Sounding-Based Thermodynamic Budgets for DYNAMO. *J. Atmos. Sci.*, **72,** 598-622.

Johnson, R. H., and P. E. Ciesielski, 2017: Multiscale Variability of the Atmospheric Boundary Layer during DYNAMO. *J. Atmos. Sci.*, **74,** 4003-4021.

Kikuchi, K., and Y. N. Takayabu, 2004: The development of organized convection associated with the MJO during TOGA COARE IOP: Trimodal characteristics. *Geophysical Research Letters*, **31,** L10101.

Kiladis, G. N., M. C. Wheeler, P. T. Haertel, K. H. Straub, and P. E. Roundy, 2009: Convectively coupled equatorial waves. *Reviews of Geophysics*, **47***, RG2003*.

Kubota, H., K. Yoneyama, J.-I. Hamada, P. Wu, A. Sudaryanto, and I. B. Wahyono, 2015: Role of Maritime Continent Convection during the Preconditioning Stage of the Madden-Julian Oscillation Observed in CINDY2011/DYNAMO. *Journal of the Meteor. Society of Japan. Ser. II*, **93A,** 101-114.

Lau, K., T. Nakazawa, and C. Sui, 1991: Observations of cloud cluster hierarchies over the tropical western Pacific. *J. Geophys. Res.: Oceans*, **96,** 3197-3208.

Liu, F. and B. Wang, 2012: A model for the interaction between 2-day waves and moist Kelvin waves. *J. Atmos. Sci.*, **69**, 611–625.

Loehrer, S.M., T.A. Edmands, and J.A. Moore, 1996: TOGA COARE Upper-Air Sounding Data Archive: Development and Quality Control Procedures. *Bull. Amer. Meteor. Soc.,* **77**, 2651–2672.

59

Mapes, B., S. Tulich, J. Lin, and P. Zuidema, 2006: The mesoscale convection life cycle: Building block or prototype for large-scale tropical waves? *Dynamics of Atmospheres and Oceans*, **42,** 3-29.

Mather, J. H., McFarlane, S. A., Miller, M. A., and Johnson, K. L., 2007: Cloud properties and associated radiative heating rates in the tropical western Pacific. *J. Geophys. Res.: Atmospheres*, **112**, D05201.

Nakazawa, T., 1988: Tropical super clusters within intraseasonal variations over the western Pacific. *Journal of the Meteor. Society of Japan. Ser. II*, **66,** 823-839.

Nakazawa, T., 1995: Intraseasonal oscillations during the TOGA-COARE IOP. *Journal of the Meteor. Society of Japan. Ser. II*, **73,** 305-319.

Nuss, W. A., and D. W. Titley, 1994: Use of multiquadric interpolation for meteorological objective analysis. *Mon. Wea. Rev.*, **122,** 1611-1631.

Randall, D.A., Harshvardhan, and D.A. Dazlich, 1991: Diurnal Variability of the Hydrologic Cycle in a General Circulation Model. *J. Atmos. Sci.,* **48**, 40–62.

Saji, N., B. Goswami, P. Vinayachandran, and T. Yamagata, 1999: A dipole mode in the tropical Indian Ocean. *Nature*, **401,** 360.

Sarachik, E. S., 1985: A simple theory for the vertical structure of the tropical atmosphere. *Pure Appl. Geophys.,* **123**, 261-271.

Schubert, W.H., P.E. Ciesielski, C. Lu, and R.H. Johnson, 1995: Dynamical Adjustment of the Trade Wind Inversion Layer. *J. Atmos. Sci.,* **52**, 2941–2952.

Takayabu, Y. N., 1994a: Large-scale cloud disturbances associated with equatorial waves. Part I: Spectral features of the cloud disturbances. *Journal of the Meteor. Society of Japan. Ser. II*, **72,** 433-449.

Takayabu, Y. N., 1994b: Large-scale cloud disturbances associated with equatorial waves. Part II: Westward-propagating inertia-gravity waves. *Journal of the Meteor.*
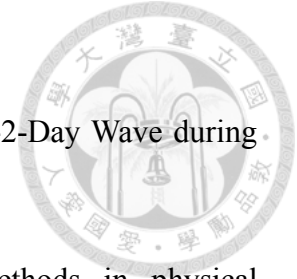
Society of Japan. Ser. II, **72,** 451-465.

Takayabu, Y.N., K. Lau, and C. Sui, 1996: Observation of a Quasi-2-Day Wave during TOGA COARE. *Mon. Wea. Rev.,* **124**, 1892–1913.

Thomson, R. E., and W. J. Emery, 2014: Data analysis methods in physical oceanography. *Newnes*.

Tropical Rainfall Measuring Mission (TRMM), 2011: TRMM (TMPA) Rainfall Estimate L3 3 hour 0.25° by 0.25° V7. Greenbelt, MD, Goddard Earth Sciences Data and Information Services Center (GES DISC), accessed 16 Sep 2014. https://disc.gsfc.nasa.gov/datacollection/TRMM_3B42_7.html

UCAR/NCAR - Earth Observing Laboratory, 2012: Meteosat-7 IR (Channel 8) Calibrated Data in NetCDF Format, version 1.0. UCAR/NCAR - Earth Observing Laboratory, accessed 22 October 2014. http://data.eol.ucar.edu/dataset/347.027

Uyeda, H., and coauthors, 1995: Doppler Radar Observations on the Structure and Characteristics of Tropical Clouds during the TOGA-COARE IOP in Manus, Papua New Guinea. *Journal of the Meteor. Society of Japan. Ser. II*, **73,** 415-426.

Webster, P.J. and R. Lukas, 1992: TOGA COARE: The Coupled Ocean-Atmosphere Response Experiment. *Bull. Amer. Meteor. Soc.,* **73**, 1377–1416.

Webster, P.J. and G.L. Stephens, 1980: Tropical Upper-Tropospheric Extended Clouds: Inferences from Winter MONEX. *J. Atmos. Sci.,* **37**, 1521–1541.

Wheeler, M. and G.N. Kiladis, 1999: Convectively Coupled Equatorial Waves: Analysis of Clouds and Temperature in the Wavenumber–Frequency Domain. *J. Atmos. Sci.,* **56**, 374–399.

Wheeler, M., G.N. Kiladis, and P.J. Webster, 2000: Large-Scale Dynamical Fields Associated with Convectively Coupled Equatorial Waves. *J. Atmos. Sci.,* **57**, 613–640.

61

Xie, S., R. T. Cederwall, and M. Zhang, 2004: Developing long-term single-column model/cloud system–resolving model forcing data using numerical weather prediction products constrained by surface and top of the atmosphere observations. *J. Geophys. Res.: Atmospheres*, **109**.

Xu, W., and S. A. Rutledge, 2014: Convective characteristics of the Madden–Julian oscillation over the central Indian Ocean observed by shipborne radar during DYNAMO. *J. Atmos. Sci.*, **71**, 2859-2877.

Yamada, H., K. Yoneyama, M. Katsumata, and R. Shirooka, 2010: Observations of a Super Cloud Cluster Accompanied by Synoptic-Scale Eastward-Propagating Precipitating Systems over the Indian Ocean. *J. Atmos. Sci.,* **67**, 1456–1473.

Yanai, M., S. Esbensen, and J. Chu, 1973: Determination of Bulk Properties of Tropical Cloud Clusters from Large-Scale Heat and Moisture Budgets. *J. Atmos. Sci.,* **30**,611–627.

Yanase, A., K. Yasunaga, and H. Masunaga, 2017: Relationship between the direction of diurnal rainfall migration and the ambient wind over the Southern Sumatra Island. *Earth and Space Science*, **4,** 117-127.

Yoneyama, K., M. Katsumata, K. Mizuno, M. Yoshizaki, R. Shirooka, K. Yasunaga, H. Yamada, N. Sato, T. Ushiyama, Q. Moteki, A. Seiki, M. Fujita, K. Ando, H. Hase, I. Ueki, T. Horii, Y. Masumoto, Y. Kuroda, Y.N. Takayabu, A. Shareef, Y. Fujiyoshi, M.J. McPhaden, V.S. Murty, C. Yokoyama, and T. Miyakawa, 2008: Mismo Field Experiment in the Equatorial Indian Ocean. *Bull. Amer. Meteor. Soc.,* **89**, 1889–1903.

Yoneyama, K., C. Zhang, and C.N. Long, 2013: Tracking Pulses of the Madden–Julian Oscillation. *Bull. Amer. Meteor. Soc.,* **94**, 1871–1891.

Yu, H., P.E. Ciesielski, J. Wang, H. Kuo, H. Vömel, and R. Dirksen, 2015: Evaluation of

Humidity Correction Methods for Vaisala RS92 Tropical Sounding Data. *J. Atmos. Oceanic Technol., 32*, 397–411.

Yu, H., R. Johnson, P. Ciesielski, and H. Kuo, 2018: Observation of Quasi-2-day Convective Disturbances in the Equatorial Indian Ocean during DYNAMO. *J. Atmos. Sci.*, doi:10.1175/JAS-D-17-0351.1, in press.

Zhang, C., and K. Yoneyama, 2017: CINDY/DYNAMO Field Campaign: Advancing Our Understanding of MJO Initiation. *The Global Monsoon System: Research and Forecast*, **9,** 339.

Zhang, M.H. and J.L. Lin, 1997: Constrained Variational Analysis of Sounding Data Based on Column-Integrated Budgets of Mass, Heat, Moisture, and Momentum: Approach and Application to ARM Measurements. *J. Atmos. Sci.,* **54**, 1503–1524.

Zhang, M.H., J.L. Lin, R.T. Cederwall, J.J. Yio, and S.C. Xie, 2001: Objective Analysis of ARM IOP Data: Method and Sensitivity. *Mon. Wea. Rev.,* **129**, 295–311.

Zipser, E.J., 1977: Mesoscale and Convective–Scale Downdrafts as Distinct Components of Squall-Line Structure. *Mon. Wea. Rev.,* **105**, 1568–1589.

Zuluaga, M.D. and R.A. Houze, 2013: Evolution of the Population of Precipitating Convective Systems over the Equatorial Indian Ocean in Active Phases of the Madden–Julian Oscillation. *J. Atmos. Sci.,* **70**, 2713–2725.

TABLES
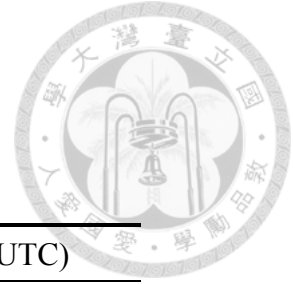
	Date	Time (UTC)
Event 1	16 Oct. 2011	1200
Event 2	18 Oct. 2011	2100
Event 3	20 Oct. 2011	2100
Event 4	22 Oct. 2011	0300
Event 5	24 Oct. 2011	0600
Event 6	26 Oct. 2011	0600
Event 7	28 Oct. 2011	1200
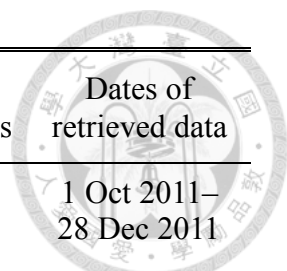
Table 3.1. Date and time of the minimum peaks of 6-hourly averaged IRBT over 150-km radius circular region around Gan. The seven most convectively active events with quasi-2-day intervals of occurrence were selected during 15–31 October 2011 in DYNAMO. LT = UTC + 5.

Date	Time (UTC)
16 Oct. 2011	0800
18 Oct. 2011	1800
20 Oct. 2011	2000
22 Oct. 2011	0100
24 Oct. 2011	0300
26 Oct. 2011	0200
18 Nov. 2011	0300
23 Nov. 2011	0700
27 Nov. 2011	0200
20 Dec. 2011	2100
23 Dec. 2011	2000
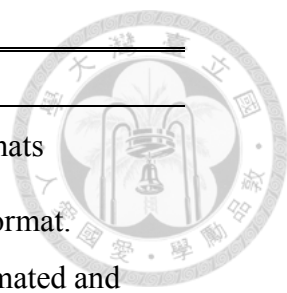
Table 3.2. Date and time of the selected maxima in rain accumulation based on hourly S-Pol rain accumulation for the 11 rainiest events during the October 2011–January 2012 period of the DYNAMO campaign. (Table 3 in Zuluaga and Houze 2013)

Site	Station ID	Radiosonde type	Native resolution (s)	No. of soundings	Dates of retrieved data
Colombo	43466	Meisei RS06G	1	258	1 Oct 2011–28 Dec 2011
Diego Garcia	DRG	Vaisala RS92-SGP	1	679	30 Sep 2011–15 Jan 2012
Gan	43599	Vaisala RS92-SGP	2	1250	15 Jun 2011–8 Apr 2012
Malé	43555	Vaisala RS92-SGP	2	323	29 Sep 2011–15 Dec 2011
R/V *Mirai*	JNSR	Vaisala RS92-SGP	2	518	26 Sep 2011–10 Dec 2011
R/V *Revelle*	KAOU	Vaisala RS92-SGP	1	635	30 Aug 2011–10 Feb 2012

Table A.1.   DYNAMO site information for the six core stations. Native resolution refers to the vertical time resolution of the data received at NCAR EOL. (Table 2 in Ciesielski et al. 2014)

Level	Description
Level 0 (L0)	Raw, unprocessed hi-res data in original formats
Level 1 (L1)	Initial hi-res data: uniform, easily readable format.
Level 2 (L2)	Preliminary hi-res data: processed with automated and visual QC.
Level 3 (L3)	Final hi-res data: corrected for biases and errors if necessary.
Level 4 (L4)	Uniform vertical resolution data created from hi-res datasets and GTS resolution soundings processed with objective QC checks and visual inspection.

Table A.2.　　Post-processing stages for DYNAMO radiosonde dataset with a brief description of the dataset at each level. (Table 5 in Ciesielski et al. 2014)

FIGURES
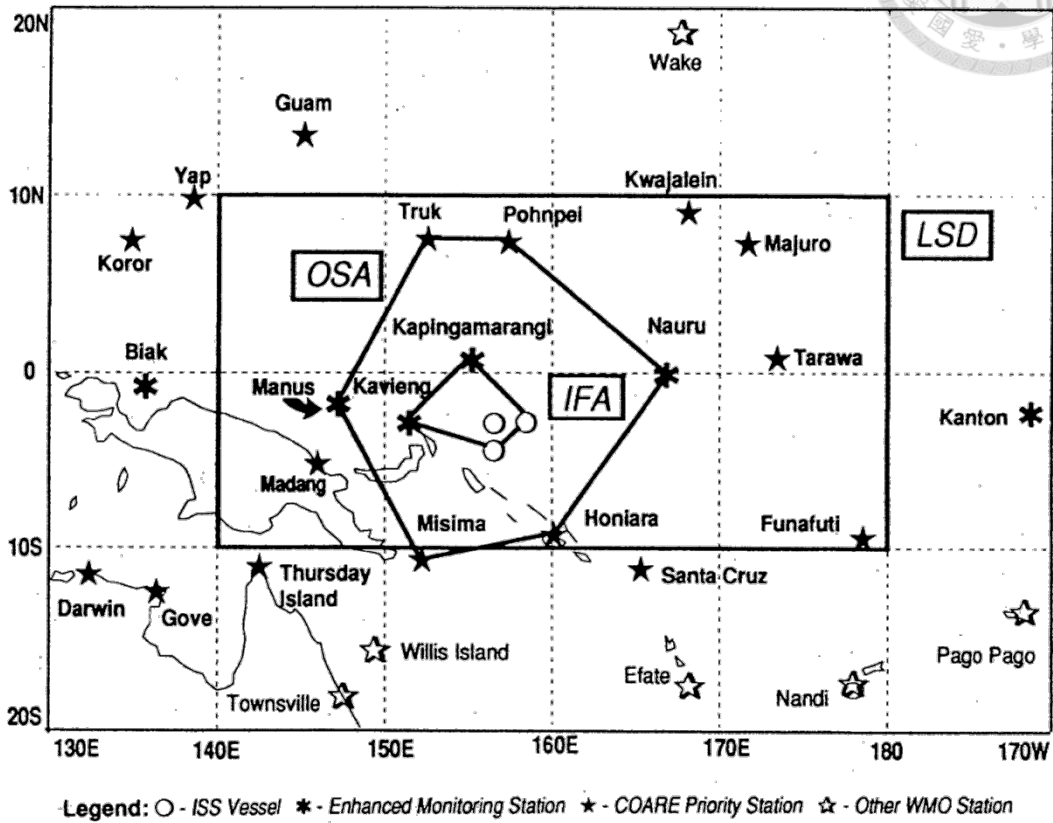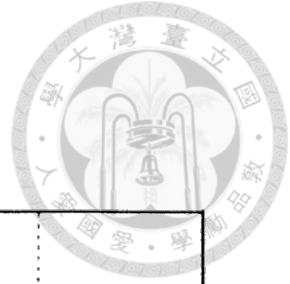
Figure 1.1.   The entire TOGA COARE domain during the IOP. The legends beneath the panels refer to the symbols used to represent the observational platforms. The large-scale domain (LSD), the outer sounding array (OSA) and the intensive flux array (IFA) are outlined. (Figure 14 in Webster and Lukas 1992)
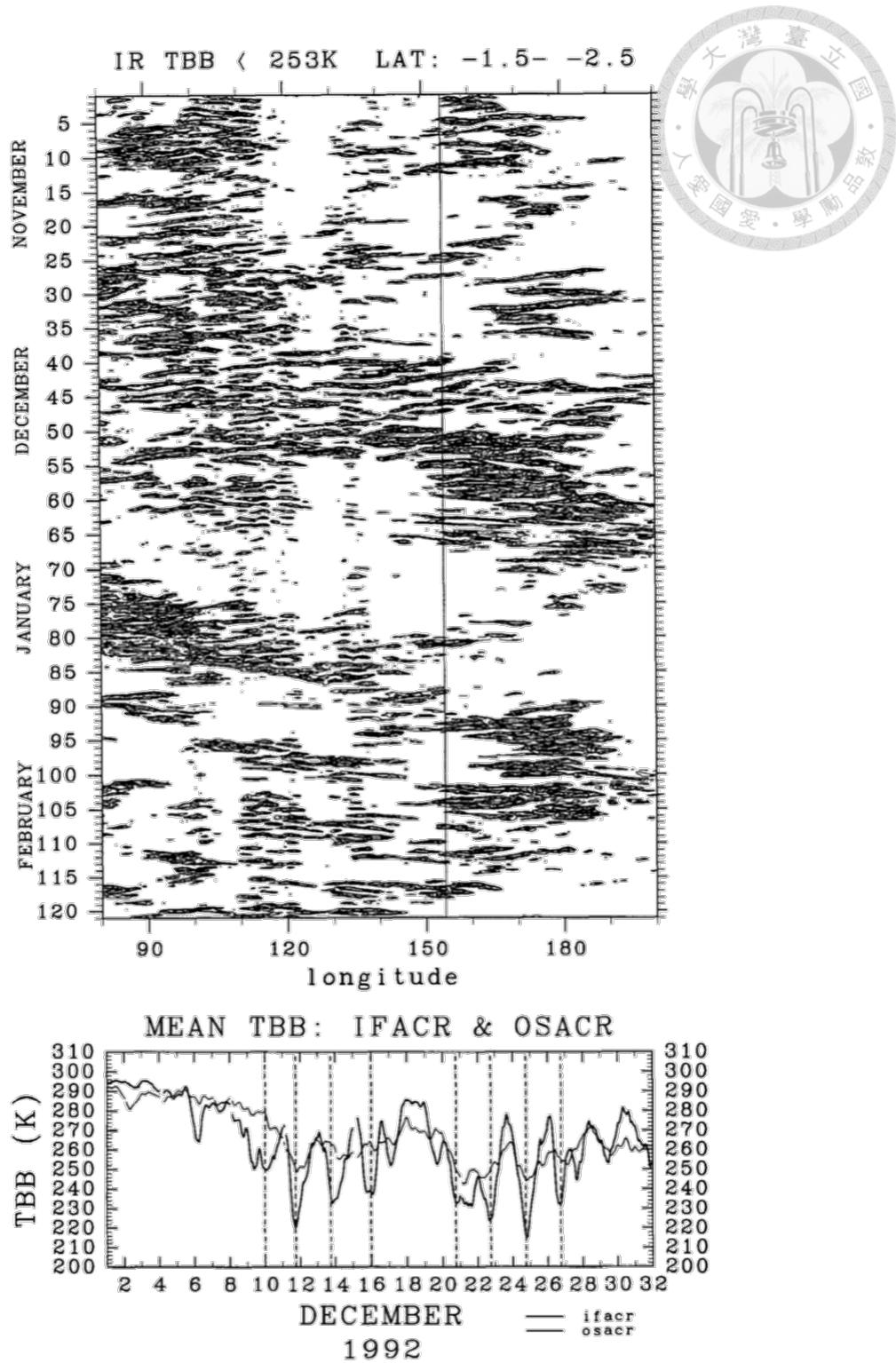
Figure 1.2.　(top) Time-longitude diagram of 3-hourly infrared brightness temperature

from Japanese Geostationary Meteorological Satellite (GMS) along 1.5-2.5°S for TOGA

COARE period, (Figure 2 in Takayabu et al. 1996) and (bottom) time variations of the

69

averaged brightness temperature over IFA (thicker line) and OSA (thinner line) for December 1992. The vertical dashed lines indicate the 8 quasi-2-day events examined. (Figure 4 in Takayabu et al. 1996)

70
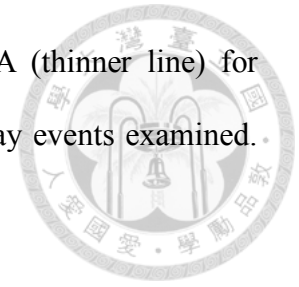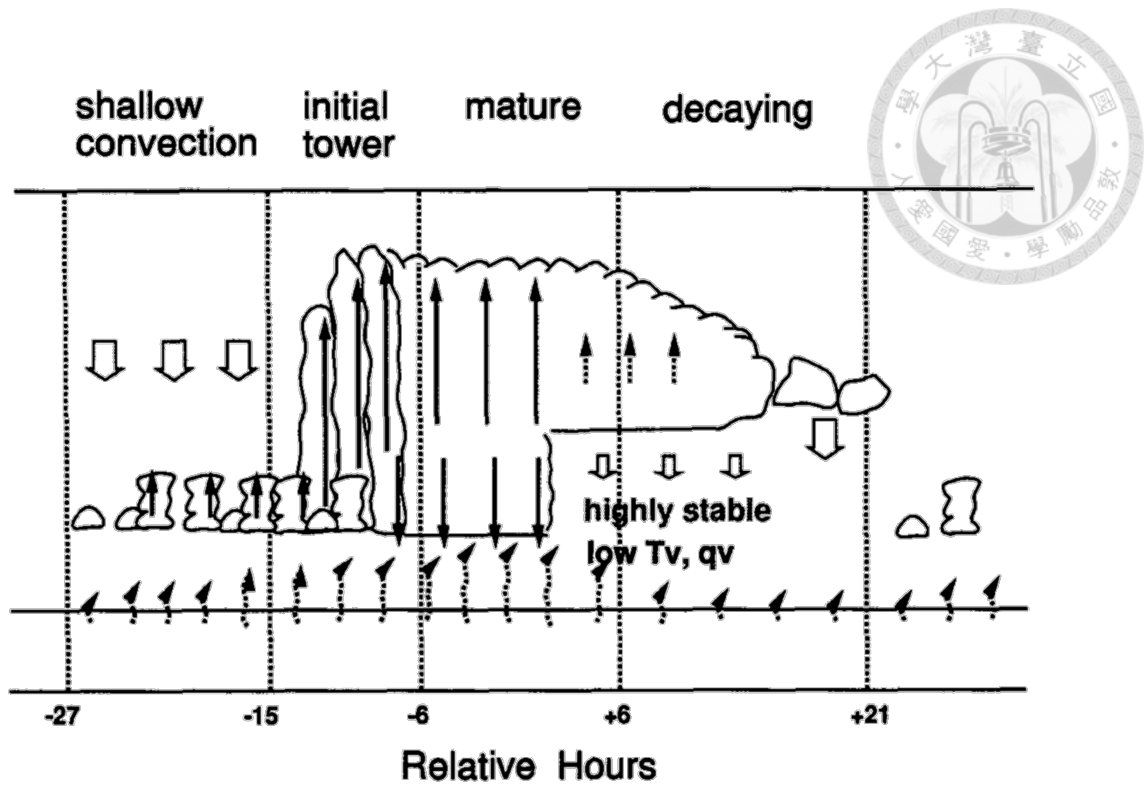
Figure 1.3.   Schematics for the quasi-2-day variation in TOGA COARE. Straight arrows indicate the vertical air motion and wavy arrows indicate the surface heat flux. (Figure 19 in Takayabu et al. 1996)
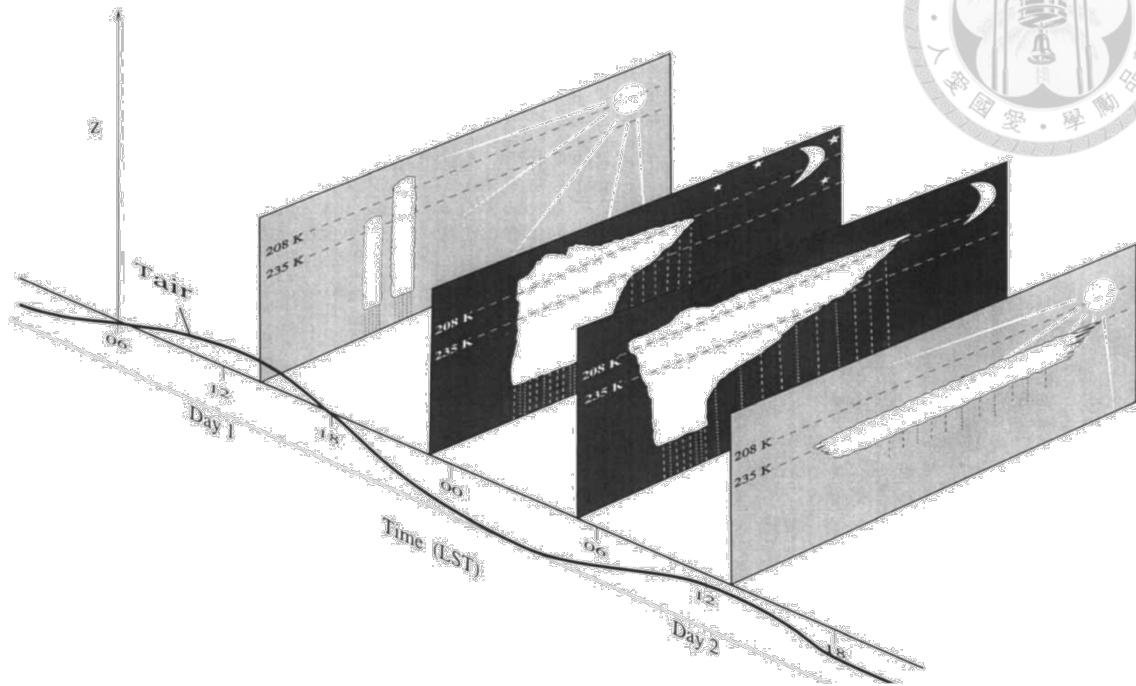
Figure 1.4. Schematic of the 2-day cycle of surface-cloud-radiation interaction for large convective systems. T_{air} is the surface air temperature. (Figure 18 in Chen and Houze 1997)
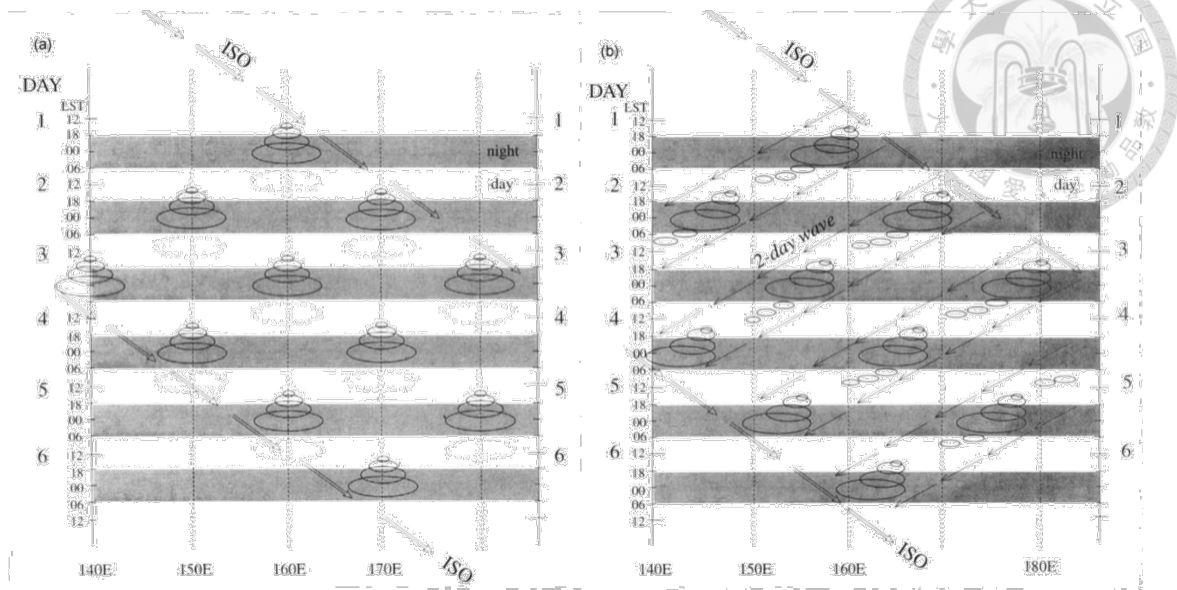
Figure 1.5.   Schematics of the time-longitude variation of cold cloud tops of large convective systems during the active phase of the ISO. (a) Spatial variation of the large convective systems within the envelope of the ISO caused by the diurnal behavior of these large systems alone (solid circles <208 K, dashed circles ~235–260 K). The smallest circle represents the early stage of the system (first afternoon cross-section in Figure 1.4), the largest circle represents the mature stage with the maximum areal extent of cold cloud tops (pre-dawn cross-section in Figure 1.4), and the dashed circles represent the warmer cloud deck (last cross-section in Figure 1.4). (b) The westward-propagating speed of 2-day equatorial inertial gravity waves is added to the westward displacement of the starting location of a new convective system. The pattern in (b) is the sum of the effects of the ISO, 2-day waves and the diurnal cycle of large convective systems. (Figure 19 in Chen and Houze 1997)

73

Figure 1.6.   Time-longitude diagram of deep convection with cloud-top temperature <208 K for December 1992. The contours are the number of pixels colder than 208 K in a 10° latitude band along each longitude grid. The arrows are 850-hPa total wind (m/s) averaged over the 10° latitude band. The position of the IFA is indicated at the top of the figure. (Figure 9b in Chen et al. 1996)

74
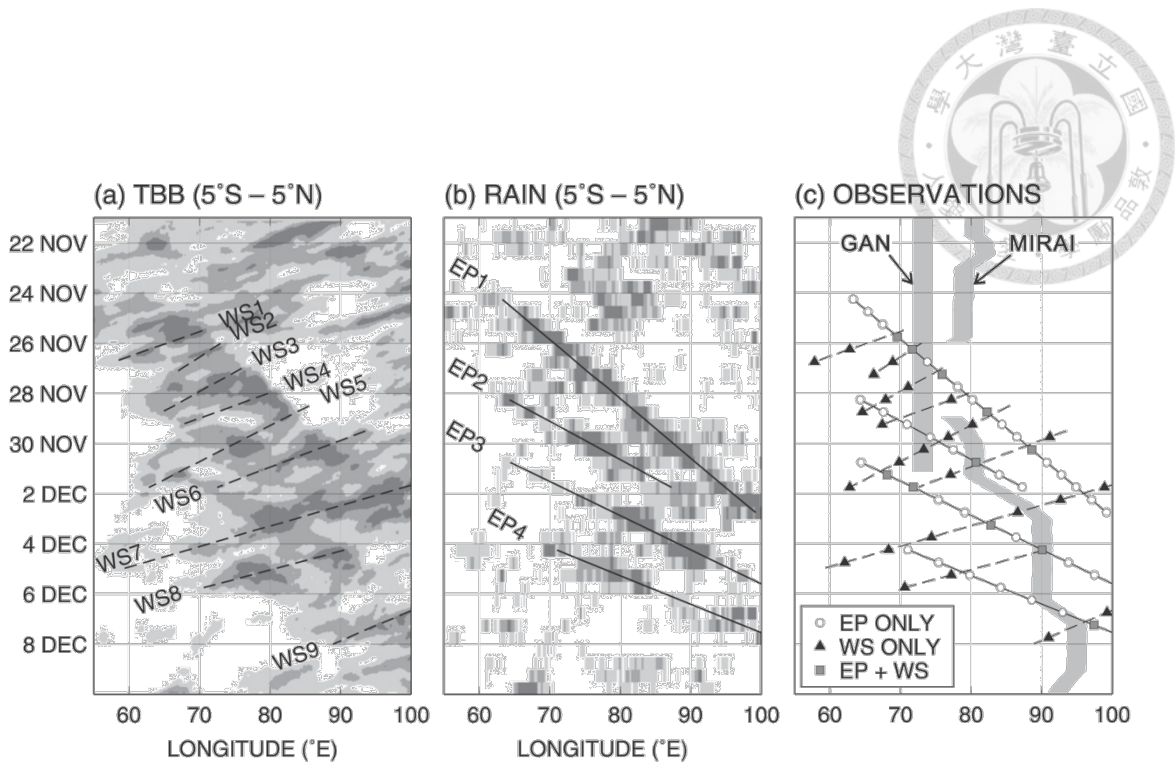
Figure 1.7.　　Time-longitude diagrams of (a) the cloud-top temperature and (b) rainfall rate. Solid and dashed lines indicate eastward-propagating precipitating systems (EP1– EP4) and westward-propagating cloud shields (WS1–WS9), respectively. (c) Classification of 12-hourly observational points into three types. The longitude of each point corresponds to the center of the zonal axis in the composite datasets. (Figure 8 in Yamada et al. 2010)

75
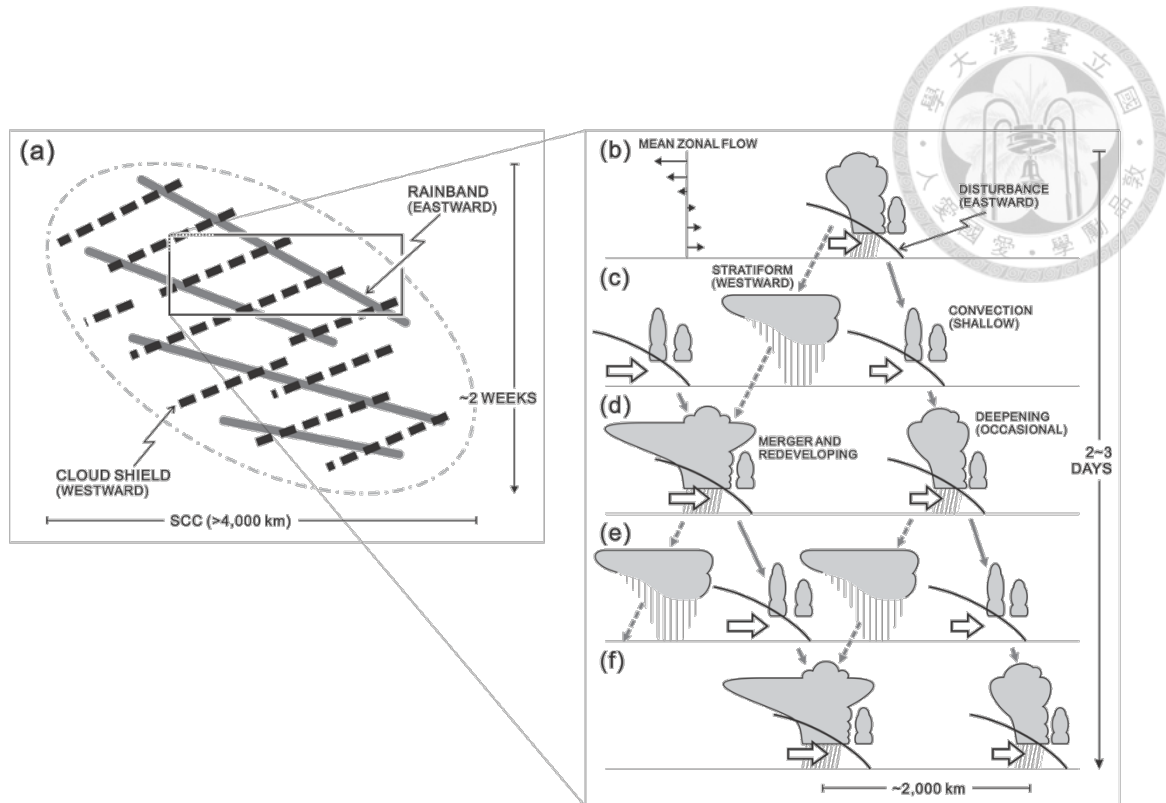
Figure 1.8.   Schematic of the mesoscale structure of the super cloud cluster (SCC) during MISMO, (a) view in the zonal–time section and (b)–(f) series of the zonal–vertical sections. (Figure 15 in Yamada et al. 2010)

76
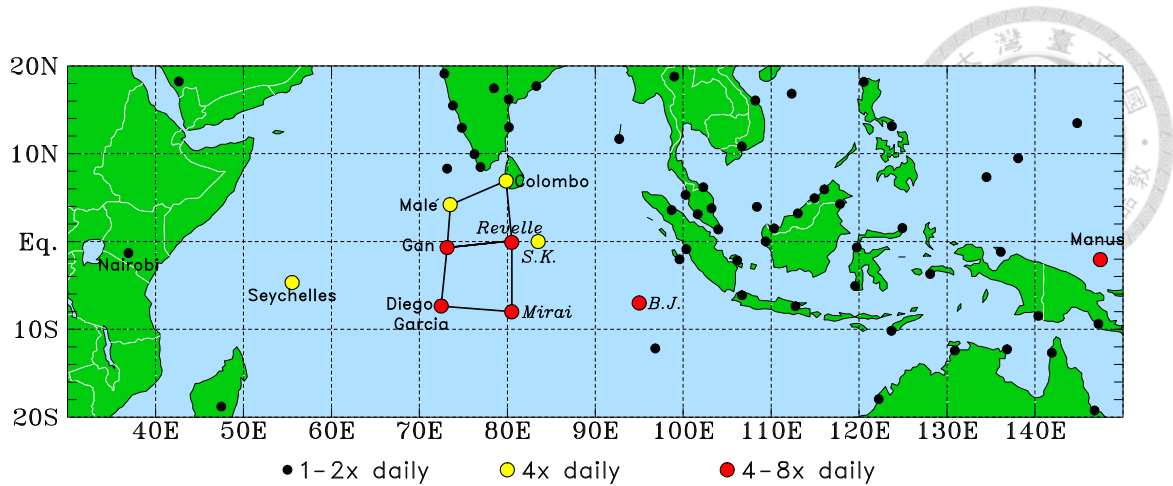
Figure 1.9.   DYNAMO–CINDY–AMIE radiosonde observation network for the period October–December 2011, including high-frequency soundings (4 and 8 launches per day; yellow and red dots, respectively) and operational sounding sites (1 or 2 launches per day; black dots). Solid lines indicate the enhanced southern/northern sounding arrays during the SOP in the central IO, which consists of Gan Island (Addu Atoll) and Male, Maldives; Diego Garcia Island, Colombo, Sri Lanka; and two ship sites at 0°, 80.5°E and 8°S, 80.5°E. (Figure 1 in Johnson et al 2015)
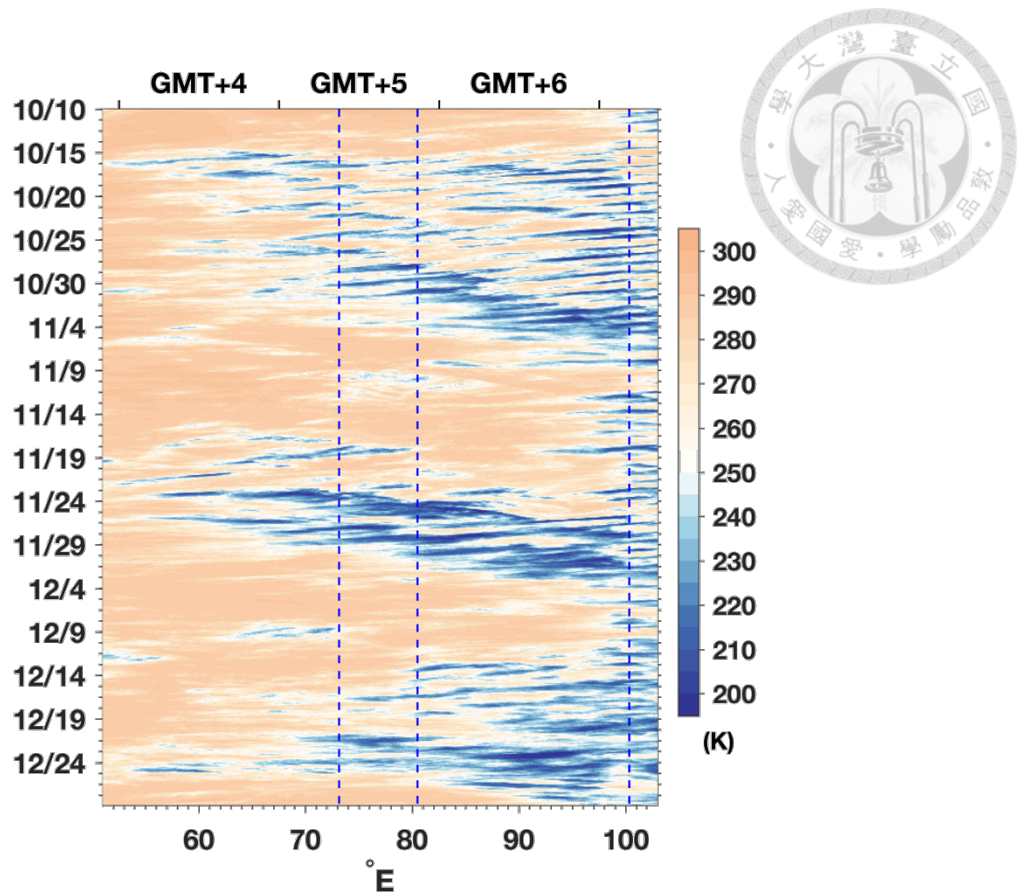
Figure 1.10. Time-longitude diagram of satellite infrared brightness temperature (K, colored) averaged over 150 km north and south of the latitude of Gan over the IO region from 10 October to 28 December 2011. The blue dashed lines, from left to right, indicate the longitudes of sites at Gan Island (73.15°E), R/V *Revelle* (80.5°E) and Padang on Sumatra Island (100.35°E). The ordinate is the date-time in UTC (00Z), and the upper abscissa is the local time zone to Greenwich Mean Time (GMT).
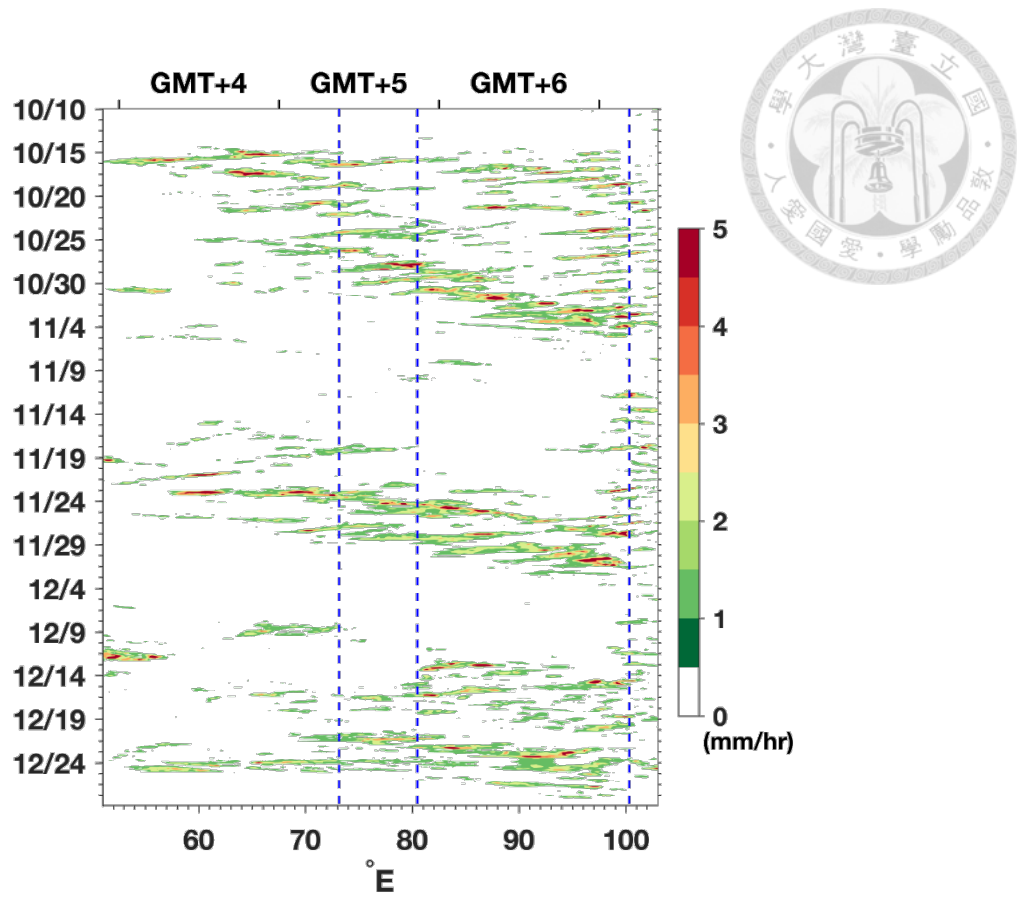
Figure 1.11.   Similar to Figure 1.10 except for TRMM rain rate.
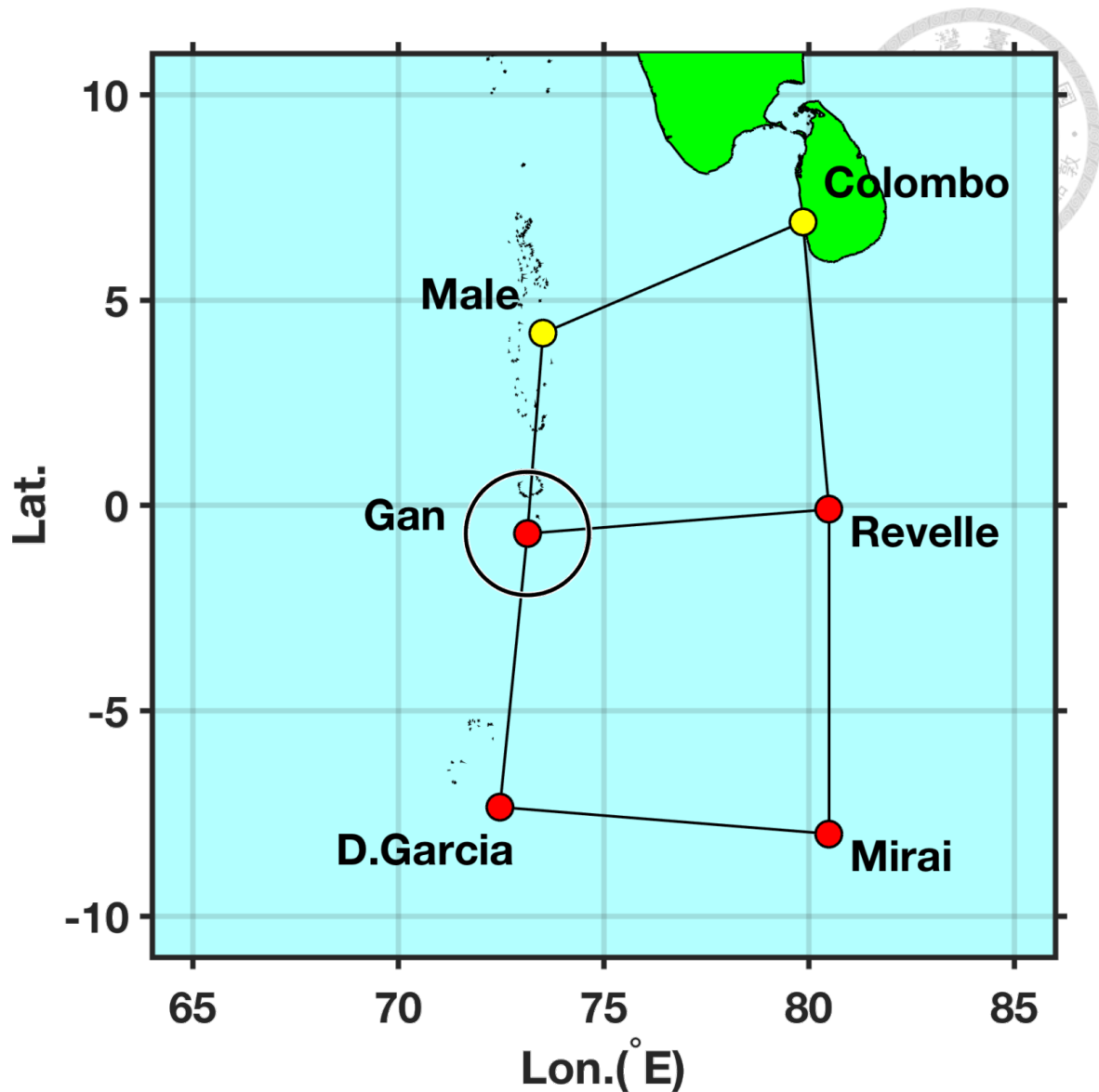
Figure 2.1. The DYNAMO enhanced sounding array (ESA) in the central equatorial

IO during DYNAMO SOP. High frequency sounding sites with 8 launches (4 launches)

per day are indicated with red (yellow) circles. Most analyses in this study focus on Gan

at 0.69°S, 73.15°E. The outer black circle around Gan indicates the 150-km radius.

circular region for satellite data averaging and the AMIE-Gan large-scale objective

analysis domain.
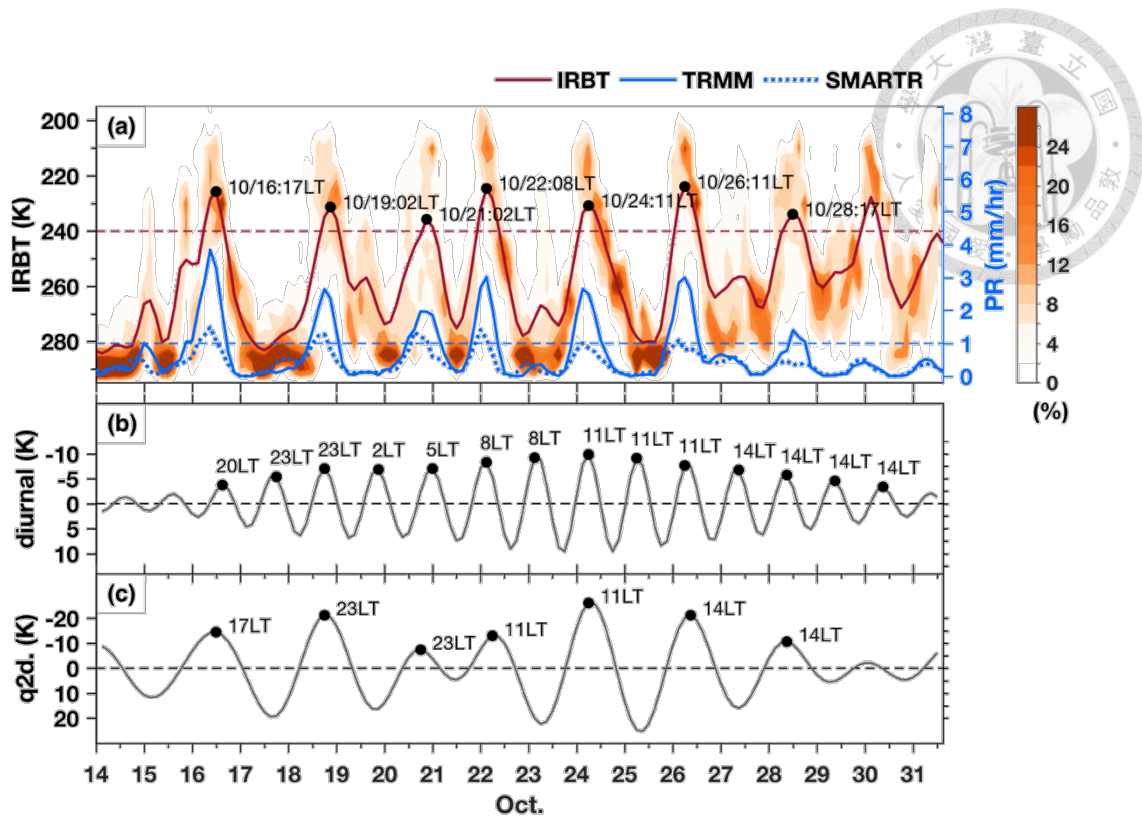
Figure 3.1.   (a) Time series of IRBT areal percentage in 5 K intervals (%; colored) and 6-hourly running averaged IRBT (K; red solid curve), TRMM 3B42 rain rate (mm/hr; blue solid curve) and adjusted SMART-R surface rain rate (mm/hr; blue dotted curve) over the 150-km radius circular region around Gan (as indicated in Figure 2.1) during late October 2011. The times of seven selected quasi-2-day (q2d.) convective events are indicated with black dots and labeled with local time at Gan (GMT+5). The criteria for the convectively active events are indicated with IRBT peaks <240 K (red dashed line) and averaged TRMM rain rate peaks >1 mm/hr (blue dashed line). (b) Time series of filtered IRBT signal within a diurnal frequency band (0.9–1.2 day). The dashed black line indicates zero. (c) Same as (b) except for quasi-2-day frequency band (1.6–3 day). Times of low peaks are indicated in both (b) and (c) with black dots and labeled with local time at Gan (GMT+5). Note that the ordinate for IRBT on the left of (a) is in reverse order. And the abscissa indicates the date-time in UTC (00Z).
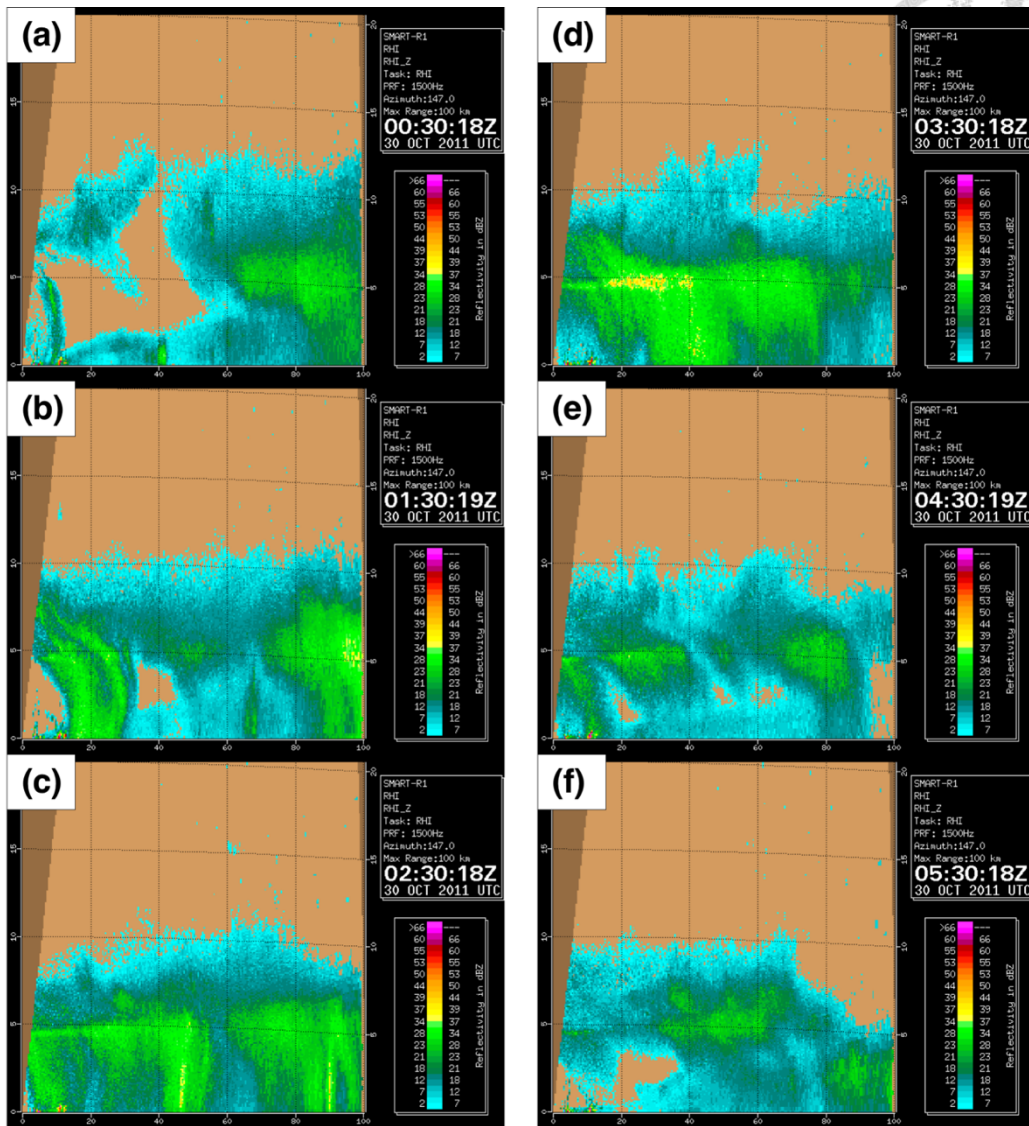
Figure 3.2.   Images of SMART-R range height indicator (RHI) scans at Gan on 30 October 2011. From (a) to (f), 00:30Z, 01:30Z, 02:30Z, 03:30Z, 04:30Z, and 05:30Z. The averaged rain rate over Gan reached a maximum around 03Z according to Figure 3.1. The azimuthal angle is 147° out to a range of 100 km. Images are available at

http://catalog.eol.ucar.edu/cgi-

bin/dynamo/research/prod_browse?platform=SMARTR&prod=smartr_DBZ_RHI_147d

eg&howmany=Use+Start%2FEnd+Dates+-

%3E&start=20111029&end=20111031&submit=retrieve+products.

82
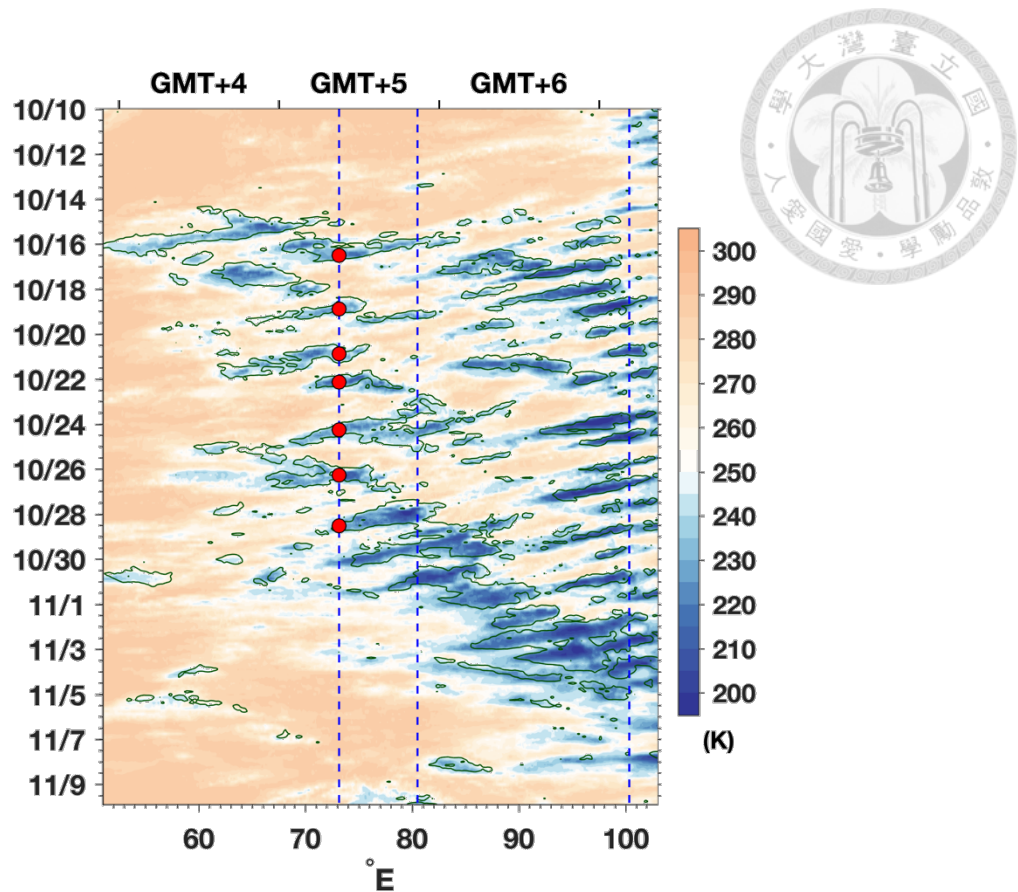
Figure 4.1.   Time-longitude diagram of IRBT (K, colored) and TRMM rain rate (green contours for 1 mm/hr) averaged over 150 km north and south of the latitude of Gan over the IO region from 10 October to 10 November 2011. The blue dashed lines, from left to right, indicate the longitudes of sites at Gan Island (73.15°E), R/V *Revelle* (80.5°E) and Padang on Sumatra Island (100.35°E). The red dots along the longitude of Gan Island indicate the time of convective events listed in Table 3.1. The ordinate is the date-time in UTC (00Z), and the upper abscissa is the local time zone to GMT.
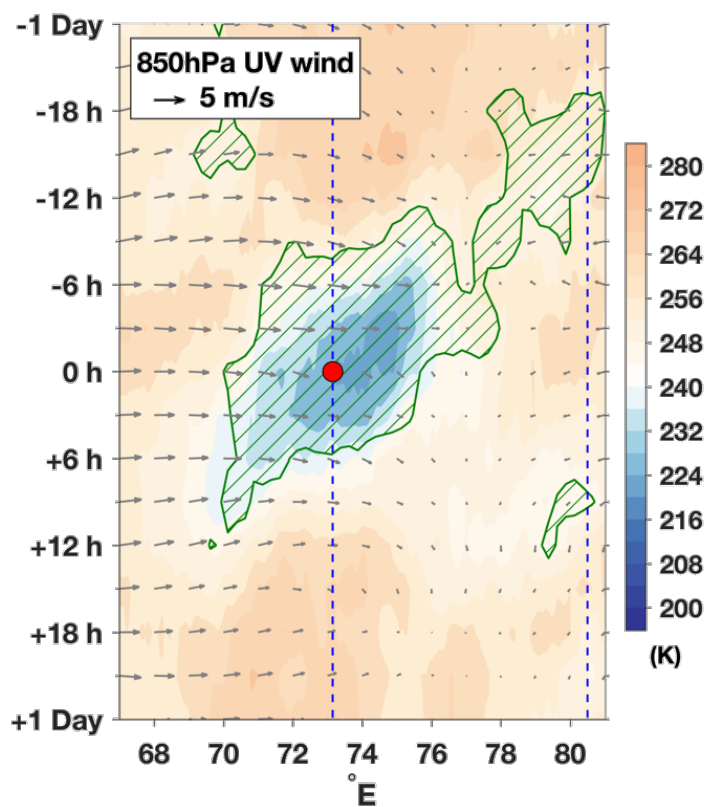
Figure 4.2.   Similar to Figure 4.1 except for the quasi-2-day convective events composite. The red dot in the center indicates 0 h of each case. The green hatched contours indicate the TRMM rain rate composite >1 mm/hr, the gray arrows the 850-hPa total wind composite, and the two blue dashed lines, the longitudes of Gan Island (left) and R/V *Revelle* (right).

84
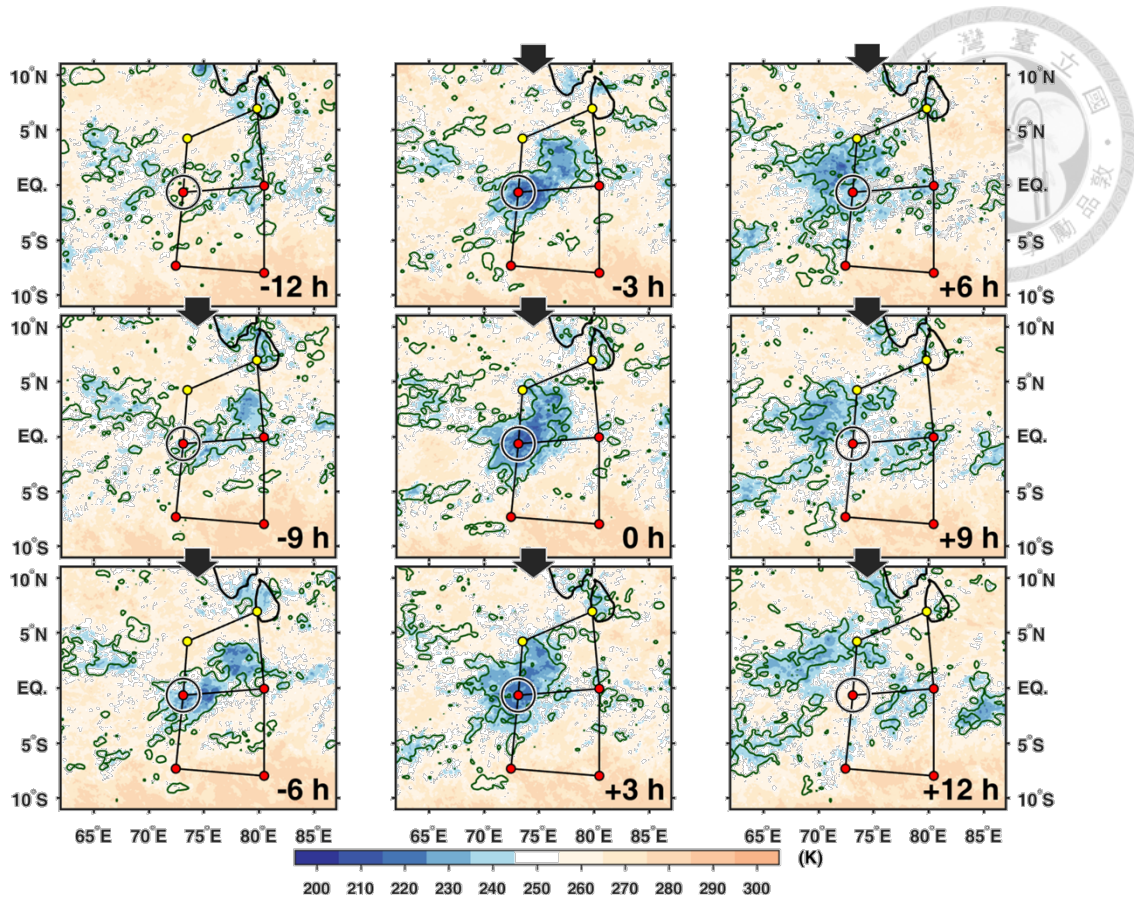
Figure 4.3. Composite IRBT (colored) and TRMM rain rate (green contours for 1 mm/hr) horizontal distributions of the quasi-2-day convective events. The 150-km region around Gan was indicated in a black circle. The times relative to 0 h are indicated on the bottom right in each subfigure. The composites are shown from –12 h to +12 h which comprises the time window of primary convective activity associated with the quasi-2-day events.

85

doi:10.6342/NTU201801684
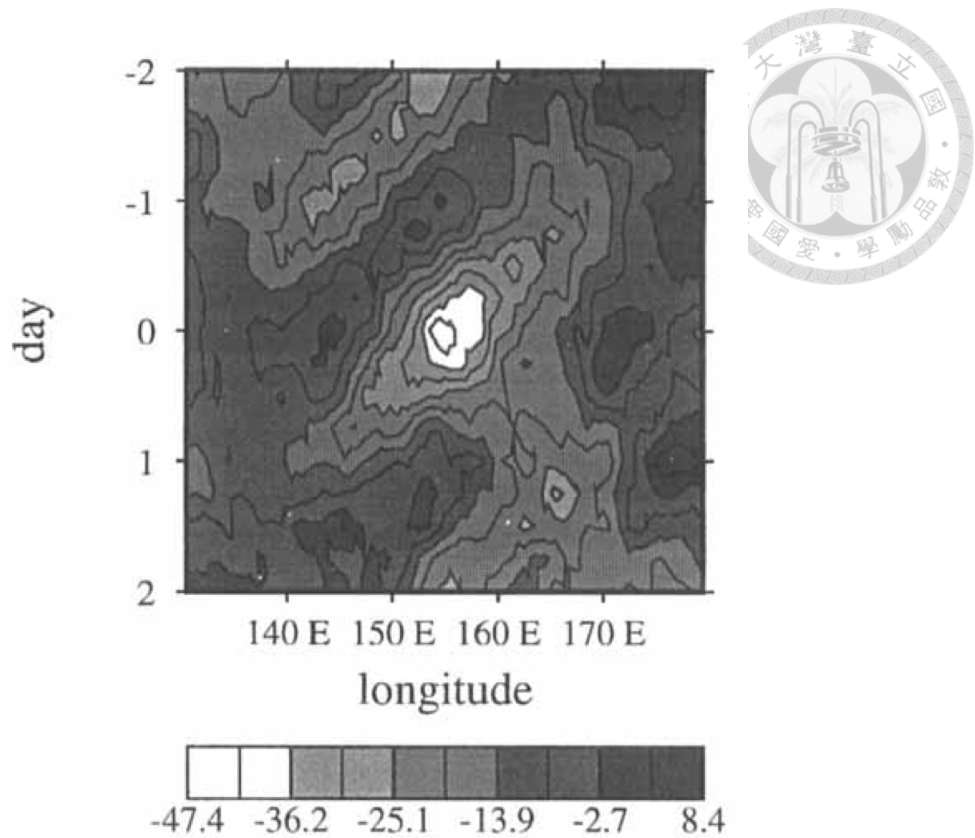
Figure 4.4. Composite time-longitude series of brightness temperature (°C). Averaging is done from 5°S to 5°N for all but two cases during TOGA COARE (22, 24 Dec. 1992). For these cases, the averaging is done from 10°S to the equator. (Figure 9 in Haertel and Johnson 1998)
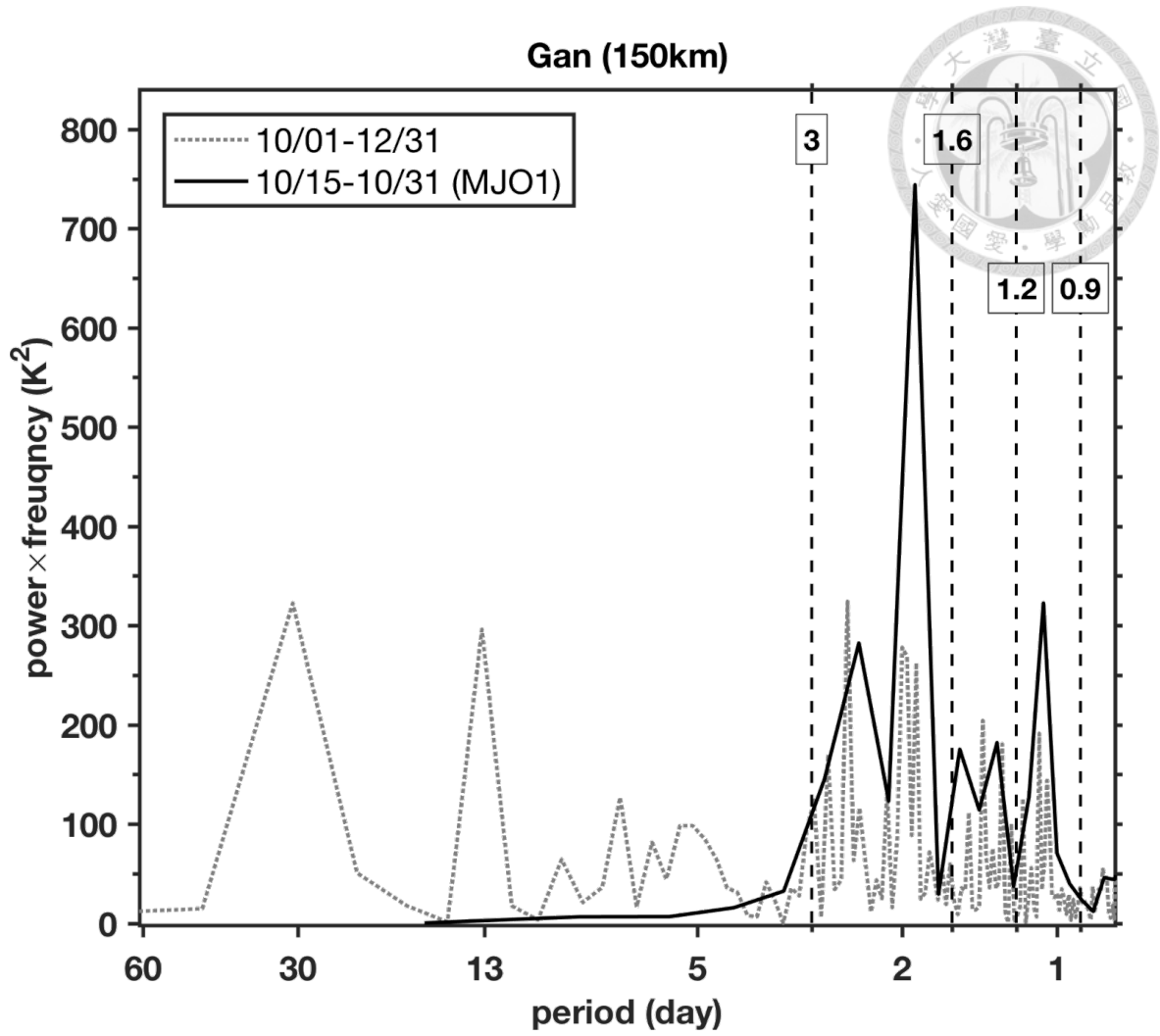
Figure 5.1. Fourier power spectrum of averaged IRBT over the 150-km region around Gan during October-December 2011 (gray dotted) and MJO1 period (black solid). The vertical dashed lines from left to right correspond to the periods of 3, 1.6, 1.2, and 0.9 days, as labeled.
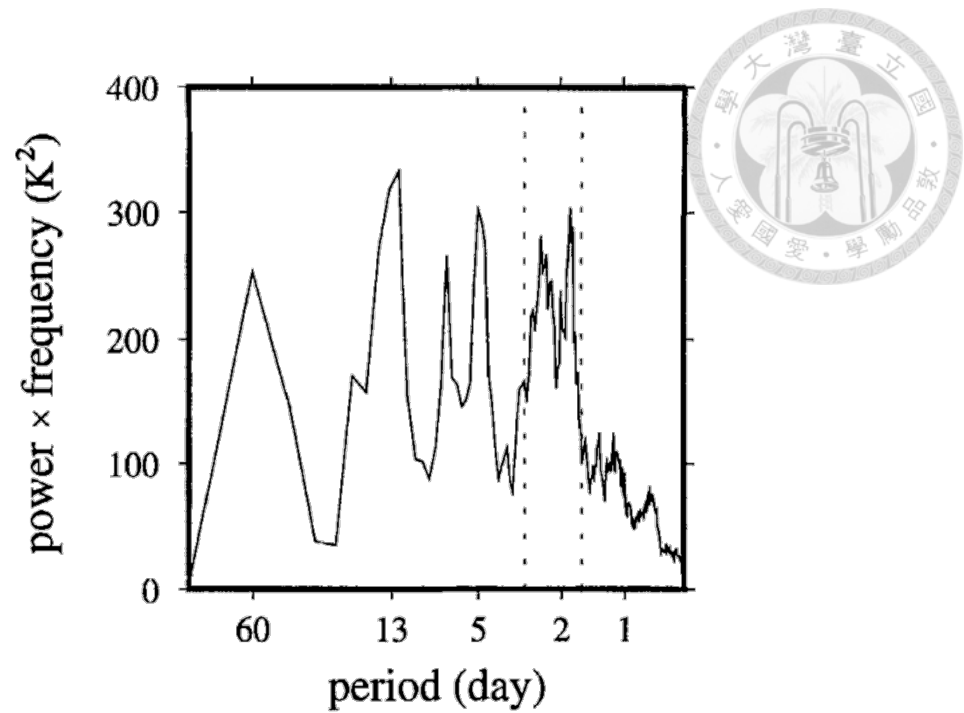
Figure 5.2. Fourier power spectrum of averaged brightness temperature over IFA for the period from November 1992 to February 1993 during TOGA COARE. The vertical dotted lines correspond to periods of 1.6 and 3.0 days. (Figure 5 in Haertel and Johnson 1998)
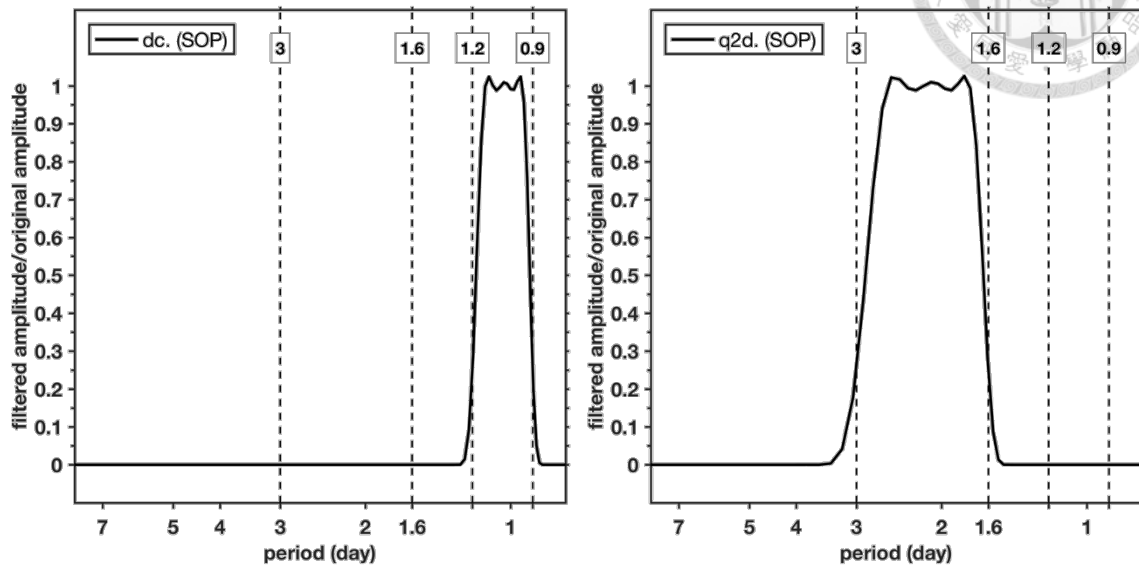
Figure 5.3.   The response functions for diurnal (dc.; left) and quasi-2-day (q2d.; right)

frequency bands associated with the Lanczos bandpass filter used in this study.
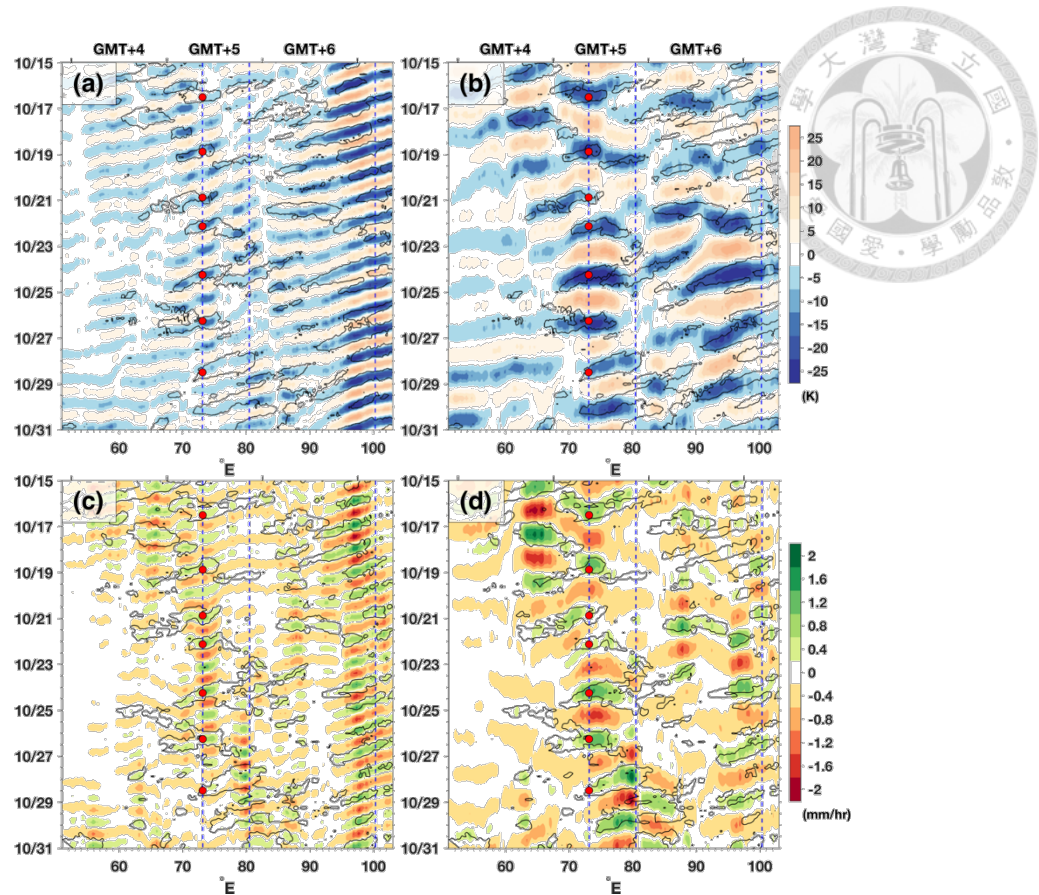
Figure 5.4. (a), (b): Time-longitude diagrams of the filtered IRBT variations with (a) diurnal periodicity (0.9–1.2 day) and (b) quasi-2-day periodicity (1.6–3 day) during MJO1. The black contours in both figures indicate the unfiltered averaged IRBT <240 K. (c), (d): as in (a) and (b), except for the filtered TRMM rain rate variations. The black contours here indicate the unfiltered averaged TRMM rain rate >1 mm/hr. In all subfigures, the blue dashed lines, from left to right, indicate the longitudes of sites at Gan Island (73.15°E), R/V *Revelle* (80.5°E) and Padang on Sumatra Island (100.35°E). The red dots along the longitude of Gan Island indicate the time of convective events listed in Table 3.1. The ordinate is the date-time in UTC (00Z), and the upper abscissa is the local time zone to GMT.

90
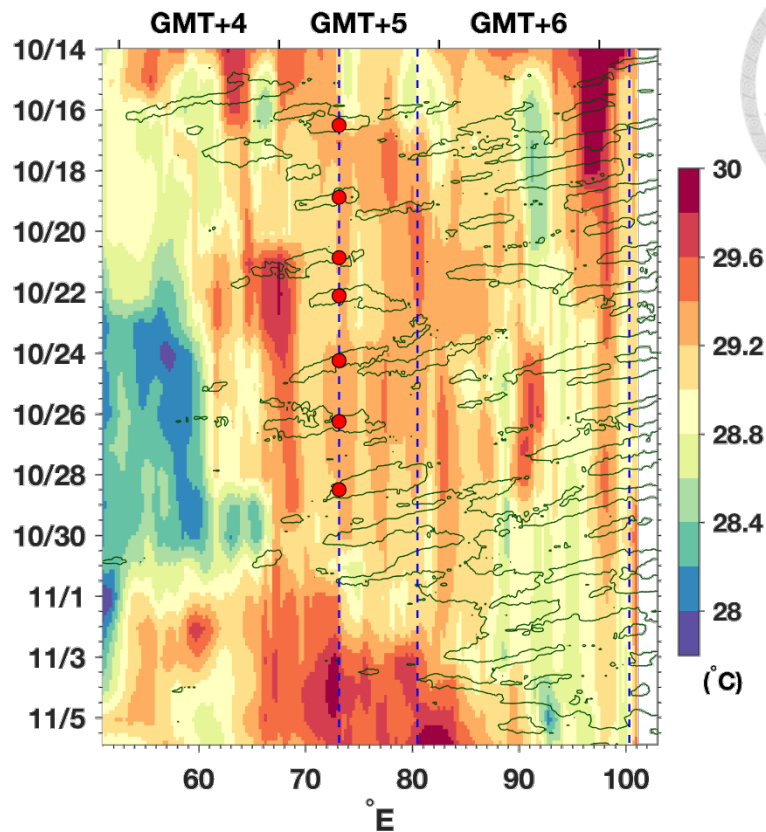
Figure 5.5.　Time-longitude diagram of NOAA High Resolution SST (°C, colored) provided by the NOAA/OAR/ESRL PSD (data available at https://www.esrl.noaa.gov/psd/data/gridded/data.noaa.oisst.v2.highres.html) and IRBT (green contours for 240K) averaged over 150 km north and south of the latitude of Gan over the IO region from 14 October to 5 November 2011. The blue dashed lines, from left to right, indicate the longitudes of sites at Gan Island (73.15°E), R/V *Revelle* (80.5°E) and Padang on Sumatra Island (100.35°E). The red dots along the longitude of Gan Island indicate the time of convective events listed in Table 3.1. The ordinate is the date-time in UTC (00Z), and the upper abscissa is the local time zone to GMT.
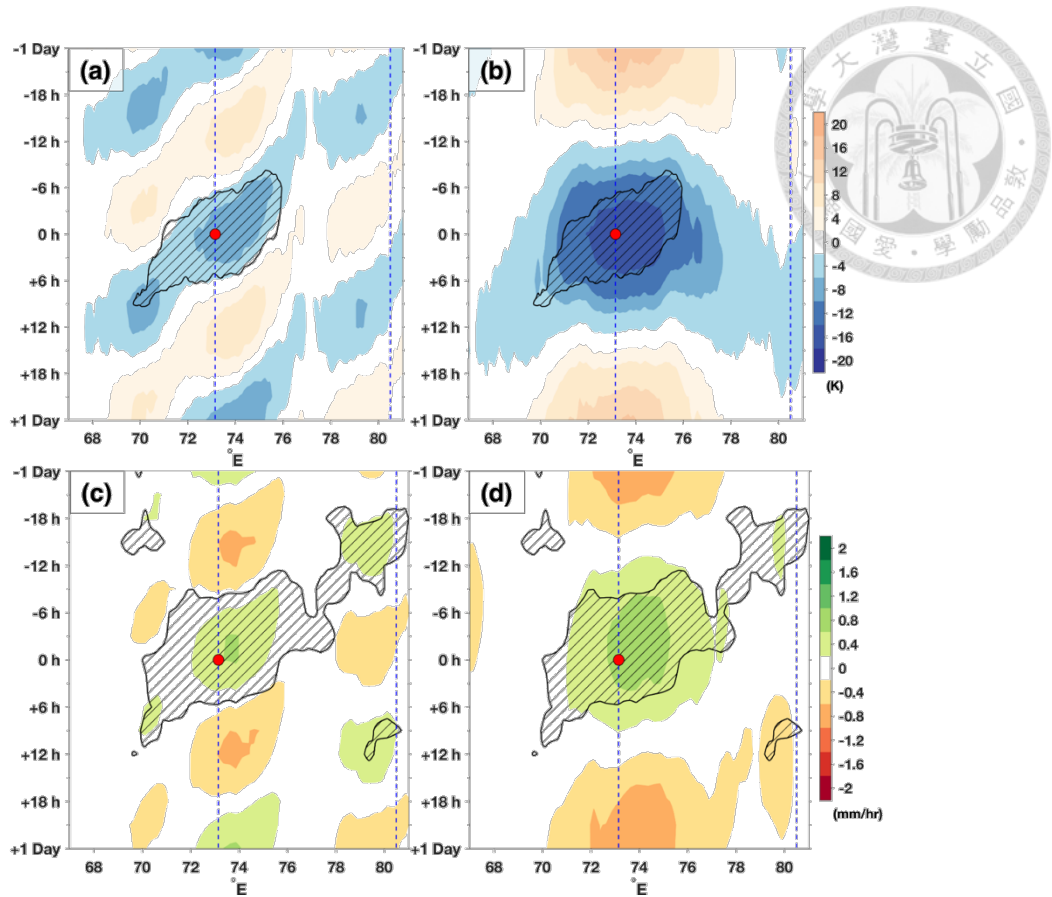
Figure 5.6.   Similar to Figure 5.4 except for the seven convective events composites. The black hatched contours indicate the unfiltered average IRBT composite <240 K in (a) and (b), and unfiltered average TRMM rain rate composite >1 mm/hr in (c) and (d). Red dots in all subfigures denotes 0 h for the quasi-2-day events.
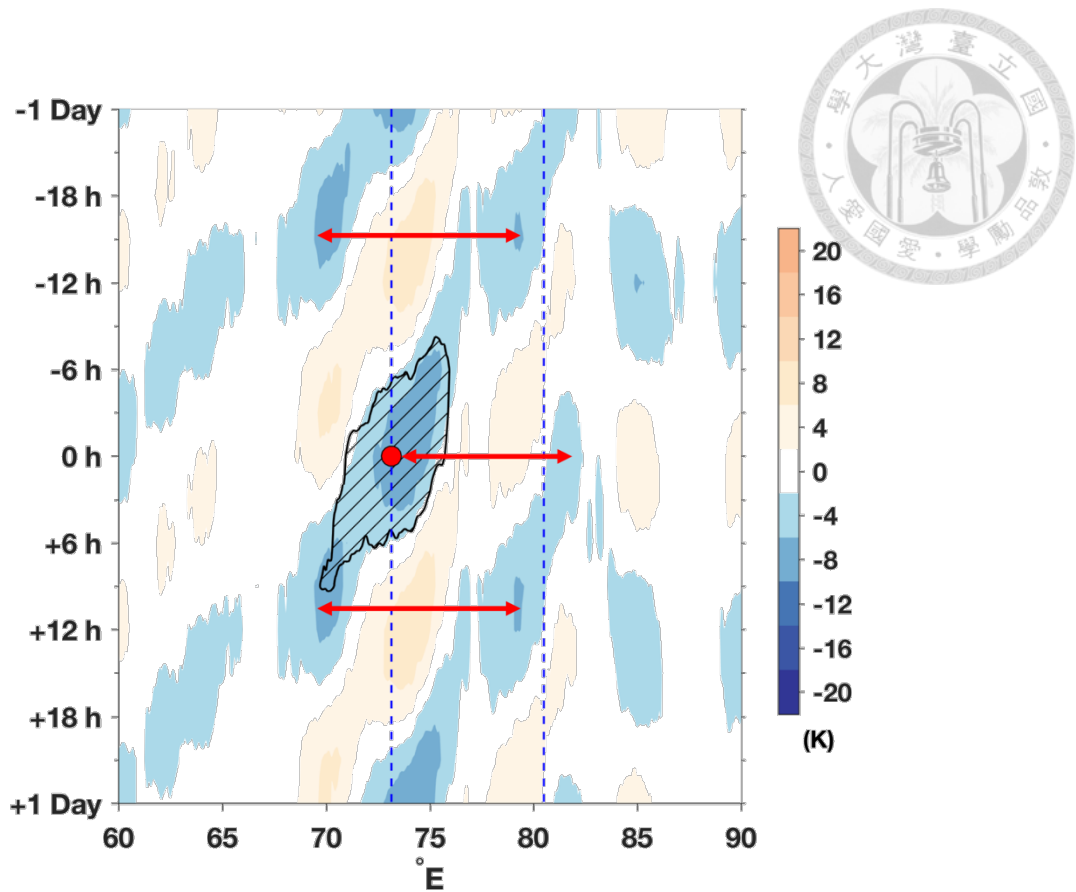
Figure 5.7.   Similar to Figure 5.6a except the longitude ranges from 60°E to 90°E. The red double arrows indicate the estimated zonal spatial scales of propagating diurnal signals.
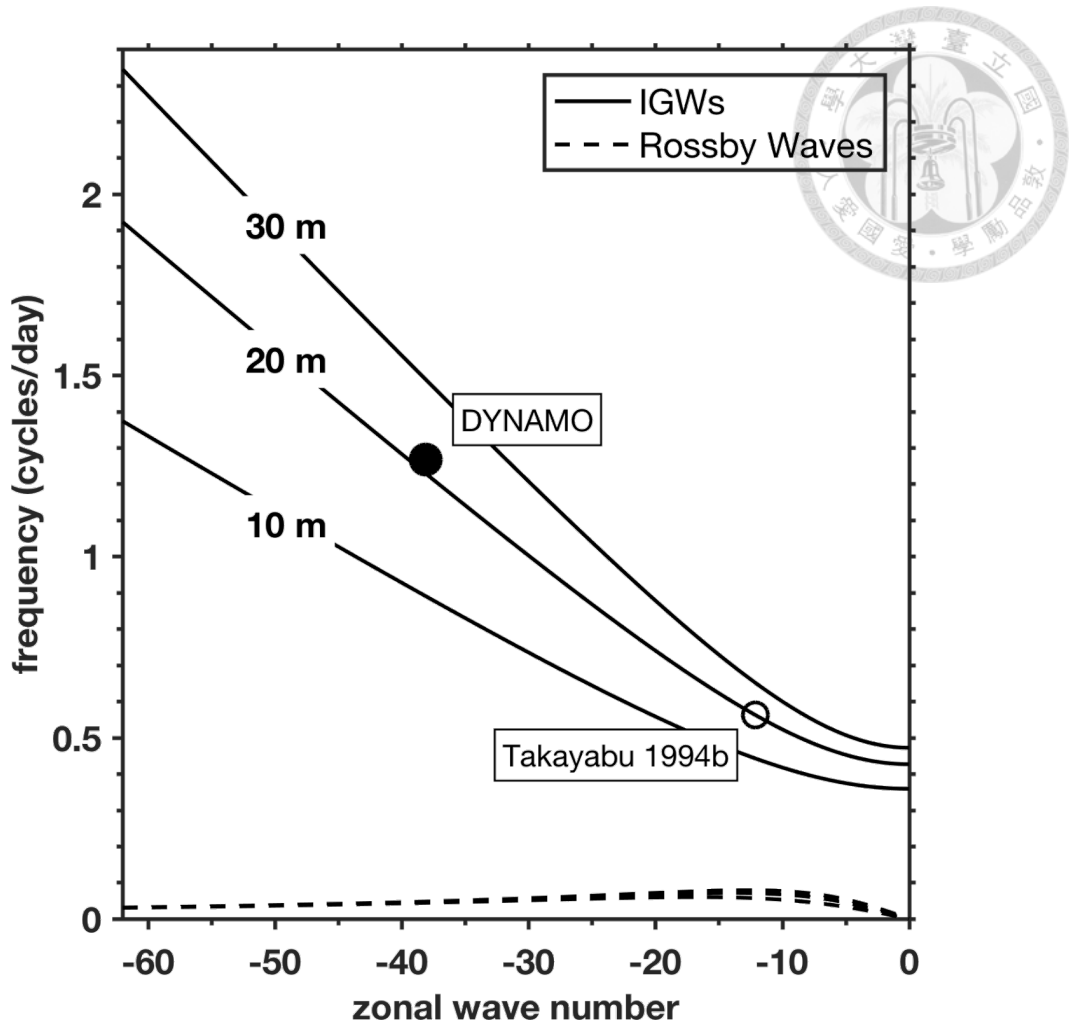
Figure 5.8.　Dispersion diagram with an estimated characteristic value of the propagating diurnal signals within the seven quasi-2-day convective events obtained from the composite during DYNAMO (black dot), and that estimated in Takayabu 1994b (black circle). Similar to Figure 8 in Takayabu 1994b, the dispersion curves indicate the $n=1$ westward-propagating inertia-gravity waves (solid) and $n=1$ Rossby waves (dashed) with the equivalent depths of 10m, 20m, and 30m, respectively.
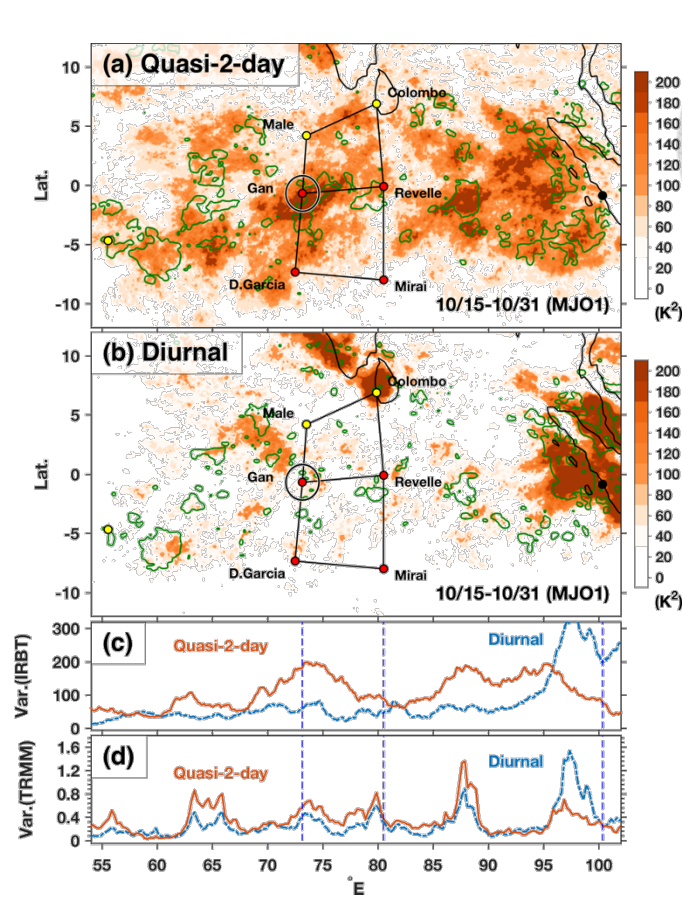
Figure 5.9.   Maps of IRBT and TRMM rain rate variances over tropical IO during MJO1 for (a) quasi-2-day (1.6–3 day) and (b) diurnal (0.9–1.2 day) periodicity. The colored regions indicate the IRBT variance, the green contours indicate the TRMM rain rate variance >0.64 mm^2/hr^2. (c): The mean variances of IRBT over 150-km north and south of Gan during MJO1. The red (blue) curve indicates the quasi-2-day (diurnal) variance as a function of longitude, and the blue vertical dashed lines indicate from left to right the longitudes of Gan Island, R/V *Revelle* and Padang on Sumatra Island. (d): Same as (c) except for the mean variances of TRMM rain rate.

95
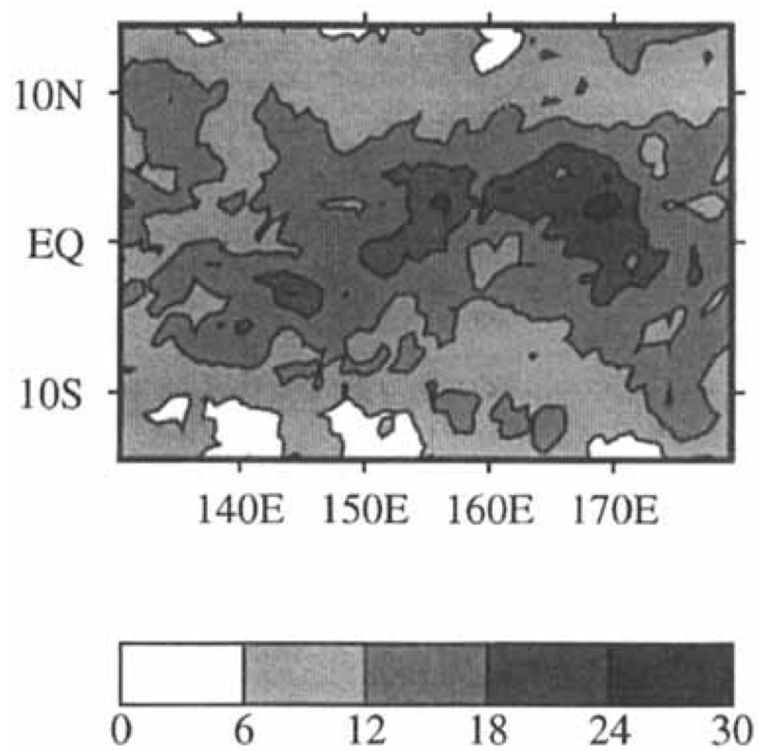
Figure 5.10.   The percentage of brightness temperature variance associated with 1.6 to

3-day Fourier components for the period 11 November 1992 to 19 February 1993. (Figure

7 in Haertel and Johnson 1998)
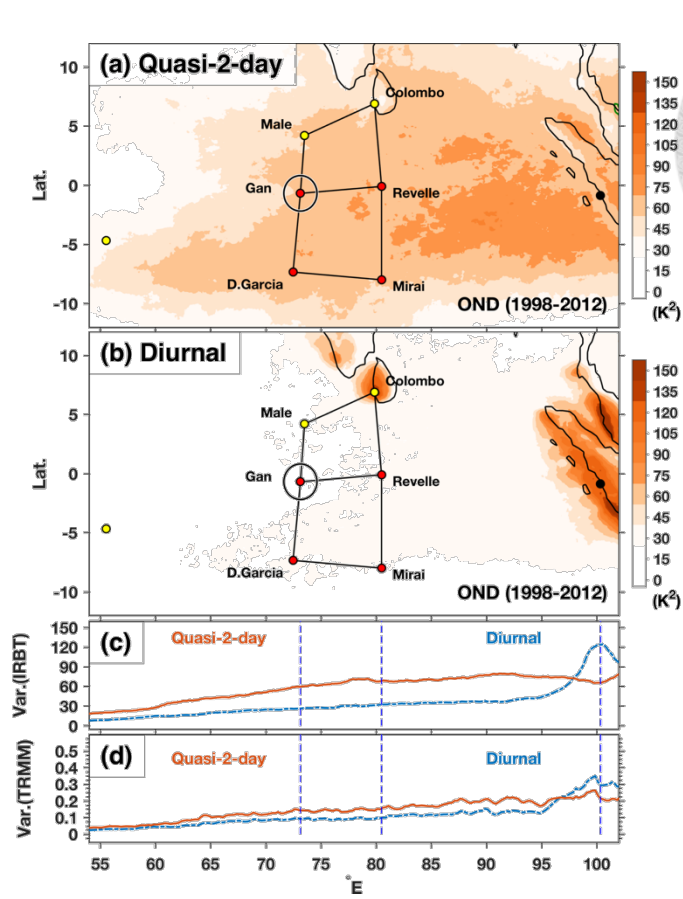
Figure 5.11.   Same as Figure 5.9 except for the averaged variance distribution during October, November, and December from 1998 to 2012.
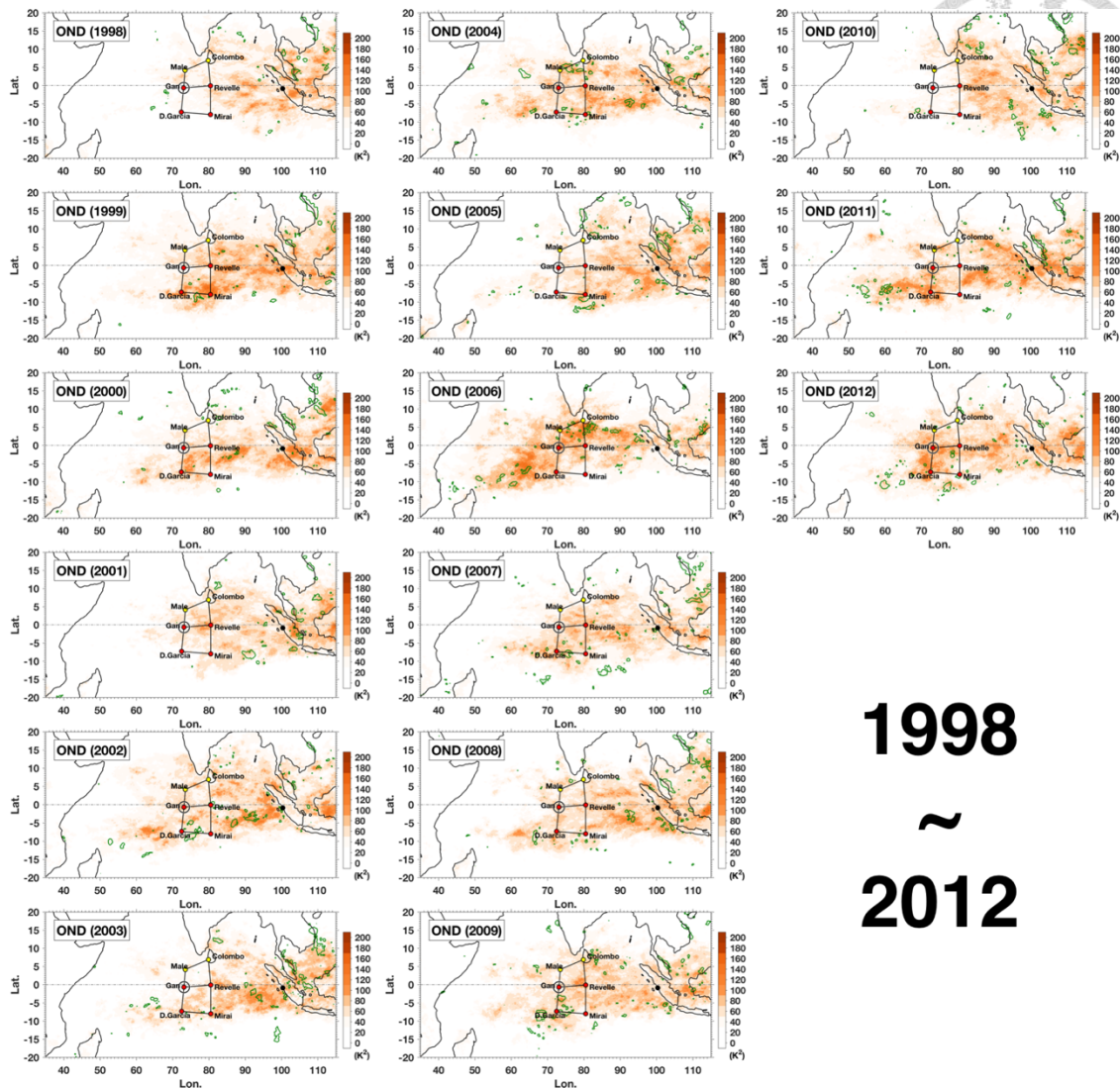
Figure 5.12. Each sub-figure shows the variance distribution of quasi-2-day signal over the IO from October to December for years from 1998 to 2012.
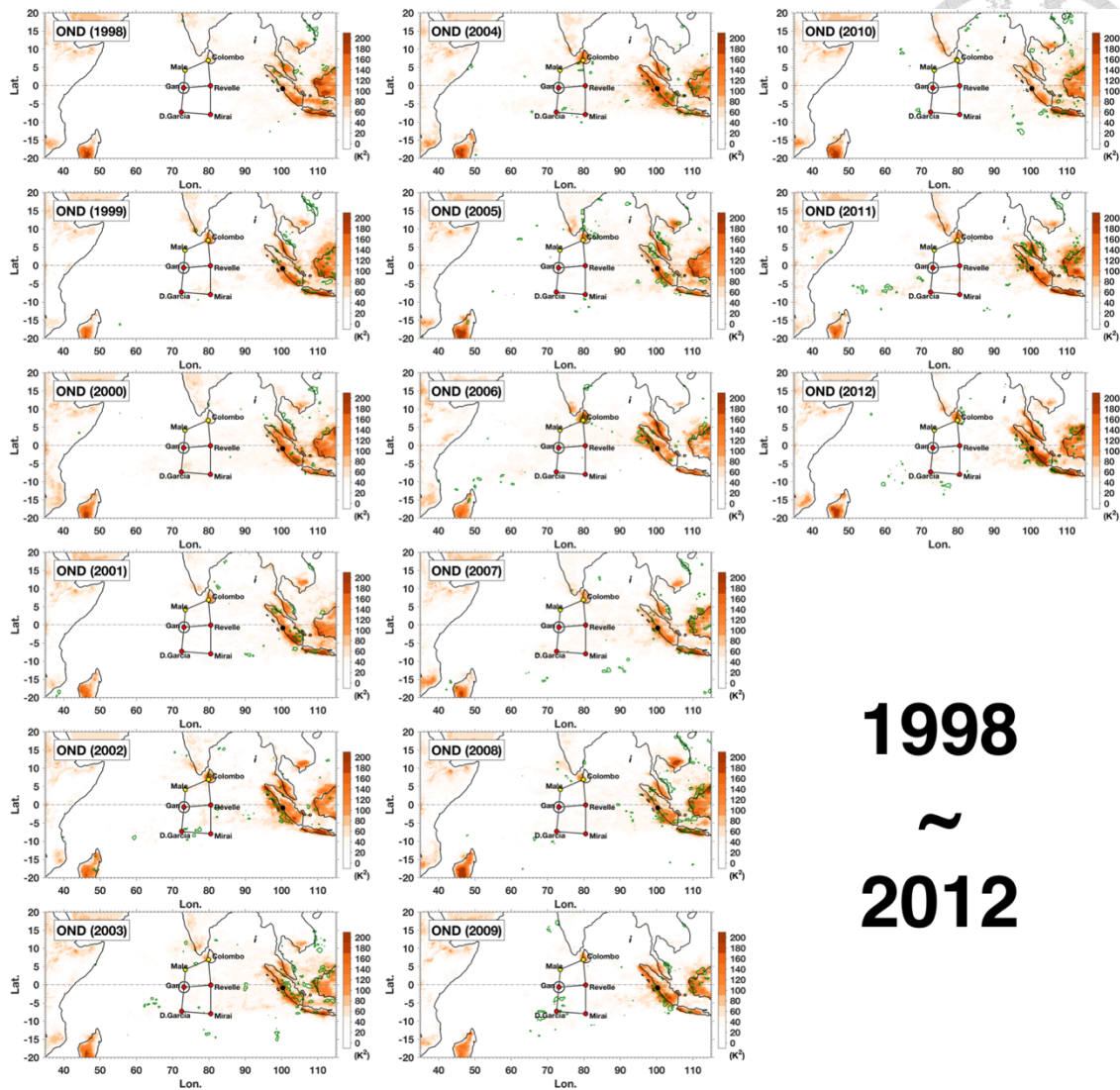
Figure 5.13.   Identical to Figure 5.12 except for the variance distribution of the diurnal signal.
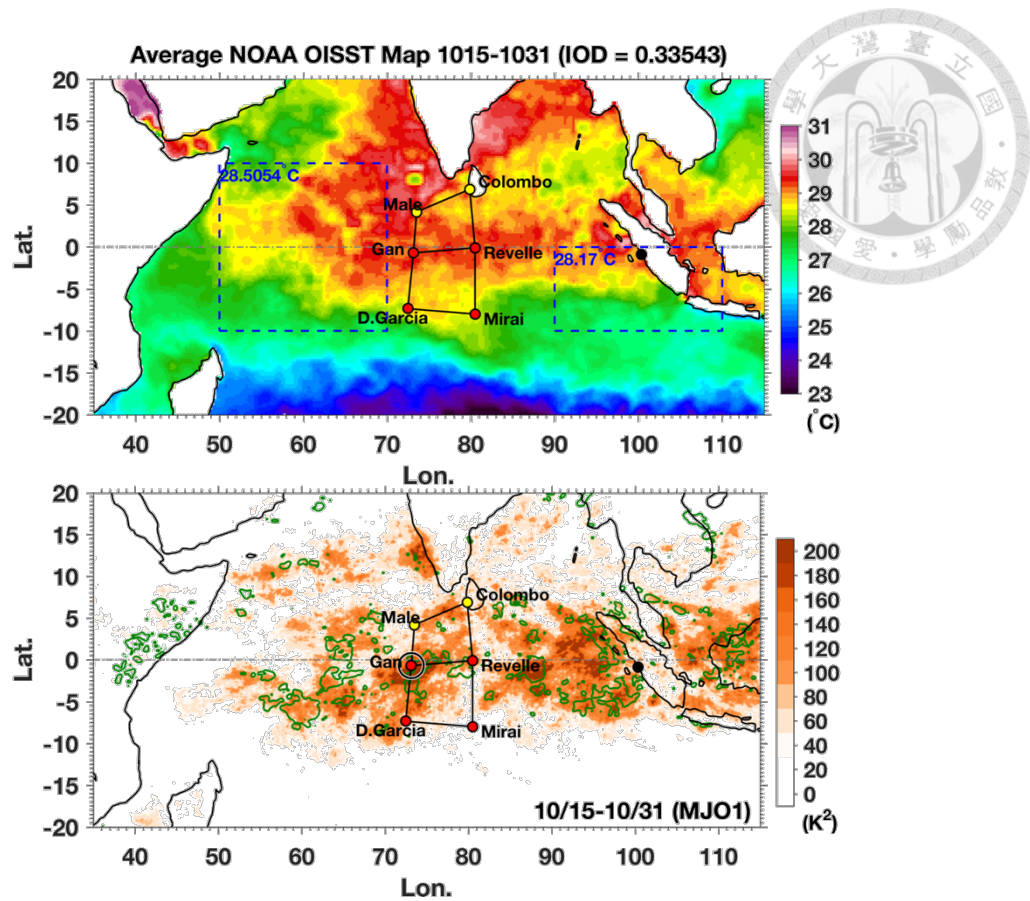
Figure 5.14.   (top) Spatial distribution of mean SST over the IO averaged during MJO1 from NOAA OISST V2 dataset (0.25° resolution). The dashed blue boxes indicate the SST averaging areas for IOD index calculation according to Saji et al. (1999), the averaged values of SST are shown in the top left of each box and the calculated IOD index is shown in the title. (bottom) Spatial distribution of quasi-2-day signal variance same as Figure 5.9a.
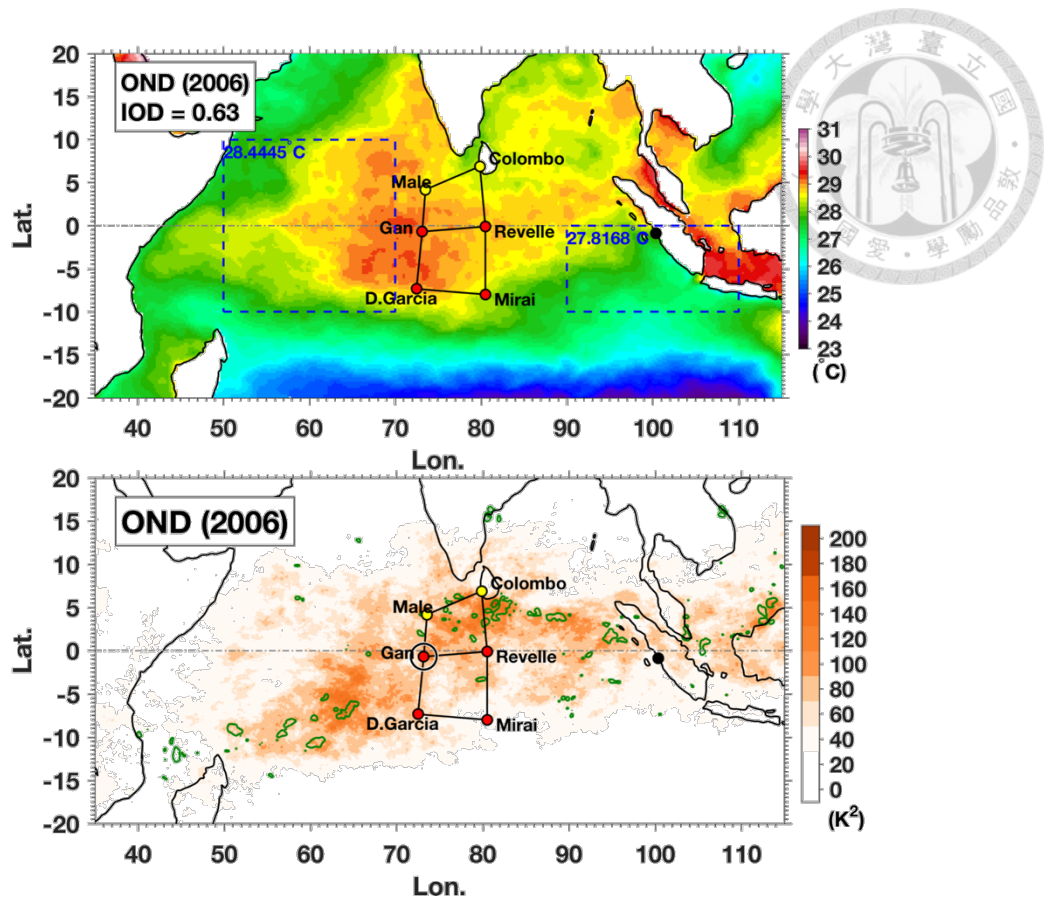
Figure 5.15.   (top) Spatial distribution of mean SST over the IO averaged from October to December in 2006. The dashed blue boxes indicate the SST averaging areas for IOD index calculation according to Saji et al. (1999), the averaged values of SST are shown in the top left of each box and the calculated IOD index is shown in the legend. (bottom) Spatial distribution of quasi-2-day signal variance similar to Figure 5.11a except for October to December 2006.

101
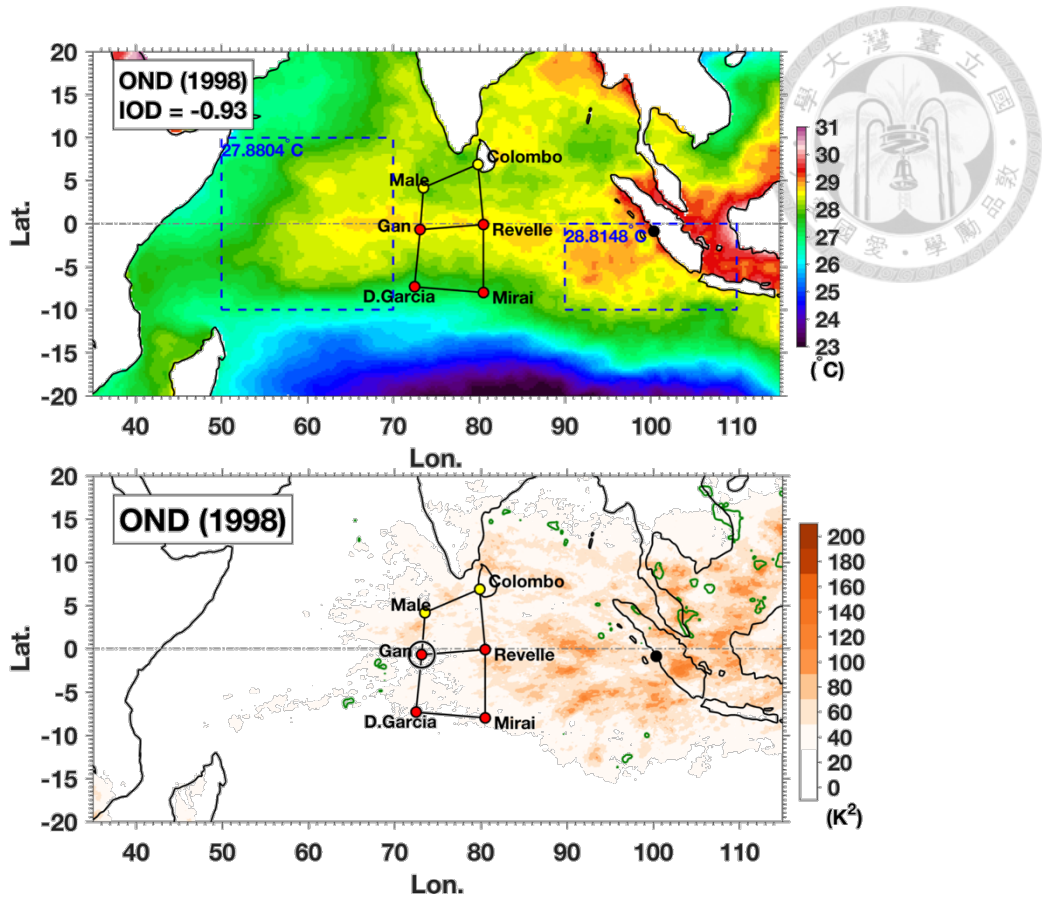
Figure 5.16.   Identical to Figure 5.15 except for the year 1998.
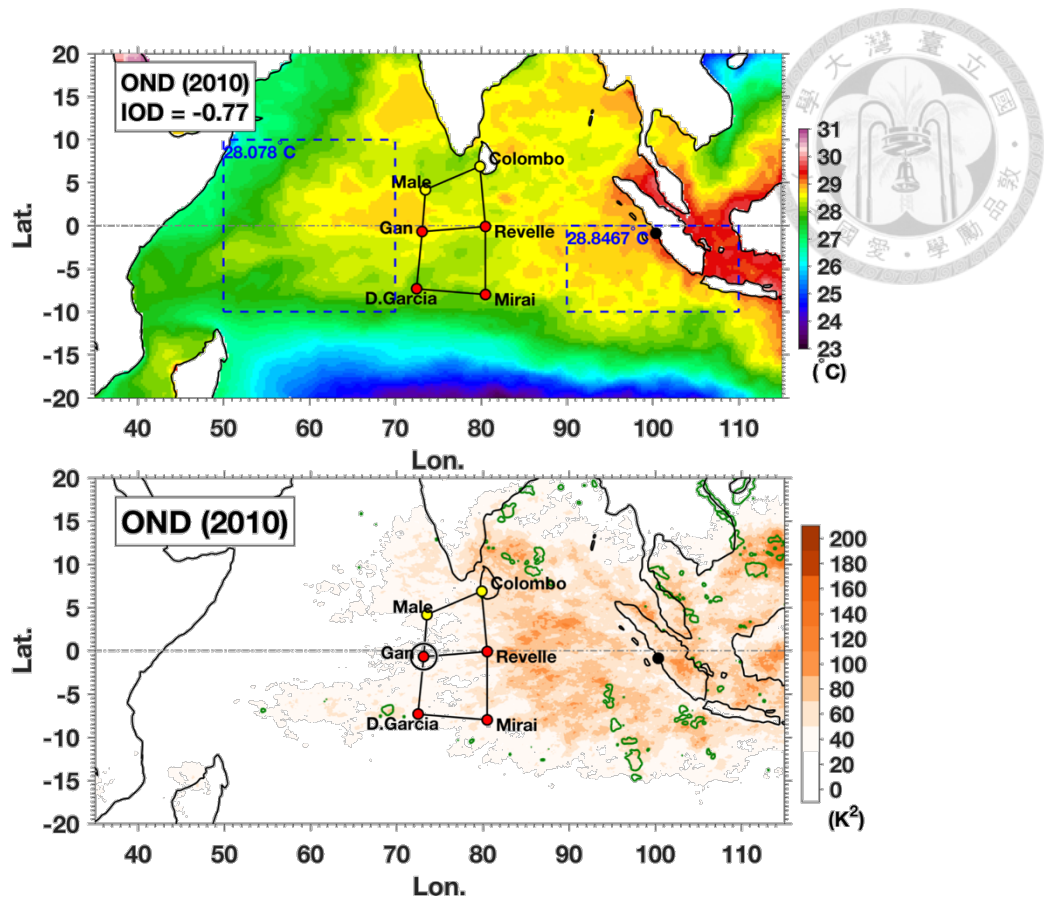
Figure 5.17.   Identical to Figure 5.15 except for the year 2010.
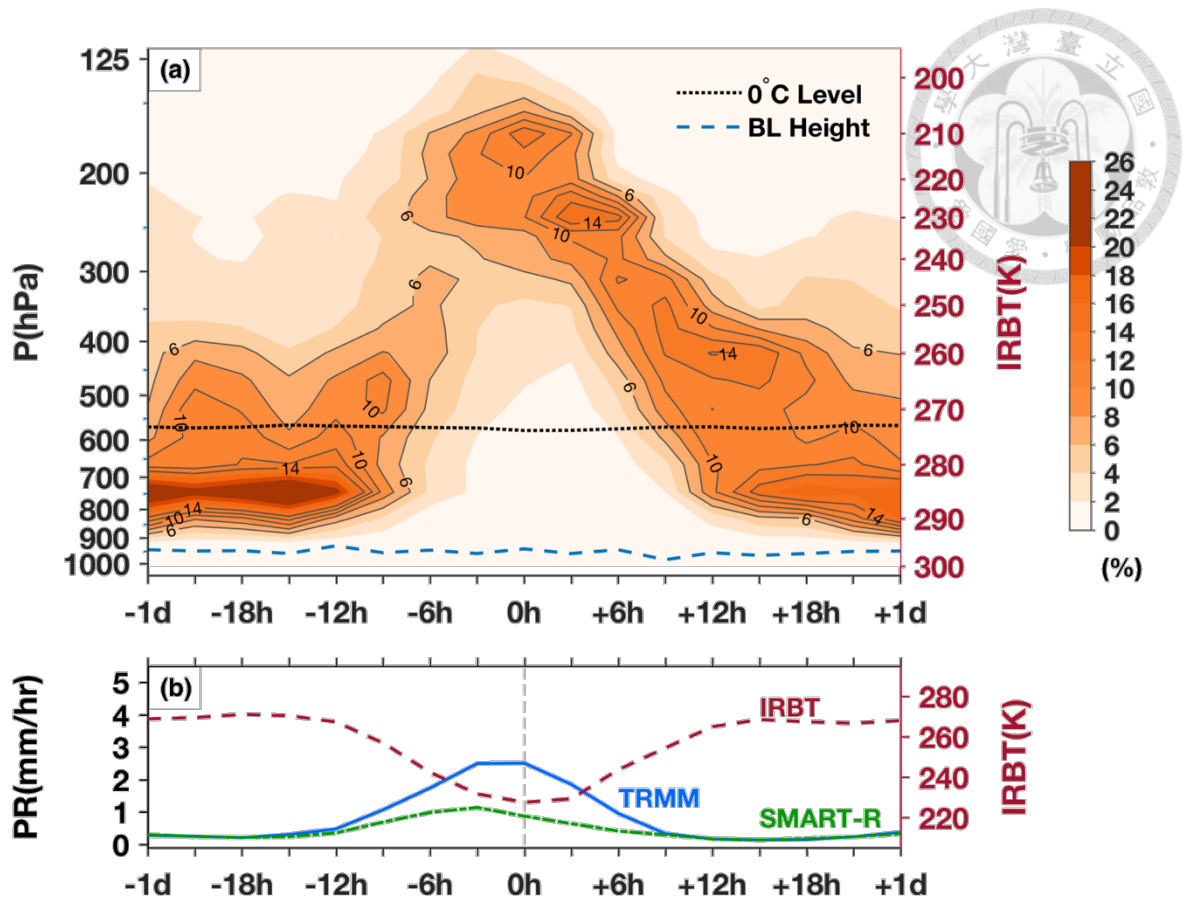
Figure 6.1.   The 48-hours window composites for the quasi-2-day convective events.
(a) Composite IRBT areal percentage (%) calculated as in Figure 3.1a. Black solid
contours indicate percentages from 6% to 14% with intervals of 2%. The black dotted
line near 600 hPa (blue dashed line near 950 hPa) indicates the period-mean 0°C level
height (boundary layer height) calculated from Gan radiosonde. The boundary layer
heights in the composite analysis are based on mixed layer depths reported in Johnson
and Ciesielski (2017). (b) Averaged IRBT (red dashed), averaged TRMM rain rate (blue
solid) and adjusted SMART-R surface rain rate (green dash-dotted) over Gan. The vertical
gray dotted line indicates 0 h.

104
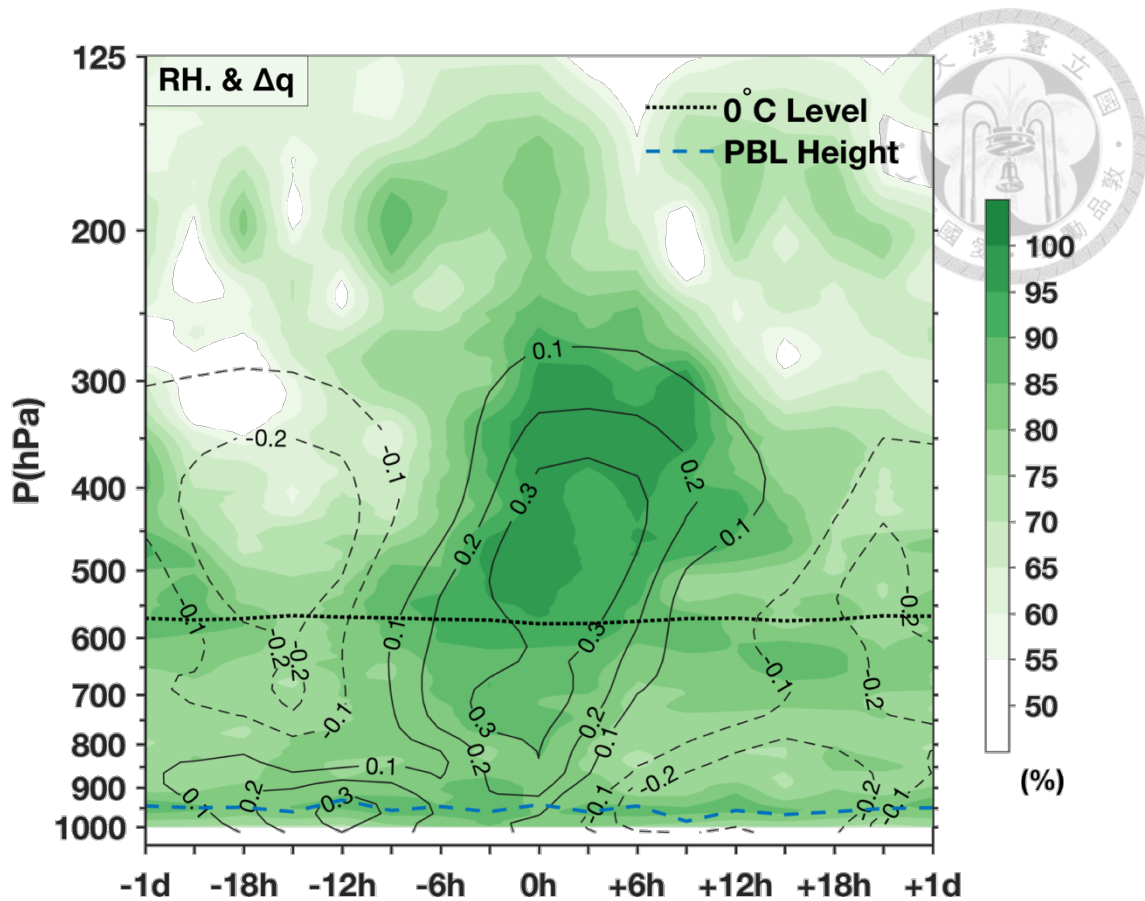
Figure 6.2. The 48-hours window composites for the quasi-2-day convective events, including RH from Gan radiosonde with respect to ice for T < 0°C (colored) and water vapor mixing ratio (q) anomaly from AMIE-Gan objective analysis (g/kg; positive values in black solid contours and negative values in black dashed contours). The period-mean 0°C level height and the boundary layer height are indicated the same as in Figure 6.1.
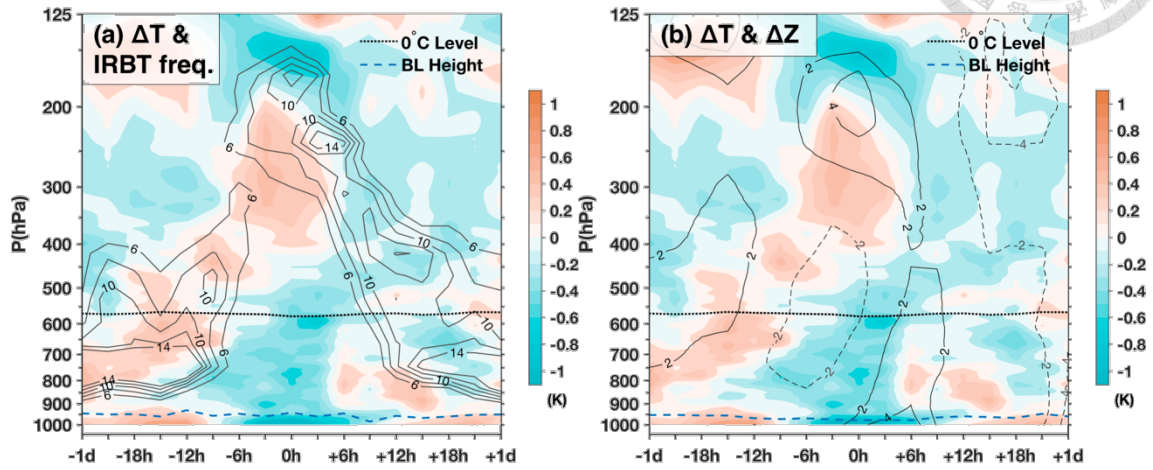
105

Figure 6.3.　　Composites similar to Figure 6.2, except for the temperature anomaly (K; colored) from radiosonde at Gan overlaid with (a) the IRBT areal percentage from 6% to 14% same as Figure 6.1a (black contour), and (b) geopotential height anomaly (m; positive values in black contour and negative values in dashed black contour) from Gan radiosonde. The period-mean 0°C level height and the boundary layer height in each subfigure are indicated the same as in Figure 6.1.
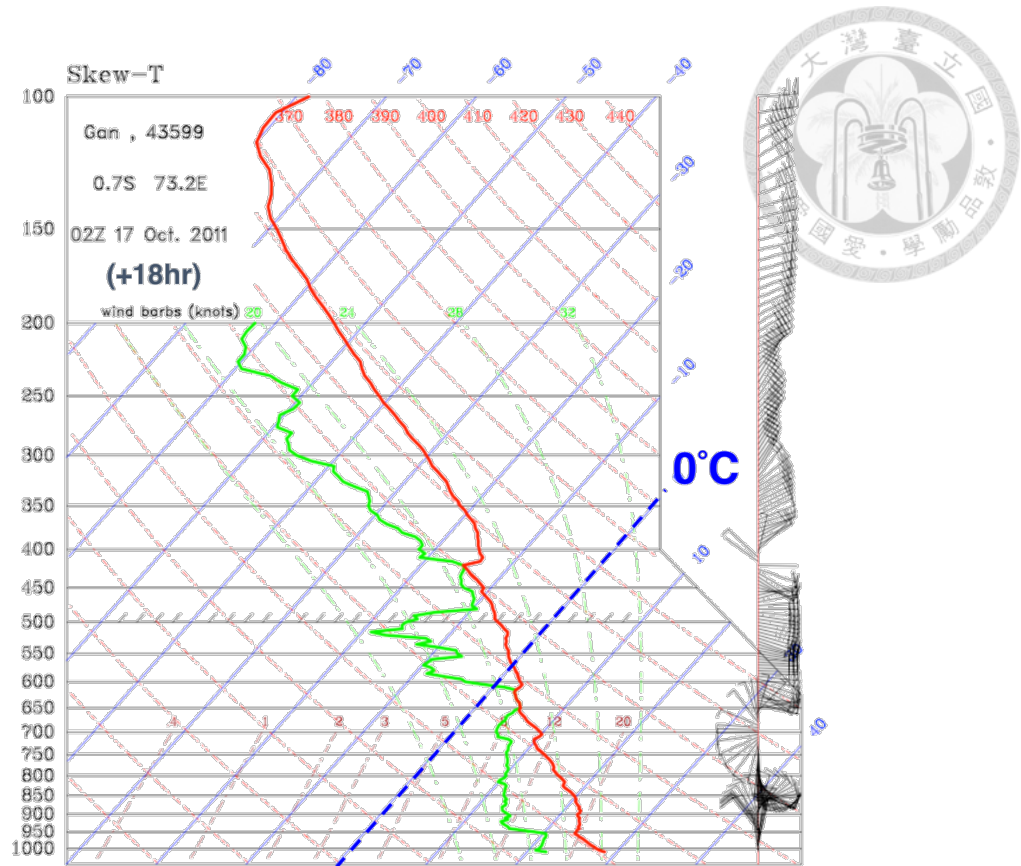
Figure 6.4.   An example of "onion-type" radiosonde profile in the high vertical resolution skew-T log-P diagram of Gan radiosonde at 02Z on 17 October 2011, corresponding to +18 h in the quasi-2-day life cycle. The red and green solid lines indicate the temperature and dew-point temperature profiles respectively. The blue dashed line indicates the 0°C level.
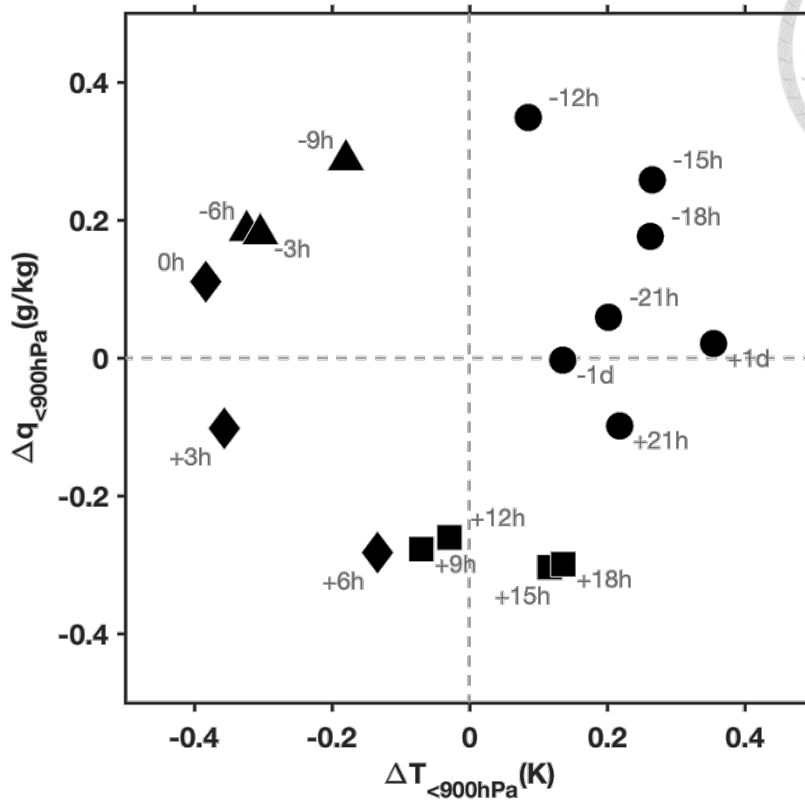
Figure 6.5.   Phase diagram for the composites of temperature anomaly (abscissa) and moisture anomaly (ordinate) under 900-hPa in the quasi-2-day convective disturbances. The 3-hourly times in the 48-hour window are indicated in gray, four stages of convection — suppressed, convective intensifying, mature and stratiform — are represented in circle, triangle, diamond, and square, respectively.
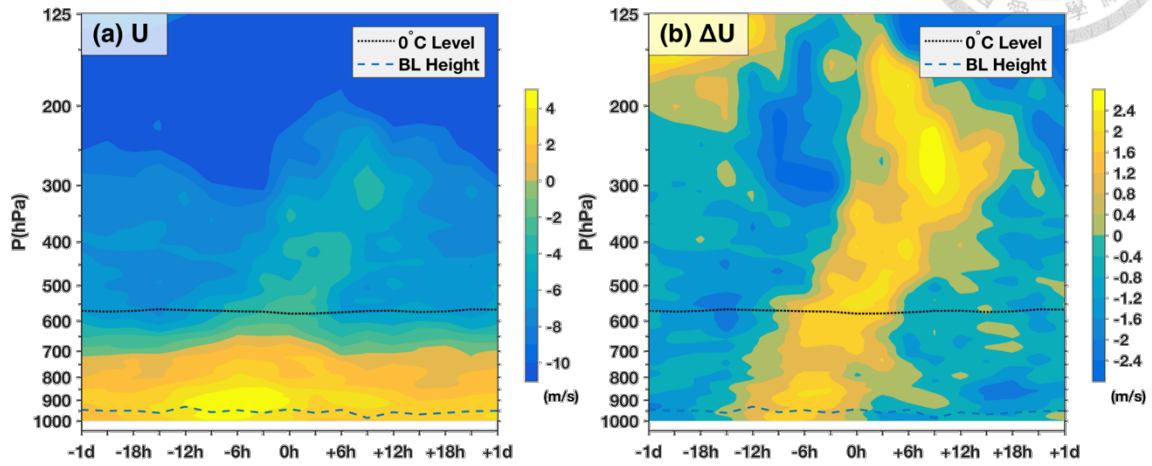
Figure 6.6.   Composites similar to Figure 6.2, except for (a) the zonal wind (m/s), and (b) the zonal wind anomaly (m/s) from radiosonde at Gan. The period-mean 0°C level height and the boundary layer height in each subfigure are indicated the same as in Figure 6.1.
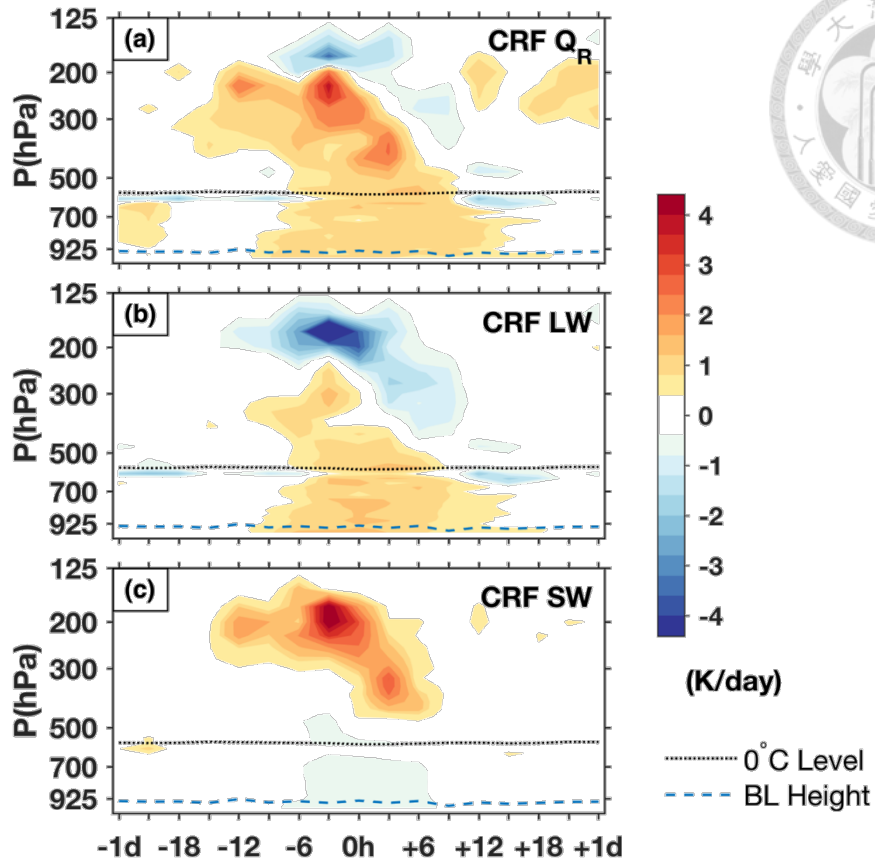
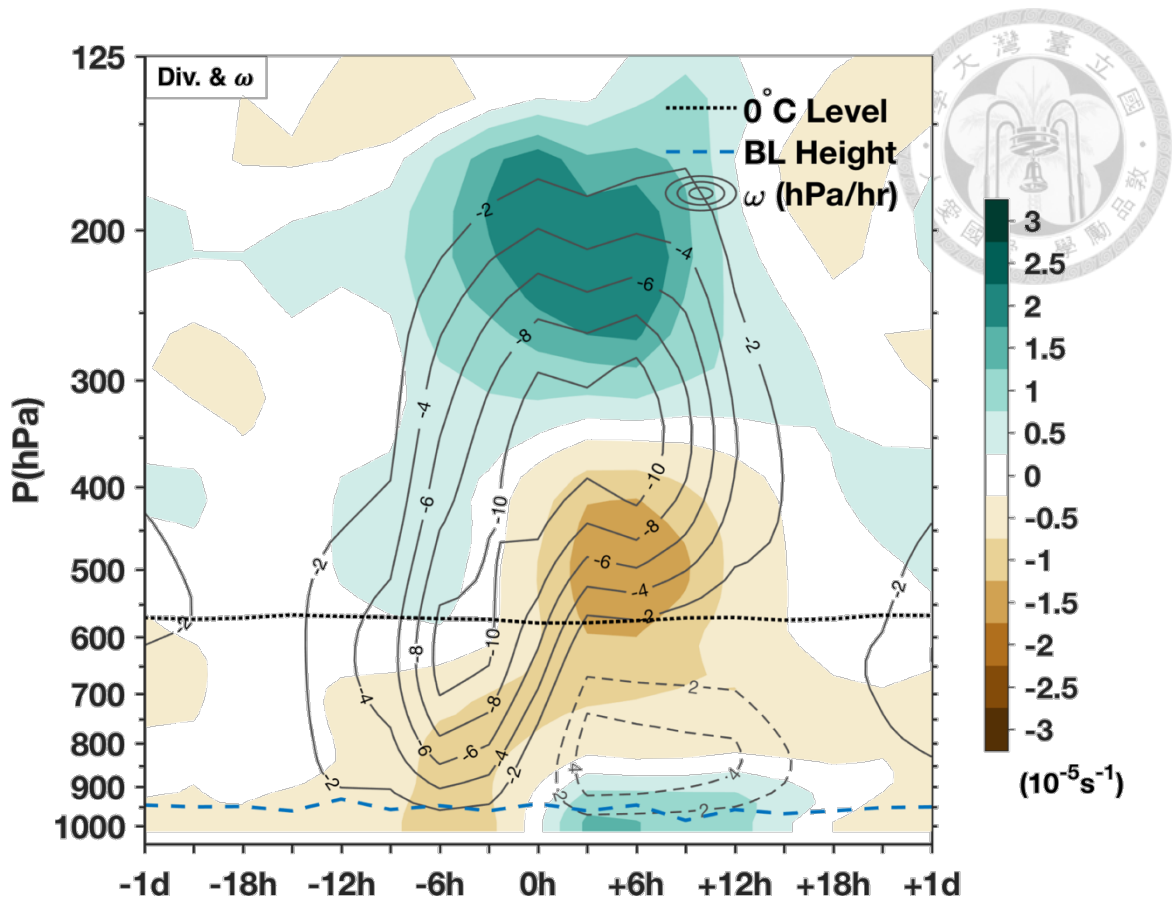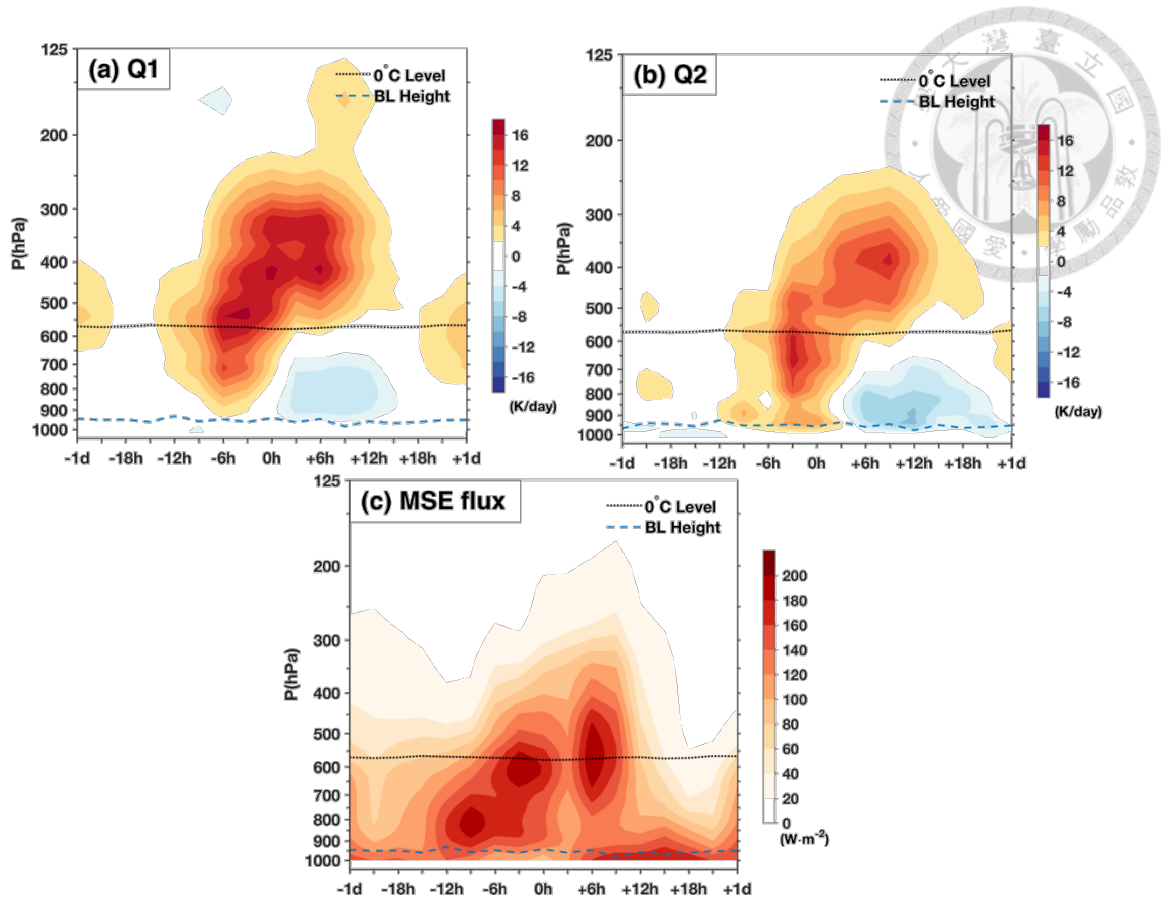Figure 6.7. Similar composites to Figure 6.2 except for the variations of cloud radiative forcings (CRF; K/day) from the CombRet dataset. Figure 6.7a to Figure 6.7c indicates the total cloud radiative heating rate (Q_R = LW + SW), the longwave (LW) cloud heating rate, and shortwave (SW) cloud heating rate respectively. The period-mean 0°C level height and the boundary layer height in each subfigure are indicated the same as in Figure 6.1.

Figure 6.8.   Composite similar to Figure 6.2, except for the horizontal wind divergence (colored; in units of $10^{-5}s^{-1}$) and the vertical motions (in units of hPa/hr; upward motions in solid contours and downward motions in dashed contours). The period-mean 0°C level height and the boundary layer height in each subfigure are indicated the same as in Figure 6.1.

Figure 6.9.   Composite similar to Figure 6.2, except for (a) the apparent heating Q_1 (K/day), (b) the apparent drying Q_2 (K/day), and (c) the vertical eddy flux of MSE (Jm^{-2}s^{-1}) calculated from AMIE-Gan large-scale objective analysis and CombRet dataset. The period-mean 0°C level height and the boundary layer height in each subfigure are indicated the same as in Figure 6.1.
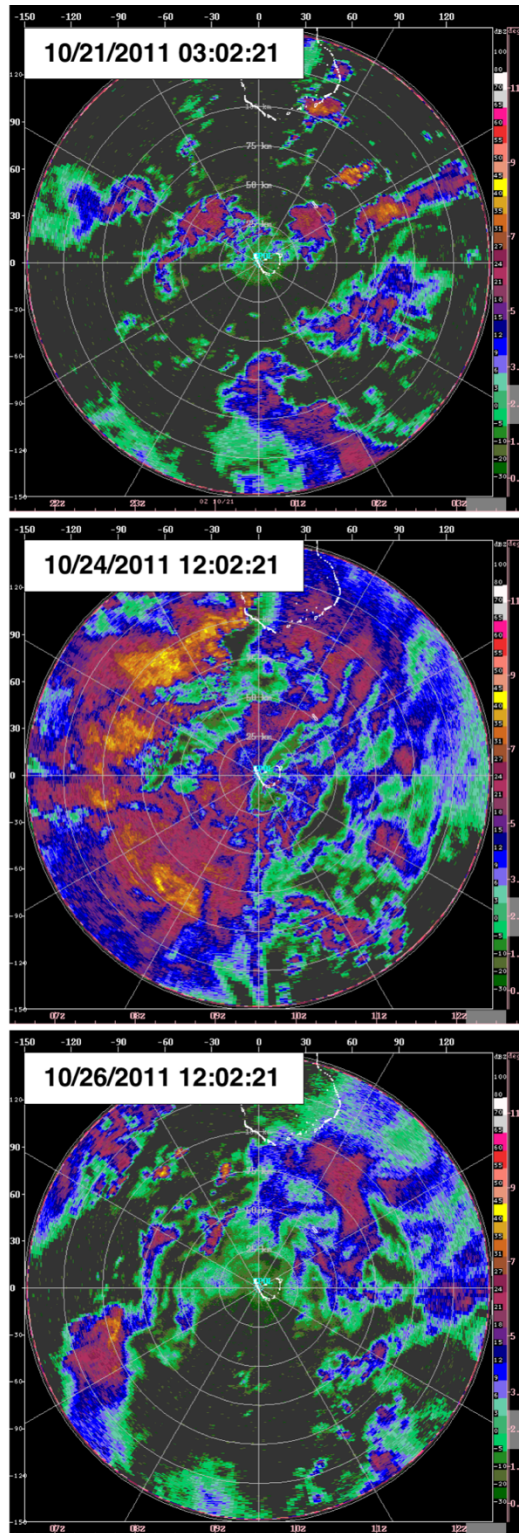
Figure 6.10.   Images of NCAR S-Pol radar reflectivity over a 150-km radius region around Gan during MJO1. The time of each radar image corresponds to +6 h in the quasi-

2-day life cycle (from top to bottom: 03:02Z on 10/21, 12:02Z on 10/24, and 12:02Z on

10/26). Images available at

http://catalog.eol.ucar.edu/cgi-

bin/dynamo/research/prod_browse?platform=SPOL_S_BAND&prod=sband_DBZ_150

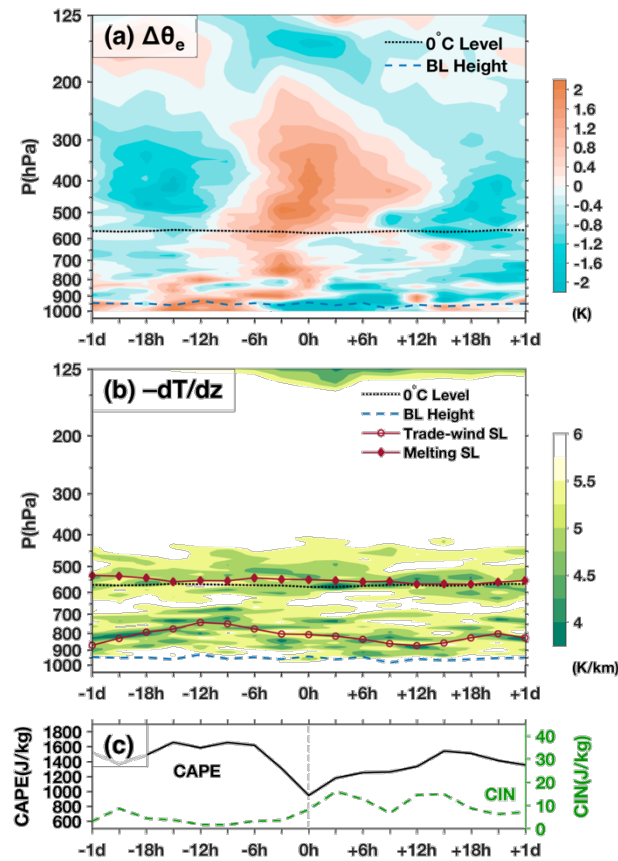km&howmany=All&start=Start+Date&end=End+Date&submit=retrieve+products.

Figure 6.11.   Composites similar to Figure 6.2 except for (a) the equivalent potential temperature anomaly computed by subtracting the MJO1 time-period mean from the composite fields (K; colored), (b) the atmospheric temperature lapse rate (K/km), and (c) the CAPE (black solid) and CIN (green dashed) calculated from radiosonde at Gan. In (b), the average heights of the top 10% most stable levels within the melting stable layer (trade-wind stable layer) are highlighted in dark red line with diamond (circle) markers. The period-mean 0°C level height and the boundary layer height in subfigures were indicated the same as in Figure 6.1.
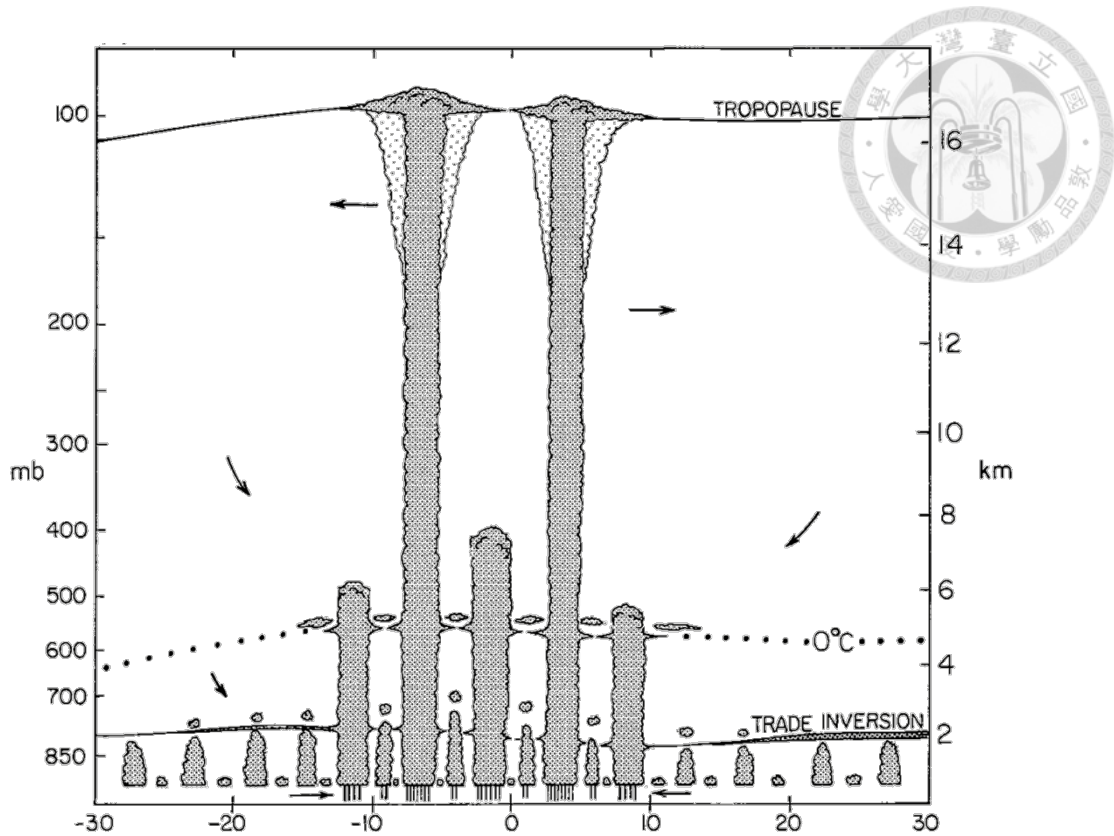
Figure 6.12. A conceptual model of tropical cumulus cloud distributions according to TOGA COARE IOP observations. Three main cloud types are indicated: shallow cumulus, cumulus congestus, and cumulonimbus, along with three stable layers indicated, the trade-wind stable layer in the lower troposphere, the melting stable layer near 0°C level, and the tropopause inversion layer. Arrows indicate meridional circulation. (Figure 13b in Johnson et al. 1999)
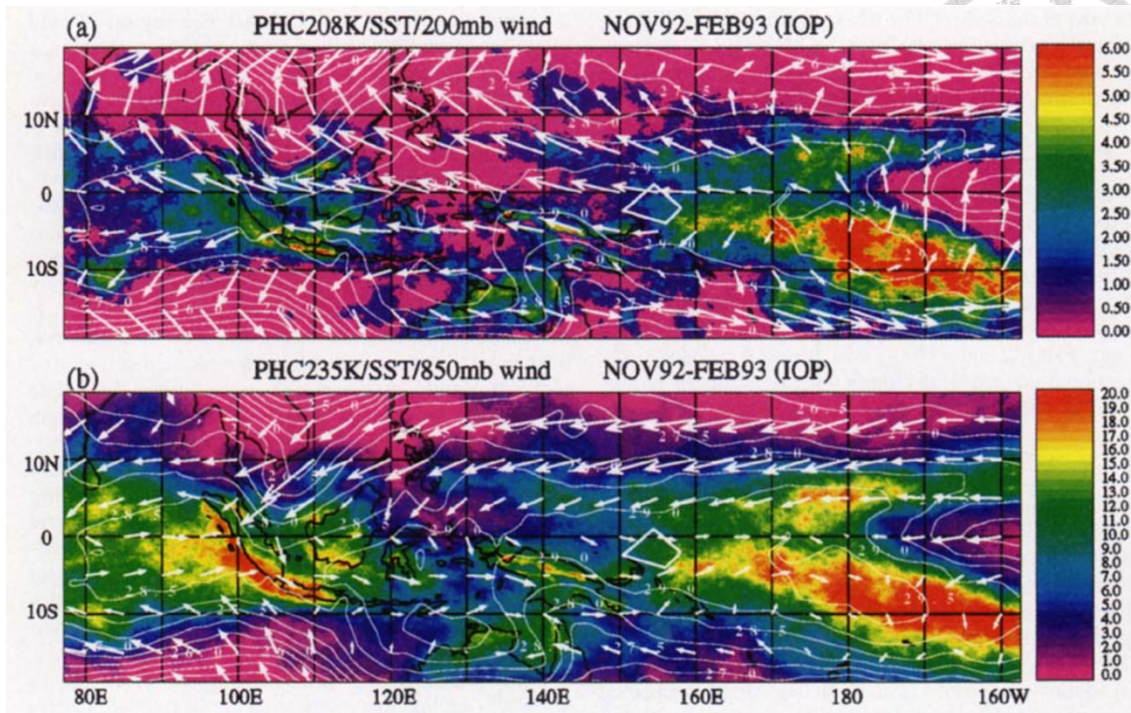
116

Figure 7.1.   The percentage of high cloudiness (shaded), the mean SST (contours) and the mean global wind analysis (arrows) for November 1992 through February 1993. (a) High cloudiness with cloud-top temperature <208 K and wind at 200 hPa. (b) Cloud-top temperature <235 K and wind at 850 hPa. Wind vectors are scaled such that 10 m/s wind is represented by a vector that would be 2.5° in length on the map. The TOGA COARE IFA is outlined. (Figure 2 in Chen et al. 1996)
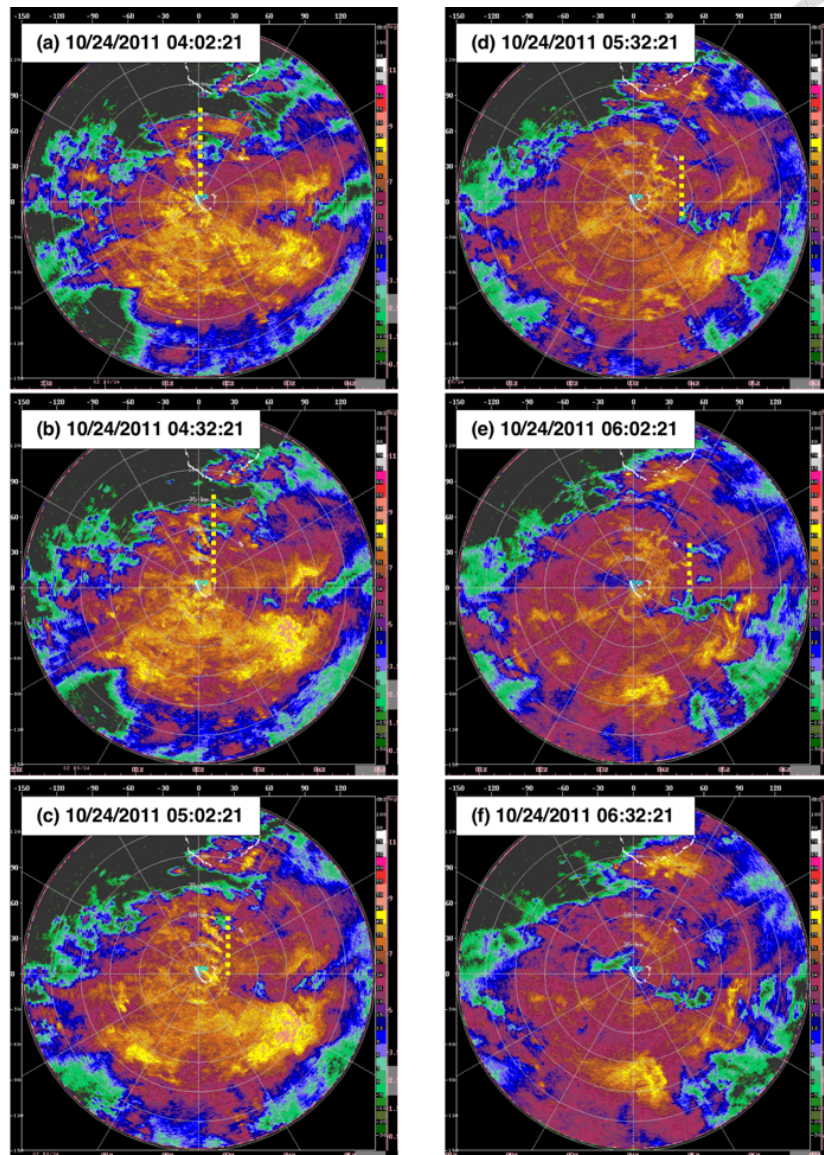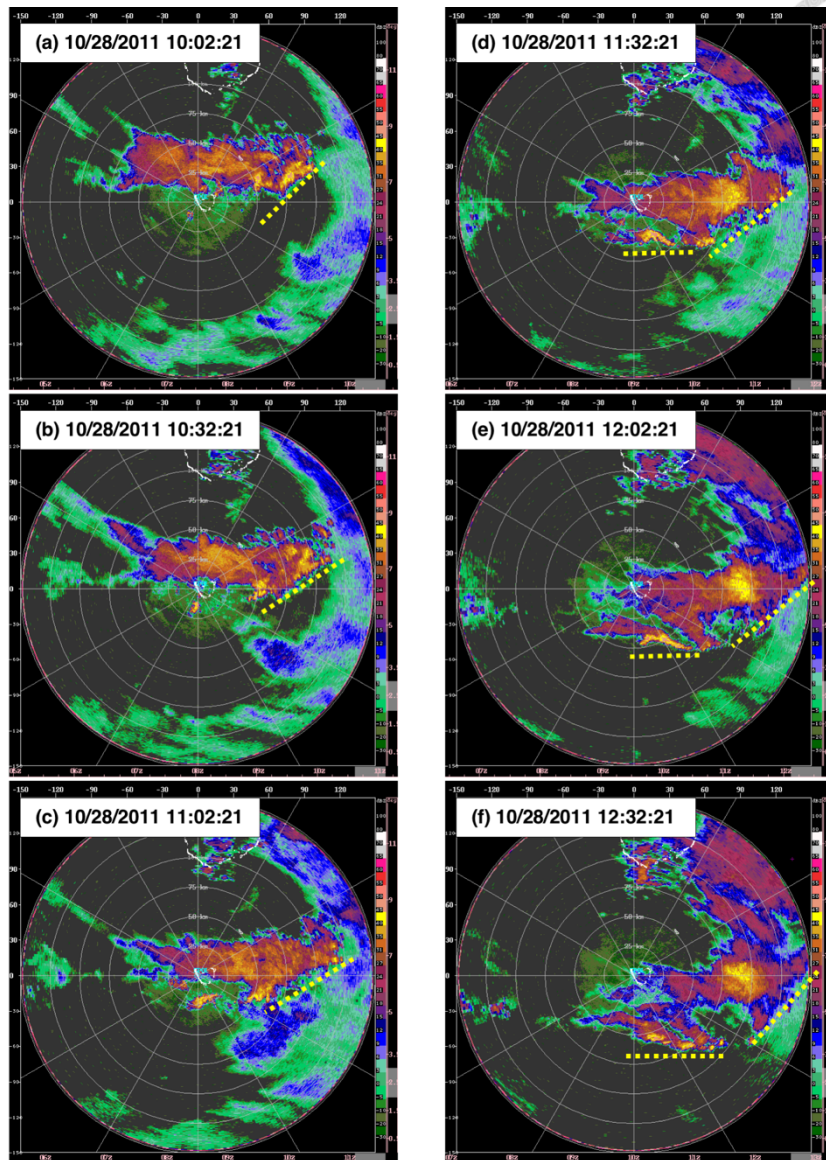
Figure 7.2. Images of NCAR S-Pol radar reflectivity over a 150-km radius region around Gan on 24 October 2011. From (a) to (f), 04:02Z, 04:32Z, 05:02Z, 05:32Z, 06:02Z, and 06:32Z. The yellow dotted vertical lines in subfigures (a) to (e) indicate the edges of eastward shifting convection. Images available at

http://catalog.eol.ucar.edu/cgi-

bin/dynamo/research/prod_browse?platform=SPOL_S_BAND&prod=sband_DBZ_150

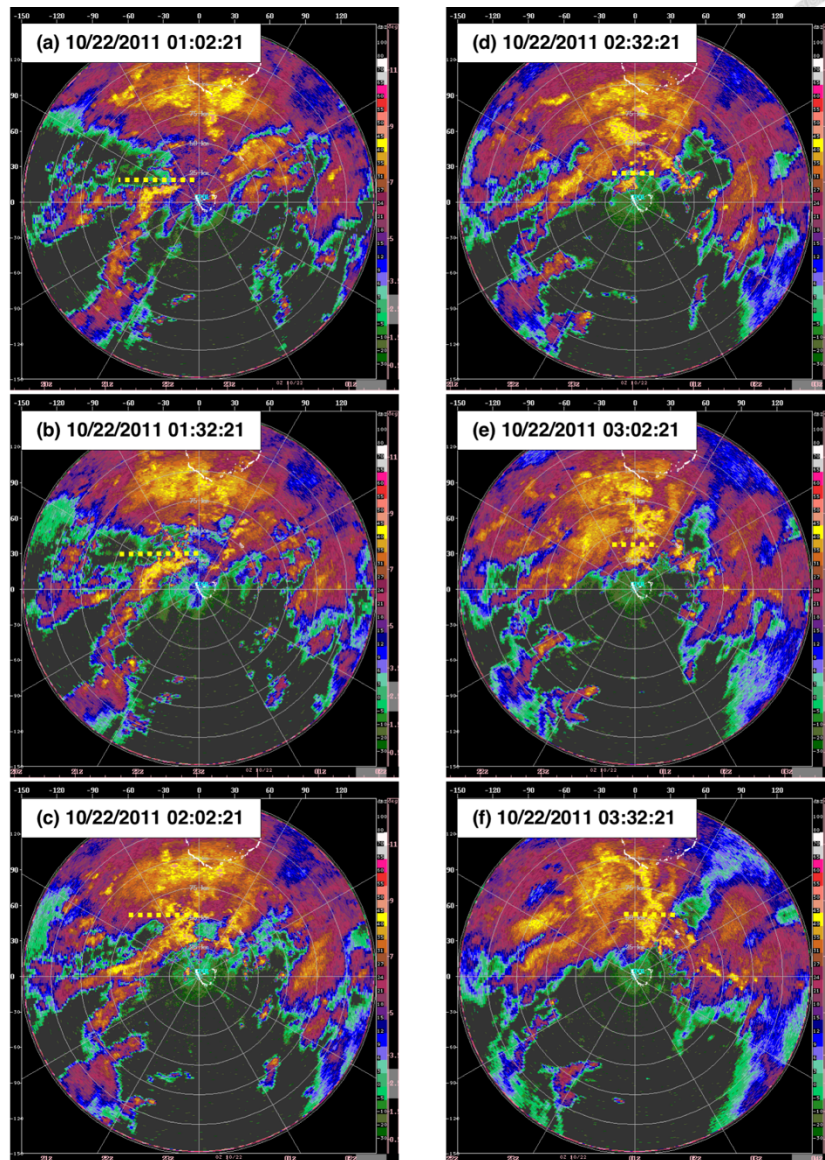km&howmany=All&start=Start+Date&end=End+Date&submit=retrieve+products.

118

Figure 7.3.   Images of NCAR S-Pol radar reflectivity over a 150-km radius region around Gan on 28 October 2011. From (a) to (f), 10:02Z, 10:32Z, 11:02Z, 11:32Z, 12:02Z, and 12:32Z. The yellow dotted horizontal lines in subfigures (a) to (f) indicate the edges of convective cells near Gan. Images available at

http://catalog.eol.ucar.edu/cgi-bin/dynamo/research/prod_browse?platform=SPOL_S_BAND&prod=sband_DBZ_150km&howmany=All&start=Start+Date&end=End+Date&submit=retrieve+products.

Figure 7.4.   Images of NCAR S-Pol radar reflectivity over a 150-km radius region around Gan on 22 October 2011. From (a) to (f), 01:02Z, 01:32Z, 02:02Z, 02:32Z, 03:02Z, and 03:32Z. The yellow dotted horizontal lines in subfigures (a) to (c) and (d) to (e) indicate the edges of northward shifting convection near Gan from 01Z to 02Z and from 02Z to 03Z, respectively. Images available at

http://catalog.eol.ucar.edu/cgi-

bin/dynamo/research/prod_browse?platform=SPOL_S_BAND&prod=sband_DBZ_150

km&howmany=All&start=Start+Date&end=End+Date&submit=retrieve+products.
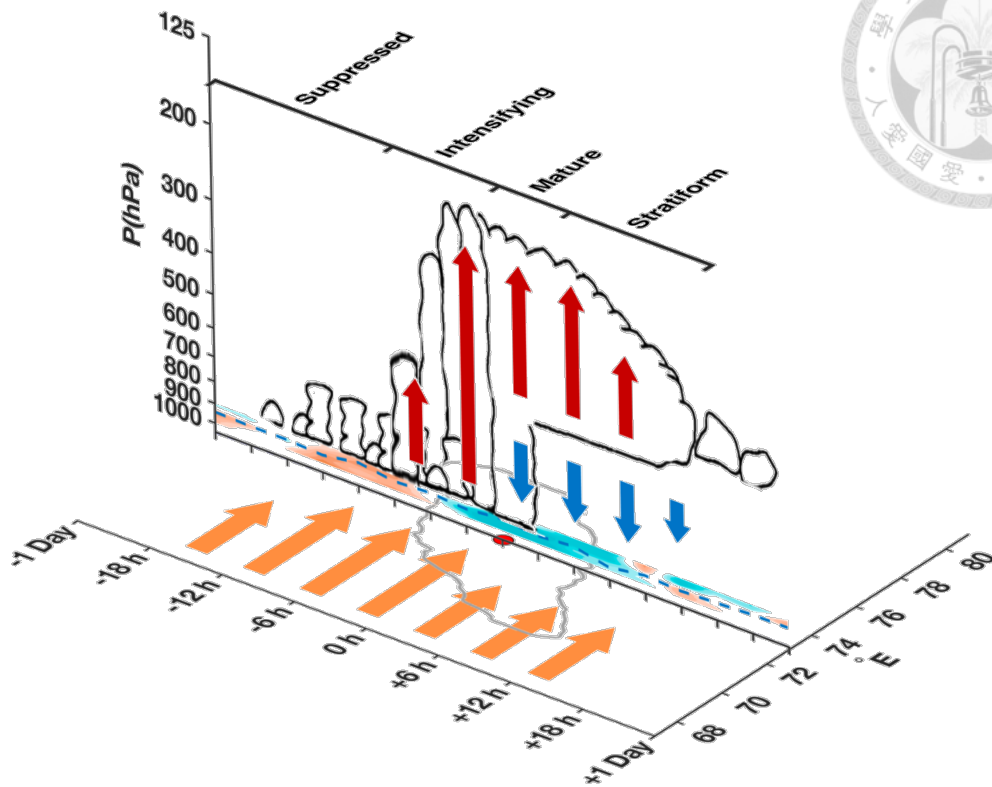
Figure 7.5.   Schematics for the quasi-2-day convective disturbances over the central IO during DYNAMO. The horizontal panel shows the time-longitude schematics of low-level zonal winds (orange arrows) and westward-propagating convective disturbance (similar to Figure 4.2). The vertical panel shows the schematics of cloud development, with four stages indicated, and vertical motions (upward motions in red arrows and downward motions in blue), in addition to the equivalent potential temperature anomaly (as in Figure 6.11a) in the BL. The BL heights were indicated in dashed blue line.

121
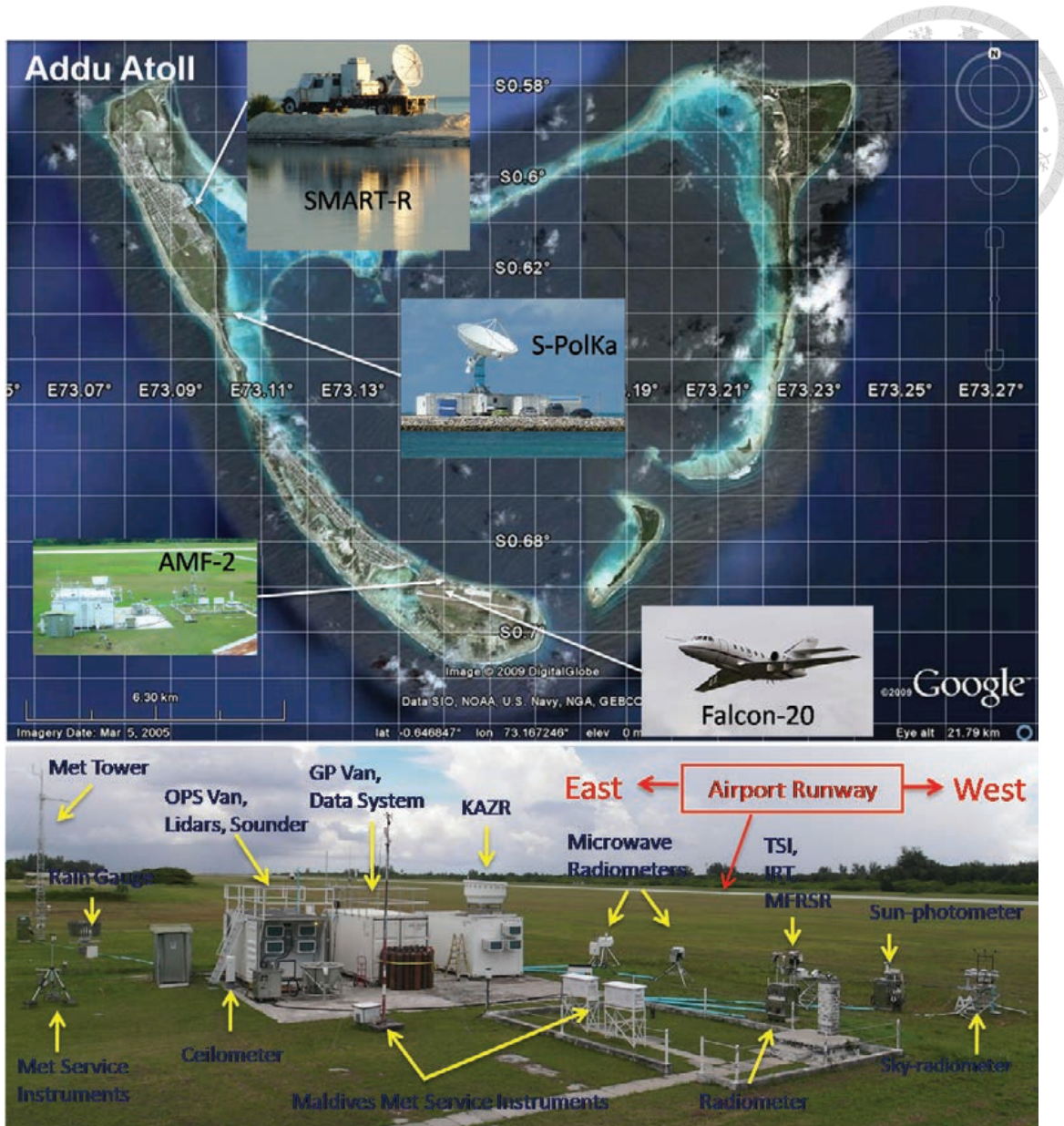
Figure A.1.   A super (radar) site on Addu Atoll, Maldives (Gan Island). (top) locations

of three radar sites and an aircraft base. (bottom) the second ARM Mobile Facility (AMF2)

deployed at the Gan airport. (Figure 3 in Yoneyama et al. 2013)

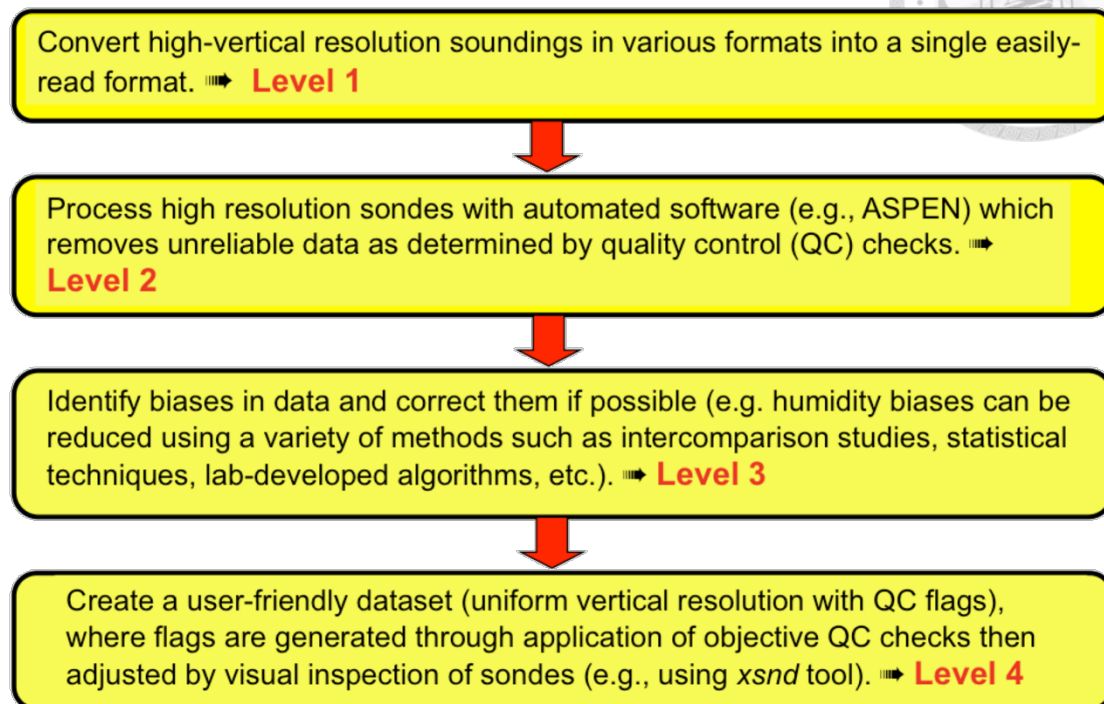## Stages to developing a research-quality sonde dataset

Convert high-vertical resolution soundings in various formats into a single easily-read format. ⇒ **Level 1**

Process high resolution sondes with automated software (e.g., ASPEN) which removes unreliable data as determined by quality control (QC) checks. ⇒ **Level 2**

Identify biases in data and correct them if possible (e.g. humidity biases can be reduced using a variety of methods such as intercomparison studies, statistical techniques, lab-developed algorithms, etc.). ⇒ **Level 3**

Create a user-friendly dataset (uniform vertical resolution with QC flags), where flags are generated through application of objective QC checks then adjusted by visual inspection of sondes (e.g., using *xsnd* tool). ⇒ **Level 4**

Figure A.2.   Flowchart showing various stages for developing a research-quality radiosonde dataset. (Figure 1 in Ciesielski et al. 2012)
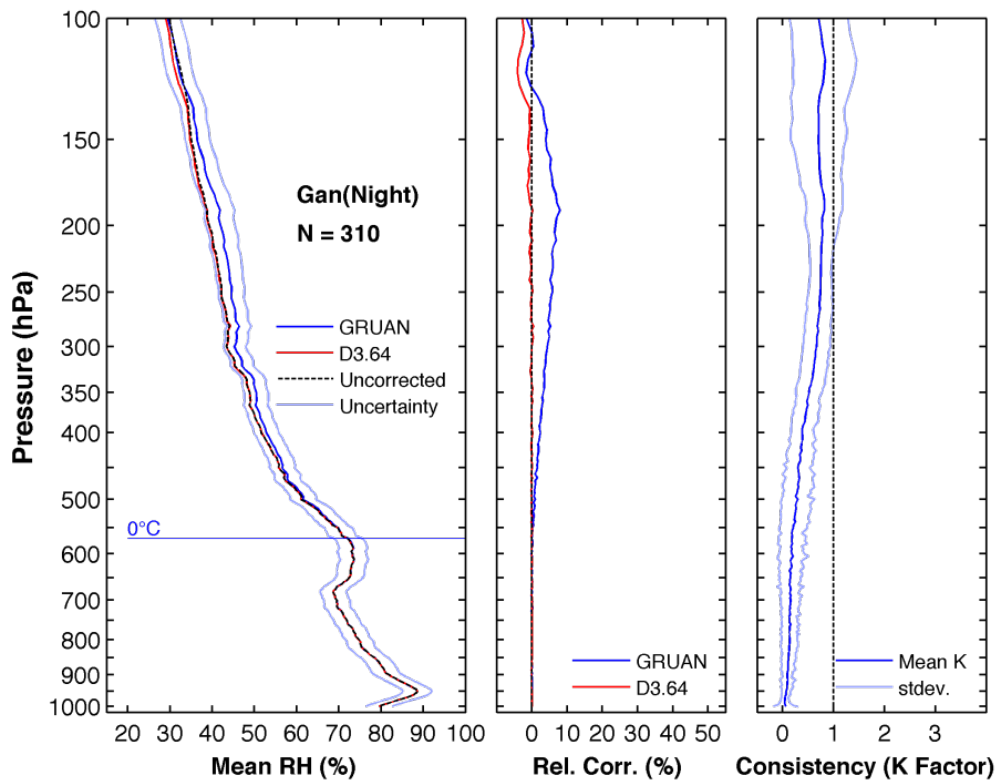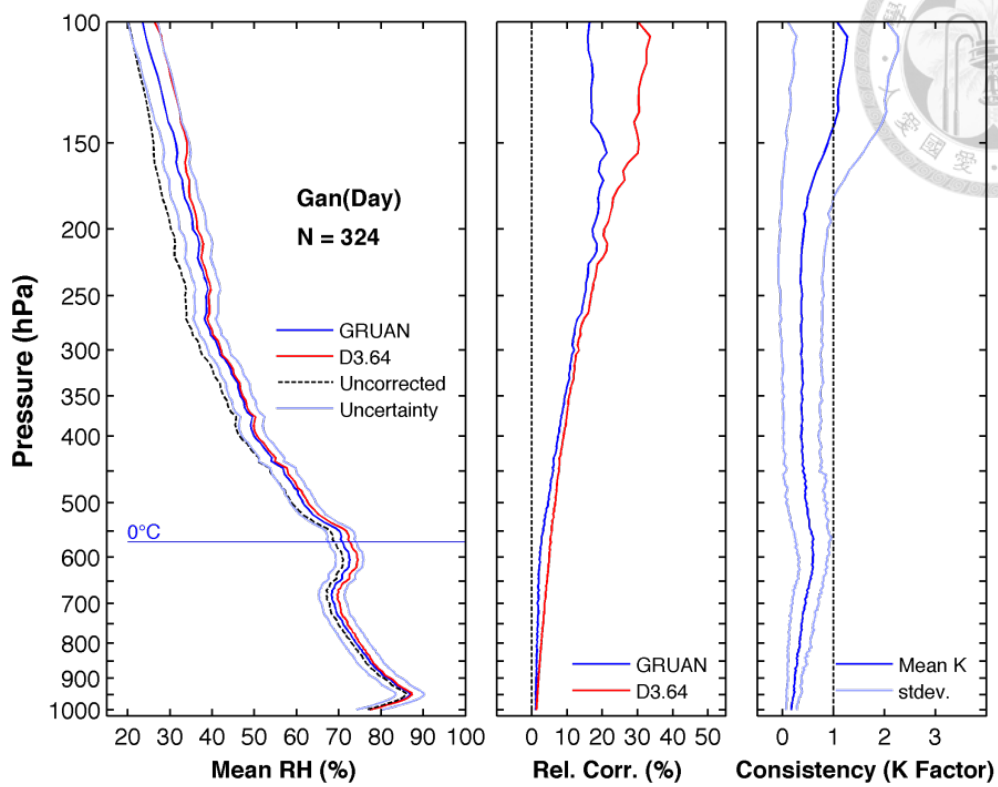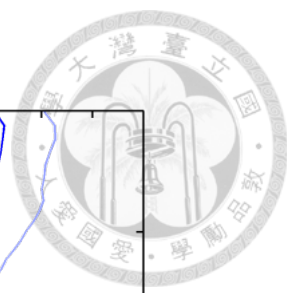
Figure A.3. Mean vertical profiles of RH at Gan for (top) daytime and (bottom) nighttime soundings with uncorrected and corrected data and uncertainty range for (left) GRUAN corrections, (middle) relative RH corrections, and (right) consistency of correction. Levels with k ≤1 indicate good consistency between corrections. Freezing level and the number of sounding (N) in each period are also shown (left).
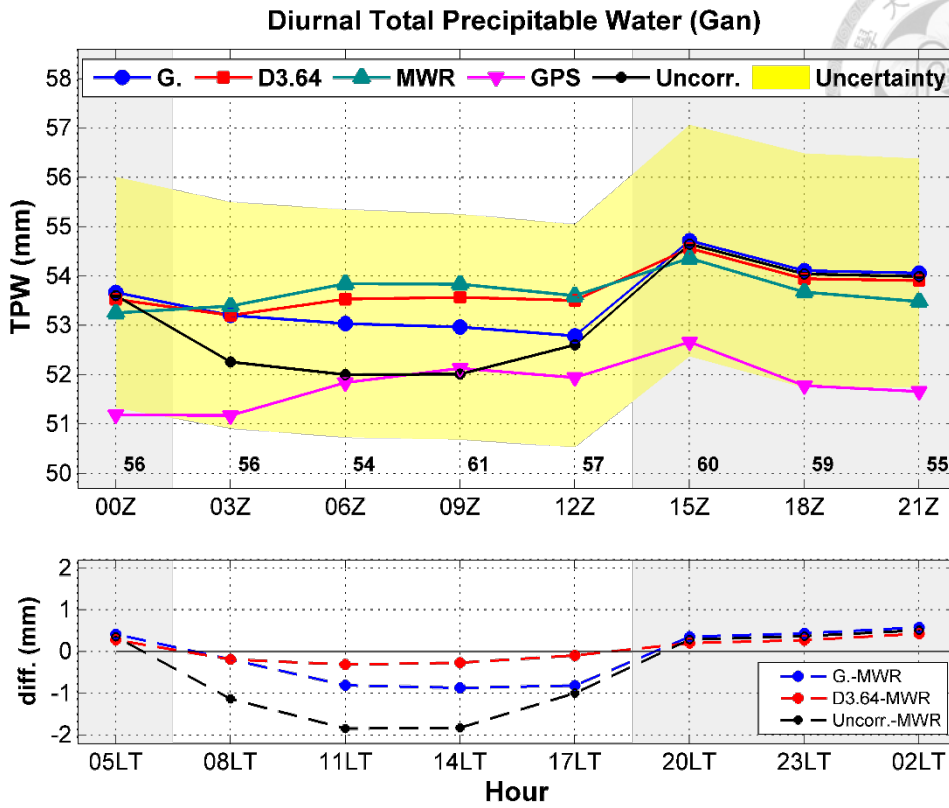
125

Figure A.4. (top) Mean diurnal cycle of TPW (mm) for Gan with uncorrected sounding data (black line), GRUAN-corrected data (blue line), DigiCORA-corrected data (red line), MWR (green line), and GPS (magenta line). Light yellow shading indicates the TPW uncertainty based on GRUAN estimates. Gray shading indicates nighttime hours. (bottom) TPW difference (mm) between uncorrected and corrected soundings and MWR. Note that the time axis is (top) UTC time and (bottom) local time.
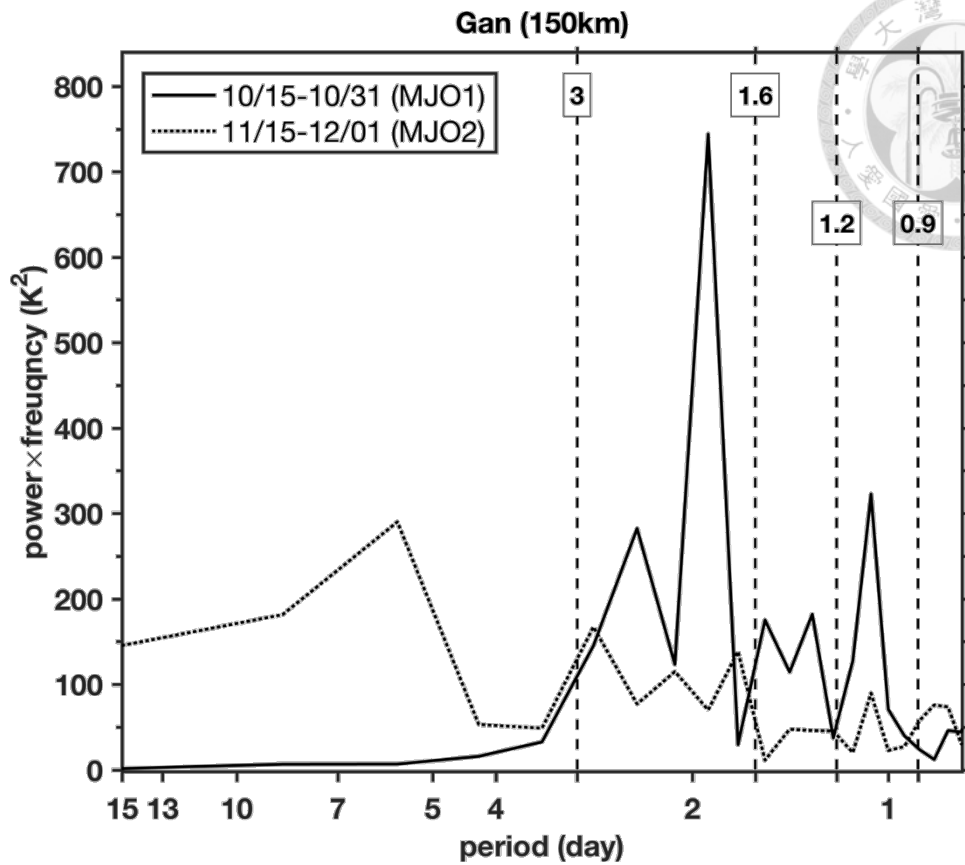
126

Figure B.1.   Similar to Figure 5.1 except for the Fourier power spectrum of the averaged IRBT over the 150-km region around Gan during MJO2 (15–30 November 2011; dotted) and MJO1 (15–31 October 2011; solid).
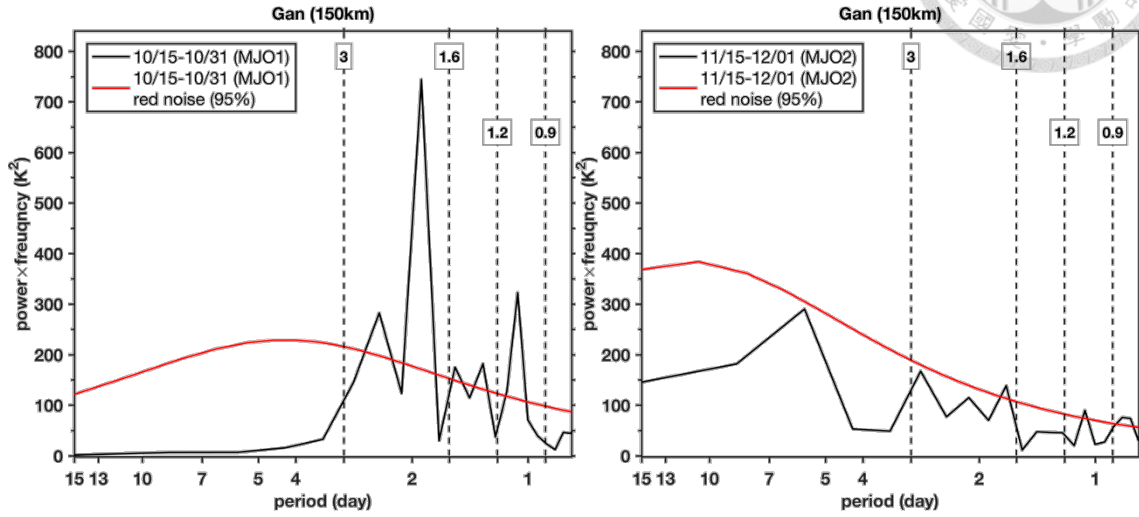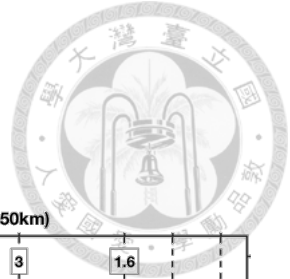
Figure B.2.   As in Figure B.1 except for MJO1 (left) and MJO2 (right), respectively. The red solid lines in both figures indicate the power spectrum of red noise at the confidence level of 95% through χ^2-test.
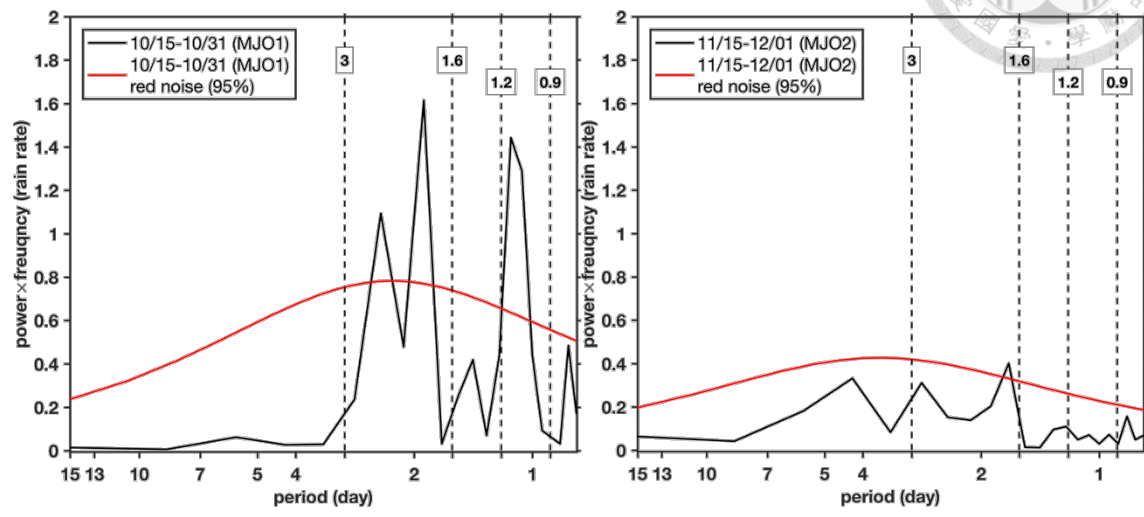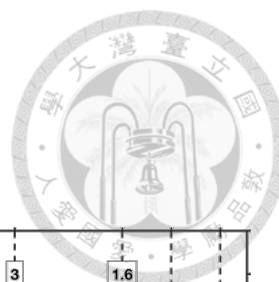
128

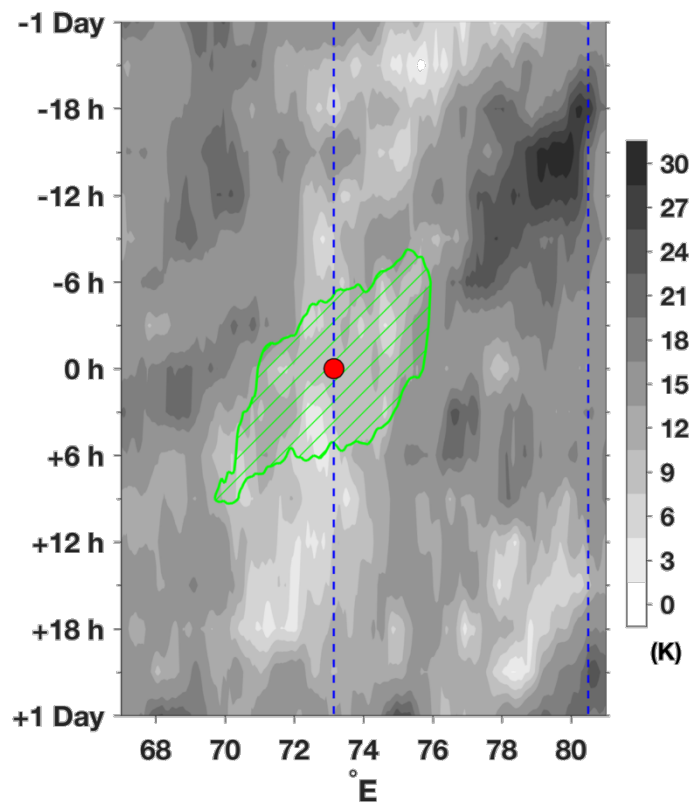Figure B.3.   Same as Figure B.2 except for the averaged TRMM rain rate over the 150-km region around Gan.

Figure B.4.   Similar to Figure 4.2 except the shading indicates the stdev composite of IRBT among the seven cases and the green hatched region indicates the averaged IRBT composite <240 K.
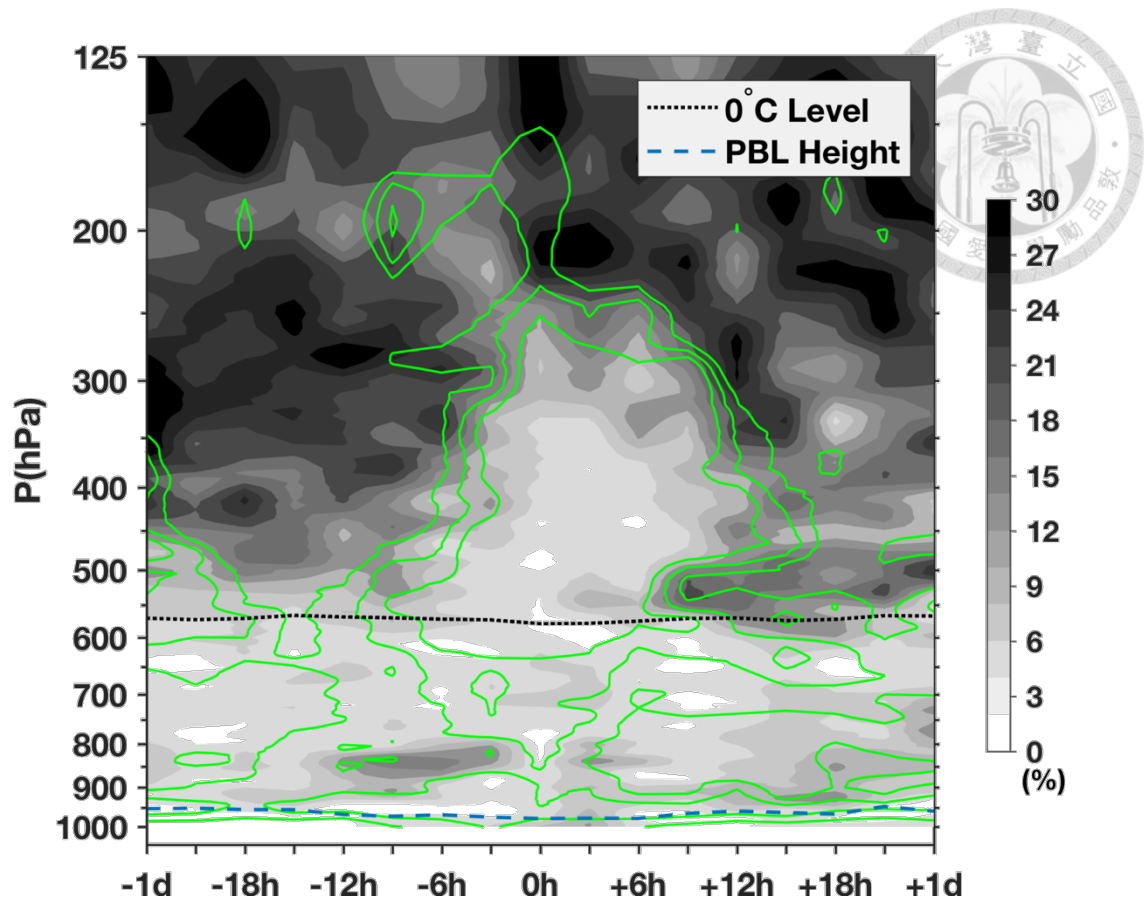
Figure B.5.   Similar to Figure 6.2 except the shading indicates the stdev composite of RH with respect to ice derived from Gan radiosonde among the seven cases and the green contours indicate the RH of 80%, 85%, and 90%.
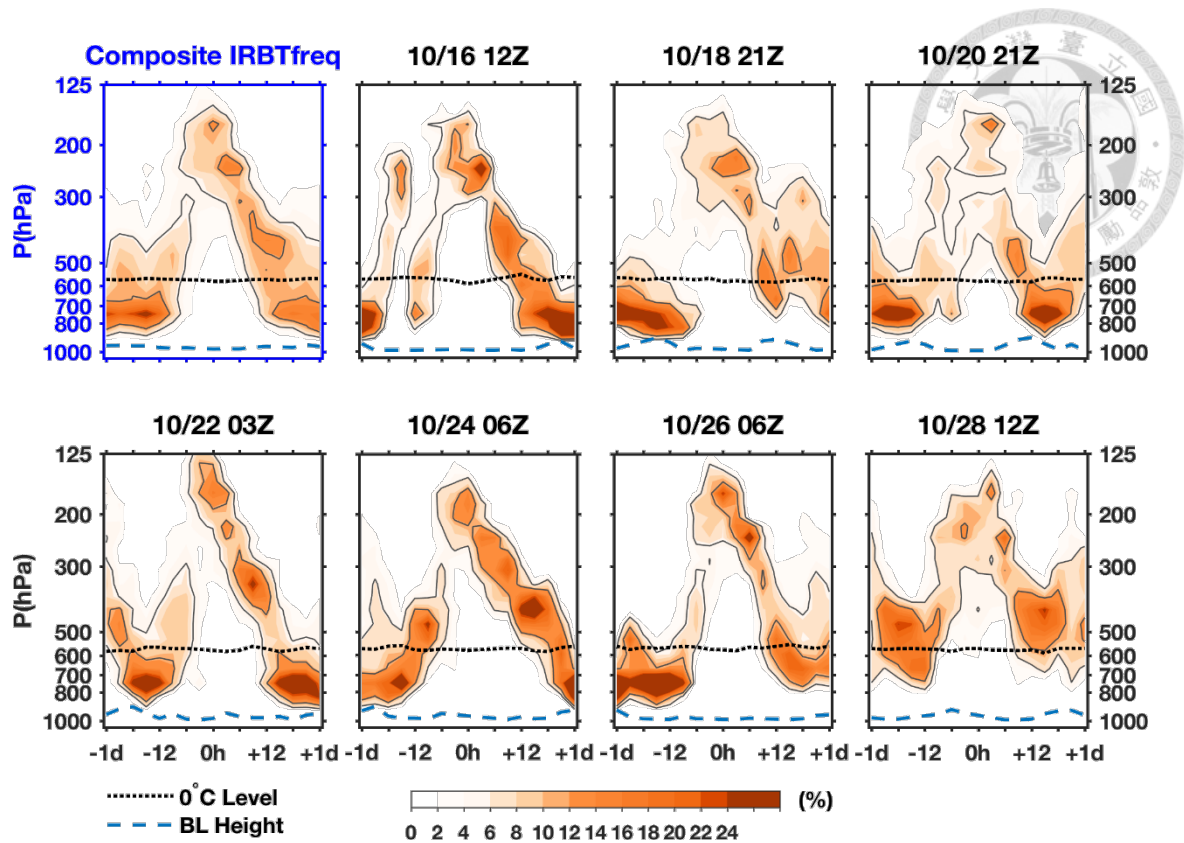
Figure B.6.   The 48-hours window composite (top left) and time variations (others) of IRBT populations for the quasi-2-day convective events. Percentages of 6% and 12% are indicated in solid black contours. The composite (top left) is identical to Figure 6.1a; other sub-figures are plotted in the same manner except centered at times of each event as listed in Table 3.1.
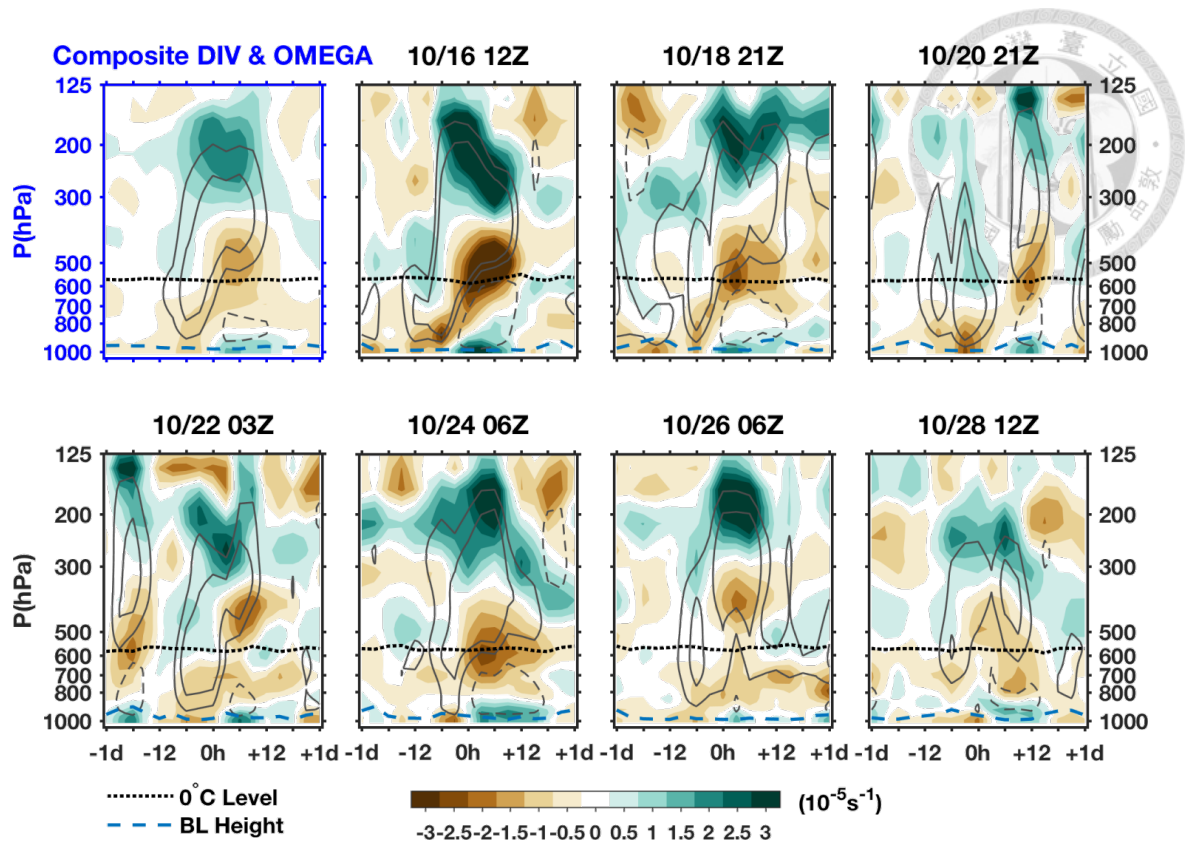
Figure B.7. Similar to Figure B.6 except for the horizontal divergence ($10^{-5}s^{-1}$, colored) and the vertical motions of -4 and -8 (+4) hPa/hr in solid (dashed) black contours.
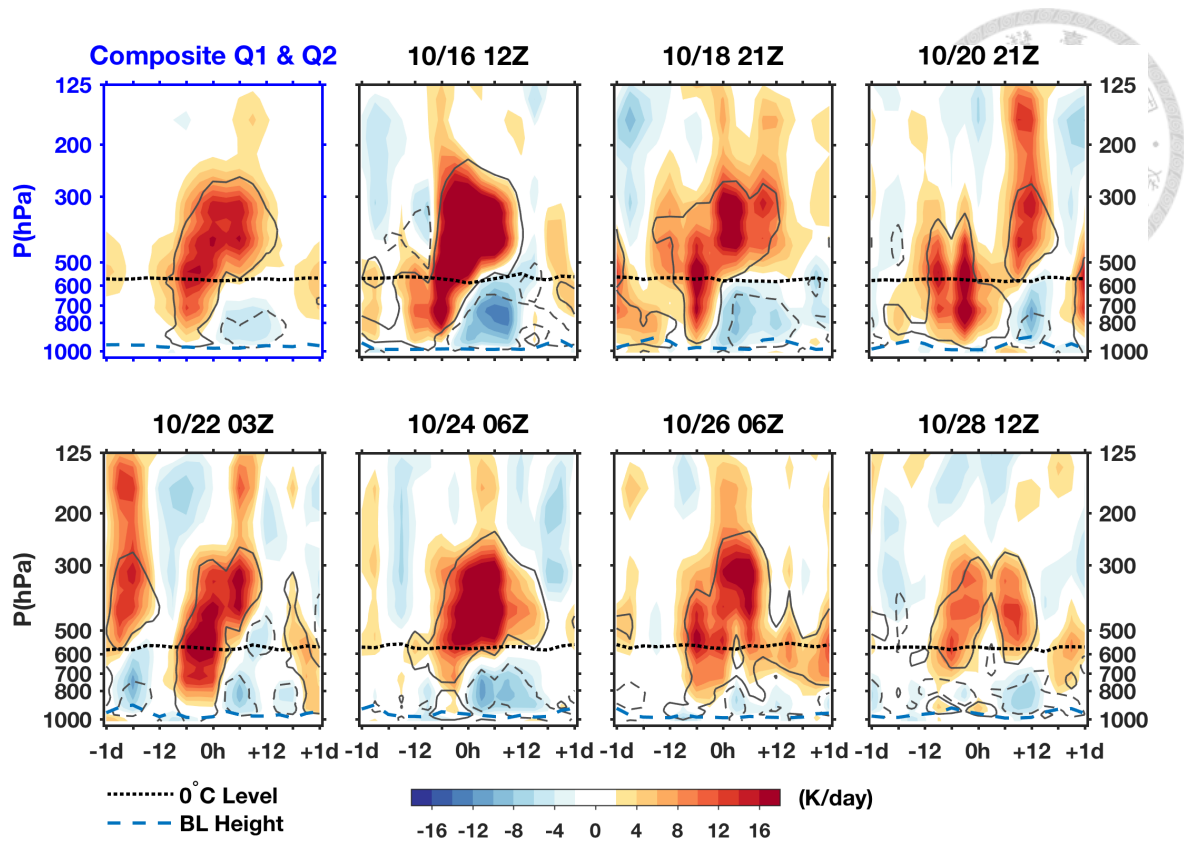
133

Figure B.8.   Similar to Figure B.6 except for Q1 (K/day, colored) and Q2 of +4 (–4) K/day in solid (dashed) black contours.